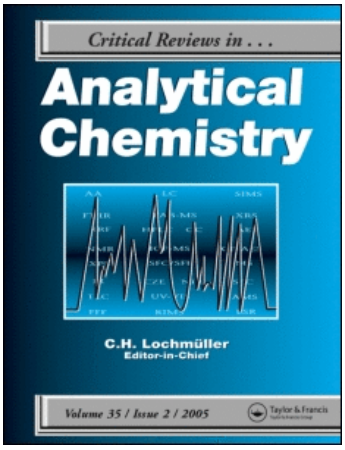

Critical Reviews in Analytical Chemistry
Publication details, including instructions for authors and subscription information:
http://www.informaworld.com/smpp/title~content=t713400837

ESCA

Robert S. Swingle II; William M. Riggs; Jon Amy

To cite this Article Swingle II, Robert S. , Riggs, William M. and Amy, Jon(1975) 'ESCA', Critical Reviews in Analytical Chemistry, 5: 3, 267 — 321
To link to this Article: DOI: 10.1080/10408347508542687
URL: http://dx.doi.org/10.1080/10408347508542687

ESCA

Authors: **Robert S. Swingle, II**
Central Research and Development Department
E. I. du Pont de Nemours and Company
Experimental Station
Wilmington, Delaware

William M. Riggs
Physical Electronics Industries, Inc.
Eden Prarie, Minnesota

Referee: Jon Amy
Department of Chemistry
Purdue University
West Lafayette, Indiana

TABLE OF CONTENTS

I. INTRODUCTION

Since the discovery of the chemical shift phenomenon and the pioneering work by Siegbahn and co-workers in the mid-1960s,[1,2] ESCA (Electron Spectroscopy for Chemical Analysis) has become a powerful tool for chemists and physicists. The technique has been used to study solid state band structure and atomic and molecular bonding in both the solid state and the gas phase. From the point of view of the analytical chemist, however, one of the most important uses of the technique has been in the analysis of solid surfaces. The ESCA technique is essentially nondestructive, universal for all elements except hydrogen, samples a layer less than ~30Å in depth, and can be applied to any vacuum-worthy solid. Indeed, at this depth resolution, ESCA is the only spectroscopic technique which can be used to study the surfaces of organic systems nondestructively.

The field of electron spectroscopy in general is a rapidly growing one, as evidenced by the large number of recent publications. The comprehensive reviews by Betteridge and Williams on U.V. excitation[3] and by Hercules and Carver on X-ray excitation (ESCA) plus Auger[4] cite a combined total of 840 references for the 1972 to 1973 period alone. A number of review articles have been published, some of which deal with the general area of electron spectroscopy,[5-9] and some of which deal with one or more specific areas within one mode of electron excitation.[10-12] In addition, at least six books on electron spectroscopy were available at the time this manuscript was prepared,[1,2,13-16] and a new periodical, *Journal of Electron Spectroscopy and Related Phenomena,* has come into being. Consequently,

the purpose of this article is not to survey the general field of electron spectroscopy or even the more specific area of X-ray photoelectron spectroscopy, as this would be redundant and hardly possible in the space available. The purpose of this article is to review X-ray photoelectron spectroscopy as presently applied to problems involving surface analysis. Section II.A gives a "broad brush" overview of the ESCA technique. Sections II.B and II.C contain more detailed discussions of reference levels, surface charging, chemical shifts, final state sources of structure, and quantitative analysis. These topics are important in a complete understanding of the ESCA method, and should be understood by those directly involved in spectral interpretation. However, some chemists may only be interested in understanding how ESCA can assist them in solving surface-related problems. These readers may wish to skip Sections II.B and II.C. In Section III, sample considerations and available commercial instrumentation are discussed, followed, in Section IV, by a review of selected applications of ESCA to surface analysis. Lastly, Section V compares ESCA with three other commercially available, spectroscopic methods for surface analysis; Auger Electron Spectroscopy (AES), Ion Scattering Spectroscopy (ISS), and Secondary Ion Mass Spectrometry (SIMS).

As outlined, the general framework of this article necessitates that several important areas in the field (such as a quantitative treatment of the chemical shift phenomenon) be mentioned only briefly. References to key papers in the areas not emphasized are provided for the reader interested in more complete information.

II. PRINCIPLES OF ESCA

A. Technique Overview

The basic ESCA experiment involves exposure of the material to be studied to a flux of monoenergetic X-rays of known energy. Absorption of these X-ray photons by atoms of the sample material results in the prompt emission of electrons, usually originating from the inner or core atomic orbitals. Since energy must be conserved in this photoemission process, the absorbed X-ray photon energy, hv, must be partitioned between the kinetic energy of the emitted electron, E_k, and the work expended in removing it from the atom, usually referred to as the electron binding energy, E_b, (i.e., $hv = E_b + E_k$). In practice, hv is known, and E_k is measured by the spectrometer, allowing direct determination of the electron binding energy from the single difference between hv and E_k. (In measurements conducted on solid materials, several other factors can influence the kinetic energy of emitted electrons. These factors and their significance are discussed in Section II.B.)

Since the atomic structure of each element is unique, measurement of the binding energies of one or two atomic orbitals for each element in a sample is usually sufficient to establish the qualitative elemental composition of the sample. All the elements of the periodic chart have electrons which can be detected in this way with the single exception of hydrogen. In addition, to qualitative elemental composition, information about the chemical environment and oxidation state of each element can frequently be extracted from a spectrum through precise measurement of electron-binding energies and peak shapes, and observation of multi-line structure.

The ability to obtain this information on solid materials is mainly significant in analytical chemistry because the spectrum is only characteristic of the outermost atomic layers of the sample, and provides a sensitive probe of surface composition and chemistry. The reason for this high degree of surface sensitivity is quite simple: the free photoelectrons traveling in solids are very easily scattered from the many bound electrons in the solid and lose some fraction of their kinetic energy in the process. Thus, only those photoelectrons generated within the top few atomic layers have any significant probability of escaping the sample with a kinetic energy given by $hv\text{-}E_B$. Electrons which have lost some portion of their kinetic energy may enter the spectrometer and be detected, but will normally contribute only to the spectrum background and will not distort the chemical information in the spectrum. The exact depth sampled by the ESCA technique depends upon a number of parameters, including the sample matrix composition and the kinetic energy of the electron of interest. (This is discussed in detail in Section II.C). As a general rule, presently available data suggest the sampling depth of ESCA is ca. 30 to 100Å for organic samples, ca. 10 to 30Å for most inorganic compounds, and ca. 5 to 20Å for metals. The matrix dependency of the sampling depth makes quantitative interpretation

of peak areas difficult, and generally precludes absolute quantitative analysis except in cases where rigorous calibration is possible. However, in most cases, relative atomic concentrations at a sample surface can be determined with an accuracy of about ±10%.

B. Core Level Binding Energies

Reference Levels in Conducting Solids

Understanding reference levels for core electron binding energies in solids is an important consideration in spectra interpretation, and a short review of the subject seems appropriate.

For an isolated atom in the gas phase, each photoionization process can be described (neglecting recoil terms) by the simple conservation of energy equation:

$$E_{b_v} = h\nu - E_{k_v} \quad (1)$$

where $h\nu$ is the energy of the X-ray photon, E_{k_v} is the kinetic energy of the photoelectron, and E_{b_v} is the binding energy of the electron referenced to the vacuum level. However, in the case of solid samples, additional terms must be considered in the energy equation. Figure 1 shows a typical energy diagram for an electrically conducting sample in contact with the spectrometer. The left and right sides of the figure refer to the sample and spectrometer energy levels, respectively. For the sample, the X-ray photon energy can be partitioned among: (1) E_{b_f}, the binding energy of the core level of interest referenced to the Fermi level, (2) ϕ_{sa}, the work function of the sample, and (3) E_{k_v}, the kinetic energy of the photoelectron. During the experiment, the photoelectron will be accelerated from E_{k_v} to E'_{k_v} (left side of Figure 1) by an amount equal to the so-called "contact potential," or the difference between the sample and the spectrometer work functions. Thus, E_{b_f} can be calculated from:

$$E_{B_f} = h\nu - E'_{k_v} - \phi_{sp} \quad (2)$$

Note that the work function of the sample need not be known to determine E_{b_f}. As discussed below, this makes the Fermi level an experimentally convenient reference, and binding energies of core electrons in solids are normally referenced to the Fermi level.

Unfortunately, there is some controversy[17,18] as to whether E_{b_f} is the best value to use for comparison with quantum calculations, or even with chemical parameters such as oxidation state. It has been suggested that better correlation of binding energies with these parameters may be possible when E_{b_v} is used in place of E_{b_f}. To determine E_{b_v} for core electrons in solids, however, the sample work function must be known and, except for metals and a few other pure materials, very little work function data exist in the literature. Consequently, in an analytical laboratory, ϕ_{sa} would need to be measured directly for most samples. Measurement of ϕ_{sa} is not an easy problem experimentally[19,20] and would be impractical for routine analytical problems.

In addition, Citrin has noted that neither E_{b_f}

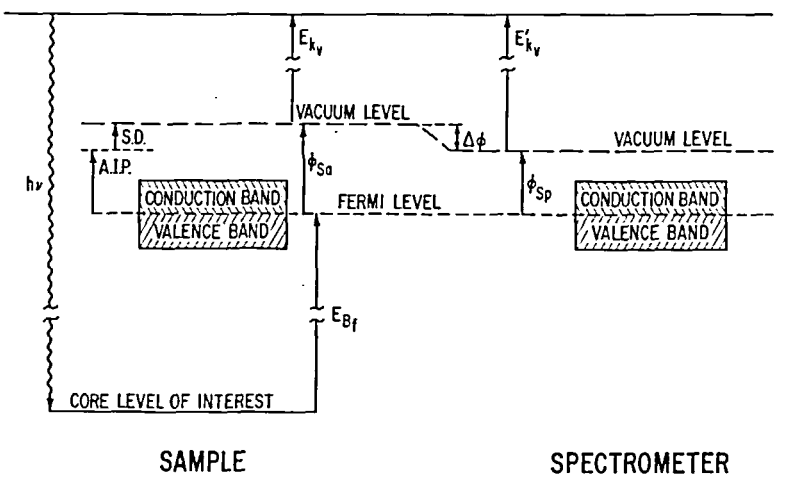

FIGURE 1. Energy level diagram for an electrically conducting solid in contact with a spectrometer.

nor E_{b_v} is the best value to use for comparison with theoretical calculations.[21] Referring to Figure 1, the work function associated with a given sample can be thought of as being composed of two terms, one term a property of the surface being analyzed, and the other a property of the bulk material. The surface term, called the surface dipole or SD in Figure 1, arises from the interaction of the photoelectron with the orbitals which protrude beyond the nuclear surface plane. For crystalline materials, the magnitude of the surface dipole potential depends not only upon the sample itself, but also upon the crystal face being examined. The bulk term contributing to the work function is called the average internal electrostatic potential, or AIP, by Citrin, and is the average potential experienced by the electron as it travels in the solid. Binding energies referenced to the AIP level have the most meaning theoretically where $E_{b_{AIP}}$ is defined as:

$$E_{b_{AIP}} = E_{b_v} - SD \quad (3)$$

or

$$E_{b_{AIP}} = E_{b_f} + AIP \quad (4)$$

Experimentally, however, it is not possible to separate the AIP and SD contributions to ϕ_{sa} and, unless one is dealing with a model system where either the SD or AIP terms can be calculated, the vacuum or Fermi reference levels are the only ones accessible. Thus, for each sample, the choice of vacuum or Fermi levels as a reference should be dictated by which term, SD or AIP, is thought to be the bigger contributor to ϕ_{sa} for that sample. If SD is larger, E_{b_f} will be closer to $E_{b_{AIP}}$ and, of course, the converse will be true if AIP is larger. As stated above, E_{b_f} is used almost exclusively because of convenience and is the only viable choice for an analytical laboratory.

2. Nonconductors and the Charging Effect

For the analytical chemist, the majority of the samples examined will not be electrically conducting and, in these cases, the reference level problem becomes more complex. The energy level diagram for a nonconductor in equilibrium with the spectrometer is shown in Figure 2. Nonconductors are characterized by a region between the top of the valence band and the bottom of the conduction band called the band-gap, whose magnitude (~1 to 4 eV) is much larger than kT at room temperature. For intrinsic semiconductors[22] and insulators, where the band structure is known and no impurity states are present, the Fermi level is statistically well-defined as being at a position one half the magnitude of the band-gap above the top of the valence band. For most samples handled in an analytical laboratory, however, the band structure and even the magnitude of the gap are unknown. Thus, the position of the Fermi level is unknown, and using the Fermi level as a reference for core electron binding energies becomes somewhat arbitrary in these cases.[23]

Complicating this picture for nonconducting samples is the problem of charging. During the ESCA experiment, the photoelectrons escaping the

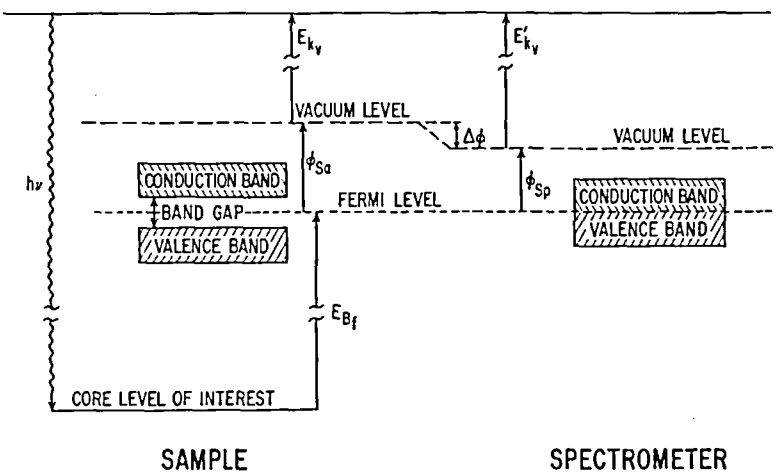

FIGURE 2. Energy level diagram for nonconductor in equilibrium with a spectrometer.

sample surface leave behind a positive charge and, because of the electrical properties of the sample, there may be no low resistance path available for electrons to flow from the spectrometer to the sample and neutralize the charge. Consequently, the sample charges positively, and the energy levels of the sample are shifted relative to the Fermi level of the spectrometer. In the absence of any electron return current, the sample would charge to some "breakdown" voltage, which might be as high as several hundred volts depending upon the sample. In an actual spectrometer, however, return current to the sample is supplied by photoelectrons generated from X-rays striking areas around the sample including, primarily, the metal foil window separating the X-ray tube from the sample. To a lesser degree, return current is also supplied by a conduction mechanism between the sample and spectrometer — possibly photoconduction across the surface of the sample. The net result of this charging current, i_c, and the sum of the discharging currents, i_d, is that a mean steady state potential, Q_{ch}, is rapidly established at the sample surface. Photoelectrons leaving the sample surface will then have a kinetic energy defined by:

$$E'_{k_v} = h\nu - E_{b_f} - \phi_{sp} - Q_{ch} \quad (5)$$

and the entire kinetic energy axis of the ESCA spectrum will be shifted from its true value. Although the magnitude of Q_{ch} will vary from sample to sample, for a constant X-ray tube current and anode voltage, Q_{ch} will be constant for a given sample during the ESCA analysis.

A number of methods are currently used to deal with the charging problem. These methods can be classified into two general types: (1) those which attempt to reduce Q_{ch} to a small value ($\leq$0.1 eV) — for example, by using extremely thin samples on a conducting substrate or by flooding the sample environment with low energy electrons, and (2) those methods which use an internal or external standard to measure the magnitude of Q_{ch}. Each of these is discussed separately below.

In the thin sample approach, ultrathin samples (one to several monolayers) are studied on a conducting support which is in electrical contact with the spectrometer. This method assumes that the resistance to bulk electrical conduction from the support to the sample surface will be sufficiently small to prevent charging. The validity of this assumption should be verified for each sample with a flood-gun or sample bias experiment (see below) since if the sample is not properly prepared, a significant, albeit small, Q_{ch} may be present at the surface during ESCA analysis.[24] Thin samples of this nature can be prepared by sputtering, vacuum deposition, or by depositing a small amount of a dilute solution containing the sample on the support and allowing the solvent to evaporate. Controlled chemical reactions with appropriate metals to produce the desired compounds as a thin layer on metal surfaces are also useful methods.[25] While this technique has considerable merit, it is not generally useful in an analytical laboratory since the original integrity of most sample surfaces must be maintained.

In the "flood-gun" approach,[26] an electron gun is used to bathe the sample in an excess of low energy electrons and thus provide another source of i_d to neutralize surface charge. This technique is of particular importance in instruments which, by design, have no window between the X-ray anode and the sample to act as a source of low energy electrons. The electron flood-gun is a simple piece of equipment, usually consisting of a tungsten filament, DC power supply, and a current meter. The filament is located near the sample, and a slit arrangement between the sample and the filament is used to limit the kinetic energy range of the electrons to a small value. By varying the filament current and voltage, the operator can qualitatively control the number and kinetic energy of the electrons surrounding the sample. The biggest disadvantage of the flood-gun technique is that a negative charge can be induced on the sample if the electron flux is too high or if the electron kinetic energies are too large. Consequently, there is no certain way to tell when the surface charge has been exactly neutralized, and by itself, the flood-gun approach does not provide an absolute reference level. Different samples have different total photoemission cross-sections which are related to i_c and, consequently, different values of i_d (and flood-gun filament current) will be required to exactly neutralize surface charge.

Another method to reduce Q_{ch} to small values has been suggested in the literature. This method is somewhat akin to the flood-gun approach in that the ratio of i_c to i_d is varied instrumentally. Ebel and Ebel[27] have shown that for the McPherson ESCA-36 spectrometer operated at a constant X-ray anode voltage, both i_c and the portion of i_d originating from the X-ray window are linear

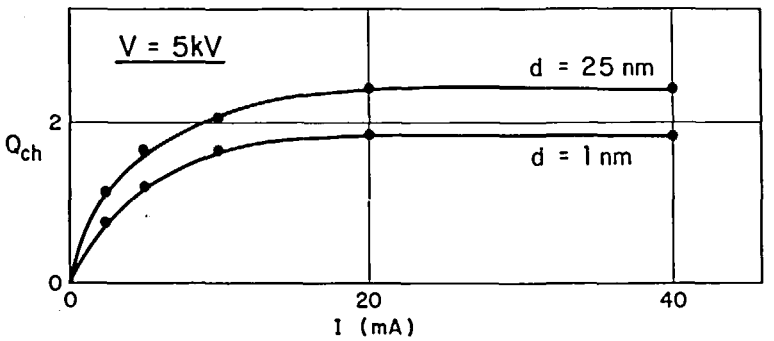

FIGURE 3. Sample charging vs. X-ray tube current at constant anode potential. [From Ebel, M. F. and Ebel, H., *J. Electron Spectrosc. Relat. Phenom.*, 3, 169 (1974). With permission.]

functions of the X-ray tube current, I. One would then expect that the difference between i_c and i_d, and thus Q_{ch}, would also be linear with I. In fact, another source of i_d, speculated to be photoconduction, adds to i_d from the window, with the result that Q_{ch} and I have the dependence shown in Figure 3. These authors give no experimental data for samples other than Teflon,* but they state that, for all cases studied, this Q_{ch} vs. I curve could be characterized by the equation:

$$Q_{ch} = A\frac{(BI)}{(I + BI)} \tag{6}$$

where A and B are constants for a given sample. From Equation 5, since $h\nu$, E_{b_f}, and ϕ_{sp} are independent of I, Q_{ch} in Equation 6 can be replaced by E'_{k_v}. A and B can then be determined for a given sample by fitting Equation 6 to a plot of E'_{k_v} vs. I and, in principle, a value of E'_{k_v} at I = 0 can be calculated which corresponds to zero surface charge. It is important to note, however, that Ebel and Ebel used external standards to determine the magnitude of Q_{ch}, and plotted Q_{ch} vs. I (rather than E'_{k_v} vs. I) because they found that negative sample charging was possible at low anode voltages. At a constant tube current, it was found that lowering the anode voltage by a factor of two decreased the total photoemission, and thus i_c, by much greater than a factor of two, while the contribution of i_d from the window remained essentially constant. At low anode voltages, i_d could be greater then i_c, and negative Q_{ch} was possible (see Figure 4). It is likely that the value of anode voltage above which negative charging is not possible will depend upon both the sample and the instrument design. Until these variables are better characterized, the authors feel that this approach, like the flood-gun, should be used only in conjunction with an external standard. An additional consideration for an analytical laboratory is that this technique requires spectra to be run at a number of power settings for each sample, which may not be practical because of the time involved.

Before continuing to the internal and external methods of charge correction, a word about differential charging is in order. Thus far, charging has been discussed in terms of an average potential, Q_{ch}, at the sample surface. In fact, nonconductors have a small distribution of charge over their surfaces which broadens the measured photoelectron line width and can be the limiting factor in resolution.[28] In general, the higher the absolute value of Q_{ch}, the larger the charge distribution will be. For the limiting case of differential charging, where one portion of a sample is in good electrical contact with the spectrometer and the remainder is not, separate distinct peaks can be observed in the spectrum. An illuminating example of this latter effect can be found in Grunthaner's study of vanadium diboride.[29] Figures 5A and 6A show the B_{1s} and V_{2p}-O_{1s} spectra, respectively, from a sample of VB_2. These spectra were taken using a spectrometer which had no window between the sample and the X-ray source for supplying i_d to the sample. Note that two boron peaks and three O_{1s} peaks are evident when the sample is examined

*Teflon – duPont Trademark for TFE-Fluorocarbon Resin.

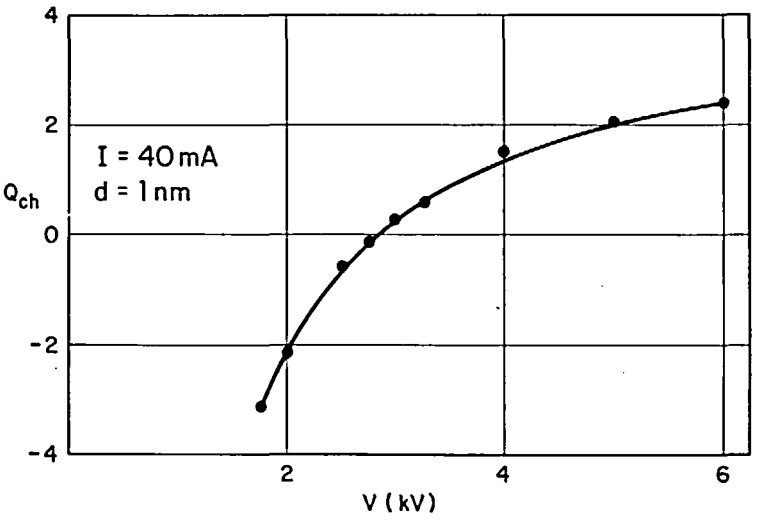

FIGURE 4. Sample charging vs. X-ray anode potential at constant tube current. [From Ebel, M. F and Ebel, H., *J. Electron Spectrosc. Relat. Phenom.*, 3, 169 (1974). With permission.]

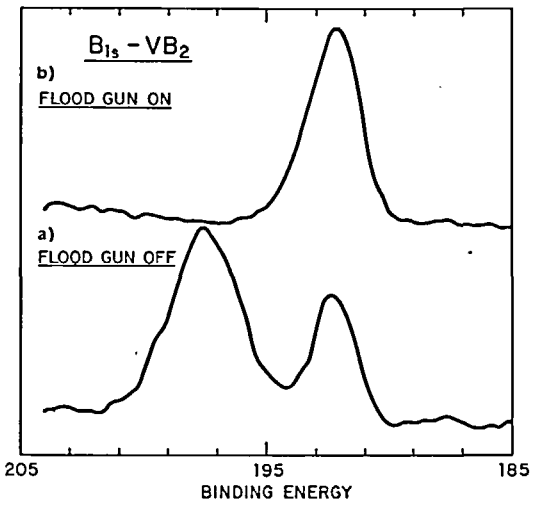

FIGURE 5. B_{1s} spectra from VB_2 with (a) flood gun off, and (b) flood gun on. (From Grunthaner, F. J., Ph.D. thesis, California Institute of Technology, Pasadena, 1974.)

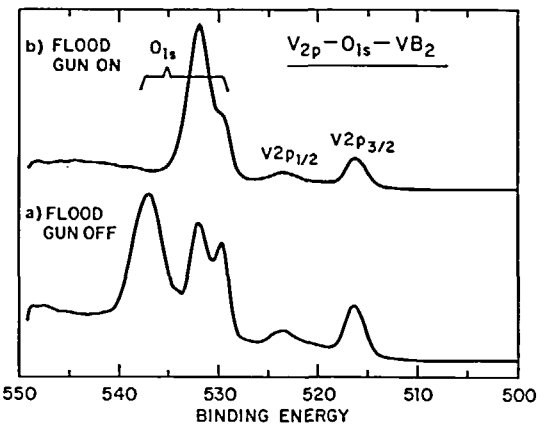

FIGURE 6. V_{2p}-O_{1s} spectra from VB_2 with (a) flood gun off, and (b) flood gun on. (From Grunthaner, F. J., Ph.D. thesis, California Institute of Technology, Pasadena, 1974.)

under normal conditions. When an electron flood-gun was operated simultaneously with the photoemission experiment (Figures 5B and 6B), the two boron peaks and two of the three oxygen peaks coalesced into single lines. Even though VB_2 is a good conductor, the boron-oxide coating on some of the particles was evidently electrically insulated from the remainder of the sample. The same conclusion was reached when the VB_2 was examined in a spectrometer which had an Al window between the X-ray source and the sample. Figure 7A shows the resulting V_{2p}-O_{1s} spectrum, which looks nearly identical to that in Figure 6b. Apparently, the i_d from the window is sufficient for charge neutralization of the nonconducting portion of the sample. When a DC potential is applied to the sample holder, photoelectrons originating from the conducting portion of the sample are shifted in the spectrum by an amount exactly equal to the applied potential as expected.

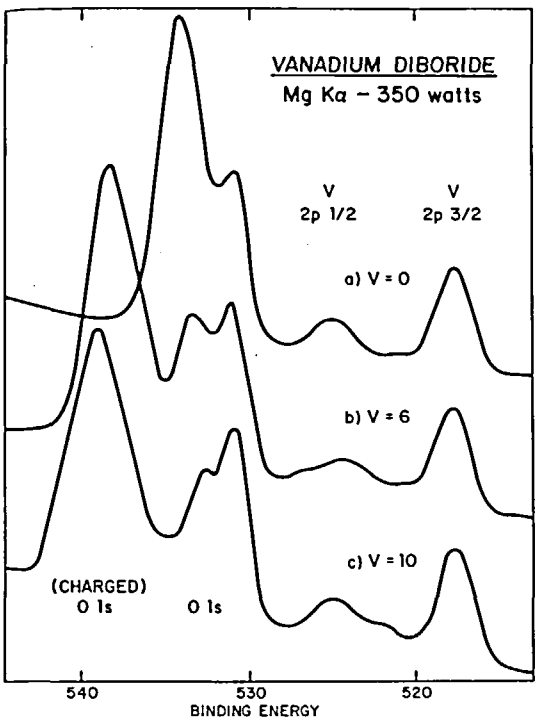

FIGURE 7. V_{2p}–O_{1s} from VB_2 with (a) zero applied potential, (b) 6 V applied potential, and (c) 10 V applied potential. (From Grunthaner, F. J., Ph.D. thesis, California Institute of Technology, Pasadena, 1974.)

Photoelectrons originating from the nonconducting portion, however, are shifted only slightly from their original kinetic energies. That they shift at all is due to a small effect which the applied potential has on the available i_d. Figures 7B and 7C show the resulting spectra for applied potentials of 6 and 10 V, respectively. These spectra have been normalized for the applied bias, and the differential charging noted previously in Figures 5A and 6A is again evident.

Clearly, care must be taken to insure that differential charging is not the source of multiple peaks in a spectrum. If the difference in binding energy between multiple peaks is constant with flood-gun current or with sample bias potential, the chemist can be reasonably sure that differential charging is not the cause of the multiple peaks.

As mentioned previously, the general approach to charge correction using internal or external standards is to take all spectra for each sample under a given set of instrumental parameters and, by measuring the apparent binding energy of a "standard" photoelectron line with respect to its true binding energy, determine the amount of charge at the surface of the sample. The fundamental assumption of the standards method is that the reference photoelectron line arises from an element in electrical equilibrium with the sample which can "follow" exactly (within ± ~0.1 eV) the charge on the sample surface.

In the internal standard method, the reference consists of an element that is part of the sample itself. In this case, the above assumption must be valid. The reference element, however, must be common to all the samples being analyzed and, most importantly, must not undergo a chemical shift from sample to sample. These latter two conditions are not always satisfied and greatly restrict the general applicability of the internal standard approach.

One good example of the internal standard approach can be found in the work by Ogilvie and Wolberg[30] on heterogeneous catalysts supported on alumina. These workers showed that for oxides of cobalt, nickel, copper, and zinc on α-alumina, a factor of ~3 to 10 more precision in binding energies was possible when the Al_{2p} photoelectron line was used as an internal standard for charge correction than when the external C_{1s} photoelectron line (see below) was used. The same improvement was even found in a number of spinels, where both tetrahedral and octahedral aluminum sites are present.

In the external standard approach, an element which is not common to the sample is used for charge correction. The C_{1s} hydrocarbon line at 285.0 eV, which is found on nearly all samples, has been used most commonly in the past.[1] Sample bias experiments (similar to that described above for VB_2), in which a potential is applied between the sample and the spectrometer, have been applied to nonconducting samples such as $BaSO_4$,[31] MoO_3,[32] and NaCl.[24] For each sample, as a function of applied potential, the position of the impurity C_{1s} photoelectron peak was shifted by the same amount as the photoelectron peaks from sample. This is good evidence that the C_{1s} external standard is in electrical equilibrium with the sample and follows the surface charge. Because of convenience, this C_{1s} line is still being used as a standard in many laboratories. As pointed out by several authors,[32] the problem with this standard is that one cannot always be certain of the origin of the carbon contamination and the same carbon species may not be present from sample to sample. Most commercial instruments today (see Section III) are pumped with "oil free" pumping systems, and the majority of carbon in these vacuum

systems is usually due to CO and CO_2 slowly desorbing from the chamber walls. Only a small amount of carbon is present as hydrocarbon. Thus, it is likely that this so-called "pump-oil" carbon detected by ESCA on many surfaces is not "pump-oil" at all, but arises from sorbed CO/CO_2 or from atmospheric contamination which occurred before the sample was placed in the spectrometer vacuum.

An alternate external standard approach to charge correction is to vacuum deposit a small amount of gold on each sample surface.[31] The magnitude of Q_{ch} is calculated from the difference between the observed binding energy for the $Au_{4f_{7/2}}$ peak and the commonly accepted value of 83.8 eV. Except in the case of ultraclean surfaces, gold vapor deposition proceeds initially by a nucleation process which results in the formation of electrically isolated islands of gold on the surface. The key assumptions in this charge correction method are (1) that the gold islands follow the surface charge, and (2) that the gold does not react with the sample. These two assumptions are generally valid since gold is relatively inert, and bias-potential experiments which alter Q_{ch} in the spectrometer have shown that the gold islands do follow the surface charge[31,32], at least at low gold concentrations. Exceptions to both assumptions have been pointed out in the literature, however. Betteridge, Carver, and Hercules[33] have shown that in some systems, the width and position of the gold peaks can change with sample, time of deposition, and probe temperature, indicating that the gold is reacting with the sample. In addition, Ginnard and Riggs[34] have shown that for gold deposited on polyethylene (PE) and polytetrafluoroethylene (PTFE) films, the magnitude of Q_{ch} increases as the amount of gold deposited on the polymer surfaces increases – probably because the higher total photoelectric yield of gold compared to that of the polymers results in larger i_c values with increasing gold coverage. An even more serious problem is that the electrical equilibrium between the gold and the polymers appears to shift significantly with increasing amounts of deposited gold. The ΔE_B between (1) the F_{1s} and C_{1s} peaks in PTFE, (2) the C_{1s} and $Au_{4f_{7/2}}$ peaks in PE, and (3) the C_{1s} and $Au_{4f_{7/2}}$ peaks in PTFE is plotted in Figure 8 as a function of the amount of gold on the two surfaces (expressed as % surface coverage). Open circles, filled circles, and triangles

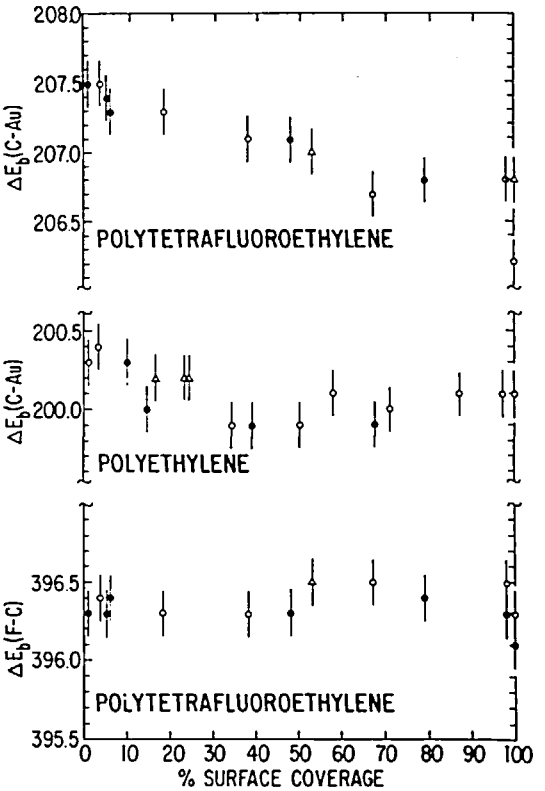

FIGURE 8. Differences in binding energies, ΔE_B, between selected peaks in PE and PTFE as a function of the amount of gold deposited on the polymer surfaces. [From Ginnard, C. R. and Riggs, W. M., *Anal. Chem.*, 46(9), 1306 (1974). With permission.]

represent data taken on three different samples of each polymer. As a function of gold coverage, the ΔE_B between the F_{1s} and C_{1s} peaks in PTFE remains constant within experimental error (σ = ±0.2 eV), as expected, since both peaks arise from the same molecular structure. The ΔE_B between the $Au_{4f_{7/2}}$ and C_{1s} peaks changes as a function of gold coverage by as much as ~0.8 eV for PTFE and ~0.5 eV for PE. It is clear that when using Au as an external standard, care must be taken to insure approximately equivalent coverage among samples, preferably at the low to moderate coverages which do not significantly enhance surface charging.

3. Chemical Shifts in Solids/Photoelectrons

Most of the early research in ESCA was sparked by the recognition that the exact binding energy of a photoelectron was related to the magnitude of the charge on the atom originating the photoelectron. In principle, if this chemical shift/atomic

charge relation could be quantified, photoelectron binding energies measured by ESCA could then be used as direct measures of atomic oxidation states and electron distributions in molecules. Since this chemical shift/atomic charge relationship was recognized, hundreds of atomic charge calculations on large numbers of chemical systems have been performed and compared with experimental binding energies. These calculations have ranged in complexity from simple Pauling electronegativity calculations[35] to *ab initio*[36] calculations using high quality wave functions. Many of these calculations have given excellent agreement with experiment, and many have not. It is not the purpose of this article to discuss these calculations in detail, and the reader is referred to the articles by Shirley[12] and Gelius[11] for more information on this subject. Instead, in this section, we will first present several examples of the chemical shift in solids in order to illustrate its usefulness in structure and oxidation state determinations. Secondly, those factors other than initial state charge which affect electron binding energies in solids are described in a qualitative fashion to alert the reader to some of the problems in correlating E_B with atomic charge in solids, and to assist him in understanding the latest literature in this area.

The chemical shift effect in ESCA can be illustrated qualitatively by considering the carbon atoms in the organic polymers, polyethylene (PE) $(-CH_2-CH_2-)n$ and polytetrafluoroethylene (PTFE) $(-CF_2-CF_2-)$. In PTFE, the carbon atoms are bonded directly to two electronegative fluorine atoms which pull electron density away from the carbon atoms and toward the fluorine atoms. This creates a net positive charge on the carbon atoms in PTFE and, compared to the C_{1s} level in PE, the C_{1s} level in PTFE is deshielded from the carbon nuclear charge. Electrons in the C_{1s} level of PTFE are thus held more tightly by the nuclear charge and exhibit a higher binding energy than electrons in the C_{1s} level of PE. Experimentally, the PTFE C_{1s} peak is found at ~8 eV higher binding energy than the C_{1s} peak for PE.[37] Another good example of chemical shifts in organic materials is found in Figure 9, which shows the C_{1s} and O_{1s} spectra from a commercial polyester film. Three peaks are evident in the C_{1s} spectrum. The origin of these peaks is easily discerned from polymer structure, relative peak intensities, and simple electronegativity considerations. The largest peak at ~285 eV is due to the ring carbons which are bound only to hydrogen and other carbon atoms. The shoulder at ~287 eV on the large peak is due to the methylene carbons which are bound directly to 1 oxygen atom, and the highest binding energy peak at ~289 eV is due to the carboxyl carbon atoms. The O_{1s} spectrum from the polymer is also shown in Figure 9. Here, two peaks with ~1:1 relative intensities are evident and correspond to the two types of oxygen in the polymer.

Figure 10 shows a palladium spectrum from palladium black which illustrates the chemical shift in inorganic solids. The 3d level in palladium is split into a natural doublet ($3d_{3/2}$ and $3d_{5/2}$) due to spin-orbit coupling. Two peaks are found in each of these levels, with the higher E_B peaks being due to palladium oxide (Pd^{II}) on the surface of the palladium black, and the lower E_B peaks to the palladium metal (Pd^{o}) substrate.

The potential model equation for photoelectrons can be written as:

$$E_B = k Q_a + 1 + V_a \tag{7}$$

where E_B is the binding energy for a core electron in atom a, Q_a is the initial state charge on atom a, k is a constant for the core level of interest in atom a, and 1 is a constant determined by the reference level; V_a is given by:

$$V_a = \sum_{b \neq a} q_b / r_{ab} \tag{8}$$

where q_b is the initial state charge on atom b, r_{ab} is the distance between atoms a and b, and the summation is taken over all atoms in the sample except atom a. In practice, k and 1 are treated as adjustable parameters for a given core level electron and are determined from a least squares fit of calculated versus observed binding energies for a large number of compounds. V_a is a Madelung potential term and represents the potential found at atom a due to charges on all the other atoms surrounding atom a.

It is obvious from Equation 7 that the quantity $(E_B - V_a)$, not E_B alone, should be linear with Q_a. Calculating V_a can be a problem in solids since, as opposed to the gas phase, all atoms, not just those in the molecule of interest, must be considered. For model solids of known structure, V_a can be calculated directly but, for most analytical samples, this will not be possible. Fortunately, studies in the literature for many core electrons

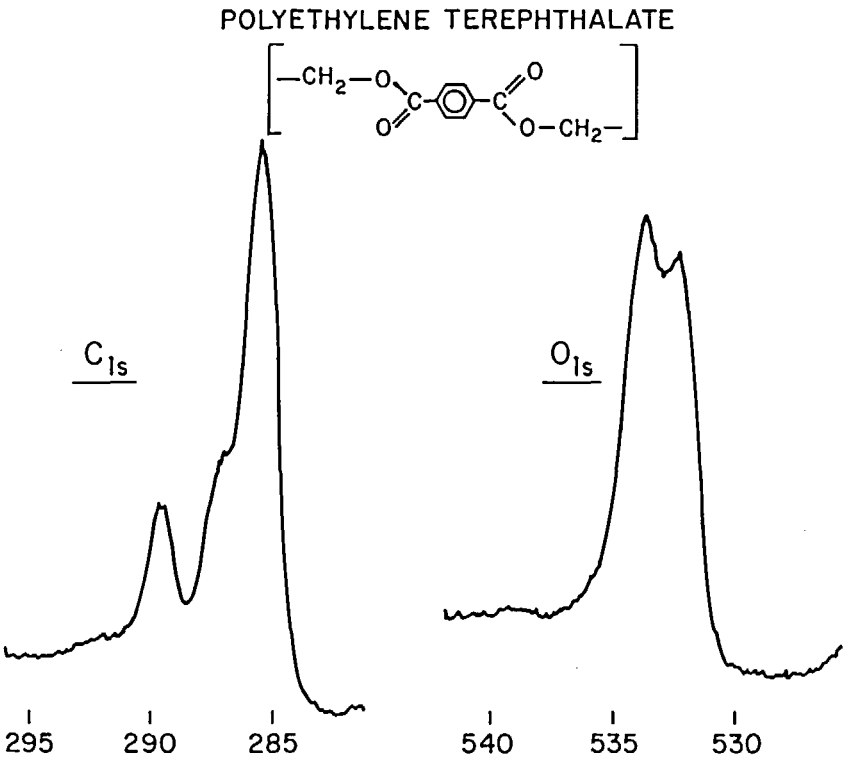

FIGURE 9. C_{1s} and O_{1s} spectra from polyethyleneterephthalate.

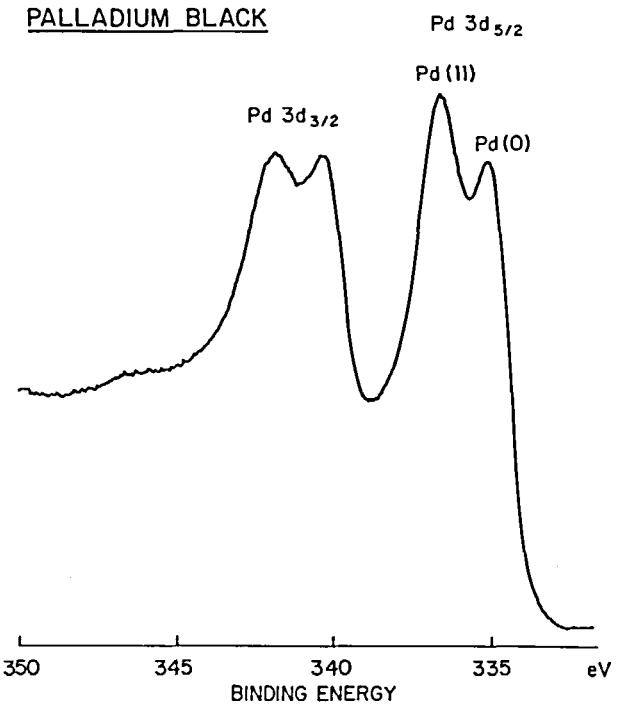

FIGURE 10. $Pd_{3d_{3/2-5/2}}$ spectrum from palladium black.

have shown empirically that the V_a contribution in Equation 7 is either negligible or nearly constant since good linear fits between E_B and Q_a have been obtained. For some atoms where a plot of E_B vs. Q_a does not give a good fit, an assignment of oxidation state based on binding energies alone may not be unambiguous, and other characteristics in the spectrum must be used to obtain chemical information. In cases where the E_B/Q_a correlation is poor, significant variations in the V_a term from sample to sample may be one cause of the poor correlation.[11]

Other reasons for a poor correlation of E_B with Q_a or oxidation state arise from so-called final state effects. Thus far, photoelectron binding energies have been discussed only in terms of initial state charges. However, as in all spectroscopic techniques, ESCA measures the energy difference between an initial and a final state, and observed chemical shifts are a measure of some average charge on the atom in the initial and final states, not of initial state charge alone. E_B can be written as:

$$E_B = E_I - E_F \tag{9}$$

where E_I and E_F are the total energies of the initial and final states, respectively. In early calculations of chemical shifts, it was assumed that a frozen-orbital approximation (Koopman's theorem)[38] could be used in describing the final state. This method assumes that the photoionization process is sufficiently fast that other electrons in the atom (or matrix) do not have time to relax toward the hole created in the electron shell by the ionization. Under this assumption, only initial state atomic charges are important in determining chemical shift since the final state energy can be given in terms of the initial state energy as:

$$E_F = E_I - \delta \tag{10}$$

where δ is the energy of the photoelectron in the initial state atom before ionization. As evident from Equation 9, δ must be equal to E_B. More recent work indicates that significant polarization or relaxation of electrons toward the photohole can occur,[21,39] and that Equation 10 is not an adequate description of the final state. This relaxation can involve both other core electrons in the same atom and "extra atomic" electrons in the solid. The effect of this electron relaxation is to screen the photoelectron from the positive charge

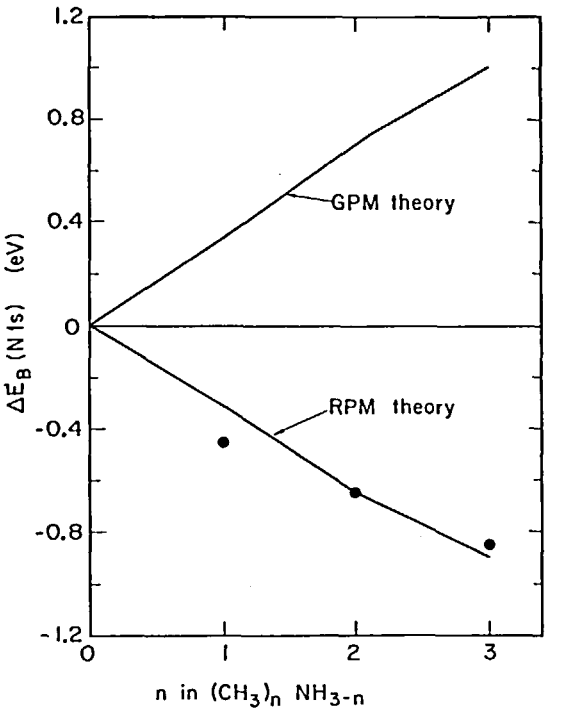

FIGURE 11. Calculated N_{1s} binding energies without (GPM) and with (RPM) relaxation terms for NH_3, NH_2CH_3, $NH(CH_3)_2$, and $N(CH_3)_3$. Experimental data shown as points. [From Davis, D. W., Banna, M. S., and Shirley, D. A., *J. Chem. Phys.*, 60(1), 237 (1974). With permission.]

at the nucleus. Thus, the photoelectron exhibits a higher kinetic energy (lower E_B) than it would have if no relaxation occurred. Calculated atomic charges which both include and exclude relaxation effects have been compared with experimental chemical shifts, and in most studies, those which include a relaxation term give better agreement with experiment. A striking example illustrating the effect of electron relaxation can be found in Shirley's study of N_{1s} binding energies in the series NH_3, NH_2CH_3, $NH(CH_3)_2$, $N(CH_3)_3$ (Figure 11).[39] Calculations using a ground state potential model (GPM – no relaxation) predict N_{1s} chemical shifts in a direction opposite to that predicted by calculations using a relaxation potential model (RPM). The experimental order of shifts agrees generally with the RPM calculations.

In summary, chemical shifts of photoelectrons in solids are related to initial state atomic charges and oxidation states, but reference level and sample charging problems, Madelung terms, and electron relaxation can also be important in determining peak positions. For many atoms in

solids, chemical shifts determine oxidation states unambiguously. For other atoms, they do not. In these cases, other characteristics of the ESCA spectrum such as Auger parameters, shake-up satellites, and multiplet structure due to exchange coupling can often be used to obtain chemical information. Published photoelectron binding energies for a large number of solid compounds have been summarized in Reference 40.

4. Chemical Shifts in Solids/Auger Electrons

A core level ionized atom has two competing processes by which it can relax. The first step in the relaxation is the same for both processes: namely, an electron from a higher energy level (level 2) falls into the core level hole (level 1) created by the ionization. The energy released in this transition can be emitted by the atom either as an X-ray photon or as an Auger electron from a third atomic level (level 3). If a photon is emitted, its energy will be characteristic of the atom and approximately equal to the difference in binding energy between levels 1 and 2. Detection of these photons forms the basis of the X-ray fluorescence technique. If an Auger electron is emitted, its kinetic energy will also be characteristic of the atom and will be approximately given by:

$$E_K \cong E_{B_1} - E_{B_2} - E_{B_3} \qquad (11)$$

Auger electrons are usually described as a KLL, LMM, MNN, etc. Auger electrons, where the letters KLL, etc. refer to the principal atomic energy levels 1, 2, and 3, respectively, involved in producing the Auger electron. Because core ionized atoms are produced in the ESCA experiment, peaks due to Auger electrons are also detected in the ESCA spectrum. Auger peaks can be easily separated from photoelectron peaks because their kinetic energies do not depend on excitation energy. Thus, they exhibit no X-ray satellite structure and have the same kinetic energies when either Mg or Al k_α radiation is used for photoexcitation. In addition, Auger peaks are broader in general than photoelectron peaks, particularly when levels 2 and 3 are valence band levels. For the remainder of this section, we will only be concerned with core-type Auger electrons, i.e., those in which levels 1 to 3 are all core levels.

Early observations of chemical shifts in Auger kinetic energies for a limited number of systems indicated that the magnitudes and directions of the Auger shifts were about the same as those found for photoelectrons, and for some time, Auger peaks in the ESCA spectrum were regarded as more of a nuisance than anything else. However, more recent studies[41,42] have found that Auger shifts are abnormally large for metal-metal oxide pairs. For example, although the $Zn_{2p_{3/2}}$ binding energies are nearly identical for zinc metal and zinc oxide, the Zn LMM Auger spectrum exhibits a shift of ~4.6 eV between the two. Figure 12 shows a portion of the Zn LMM spectrum for a thin layer of ZnO on Zn^0. Peaks due to both Zn^0 and Zn^{II} are clearly evident. Wagner has summarized the Auger and photoelectron binding energies for 13 metal-metal oxide pairs (Table 1) and has illustrated the generality of the large relative Auger shifts in these systems. These Auger shifts have been investigated theoretically[43] and are ascribed almost entirely to much larger extra-atomic electron relaxation in the doubly charged final state for Auger emission compared to the singly charged final state for photoelectron emission. Large Auger shifts have also been found between nonconducting salts.[44,45] Columns 2 and 3 of Table 2 list the Na_{1s} and sodium KLL Auger binding and kinetic energies, respectively, for sodium metal and 10 insulating sodium salts as determined by Wagner. Chemical shifts in the Na_{1s} binding energies for the insulating compounds vary only within a range of ~0.5 eV, while the corresponding Auger shifts vary over a range of ~3.5 eV and are nearly characteristic of the compound.

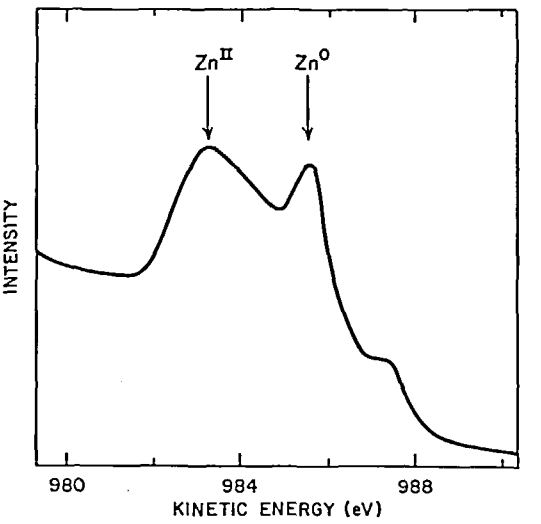

FIGURE 12. Portion of the Zn LMM Auger spectrum for a thin layer of ZnO on a Zn^0 substrate.

Wagner has proposed the "Auger parameter," α,

TABLE I

Photoelectron and Auger Shifts for Metal–Metal Oxide Pairs

	Photoelectron binding energy (eV)		Auger apparent binding energy (eV)		Auger transition
	2p	3d	Mg Anode	Al Anode	
Mg	49.8		–	300.8	KLL
MgO	51.2		–	307.2	
Al	72.8		–	93.5	
Al_2O_3	75.4		–	100.2	
Zn		9.9	261.0	494.0	LMM
ZnO		10.7	265.6	498.6	
Ga		18.5	185.3	418.3	
Ga_2O_3		19.7	190.8	423.8	
Ge		29.4	108.5	341.5	
GeO_2		33.2	116.3	349.3	
As		42.05	–	261.85	
As_2O_3		45.8	–	268.6	
Se		55.5	–	179.7	
Na_2SeO_3		58.3	–	185.2	
Ag		374.0	895.2	1128.2	MNN
Ag_2SO_4		374.2	899.2	1132.2	
Cd		411.55	869.7	1102.7	
CdO		411.65	873.4	1106.4	
In		451.8	843.3	1076.3	
In_2O_3		452.3	846.0	1079.0	
Sn		492.9	815.3	1048.3	
SnO_2		494.6	820.4	1053.4	
Sb		537.3	789.2	1022.2	
Sb_2O_3		539.2	793.7	1026.7	
Te		583.7	761.9	994.9	
TeO_2		587.2	767.1	1000.1	

which is defined as the difference in kinetic energy between the Auger and photoelectron peaks, as a useful measure for identifying chemical species. Values for α are listed in the fourth column of Table 2 for the sodium compounds and, although shifts in α ($\Delta\alpha$) are nearly the same as the Auger shifts (ΔE, Auger), $\Delta\alpha$ has an important practical advantage over ΔE, Auger. Because α is calculated from a difference in peak positions, there are no reference level or sample charging problems to be concerned with, and α can be easily measured with ±0.1-eV accuracy. Wagner has demonstrated that the Auger parameter has a large range for all elements which give sharp core-type Auger peaks and which are accessible with Al k_α radiation. These elements include Ne, Na, Mg (KLL), Ar, K, Ca (LMM), Cu^{+1}, Zn, Ga, Ge, As, Se (LMM), Ag, Cd, In, Sn, Sb, Te, and Xe (MNN). With higher energy incident radiation, the Auger parameter might be extended to Al, Si, P, S, Cl (KLL), Br,

TABLE 2

Chemical Shifts and the Auger Parameter for Sodium Compounds (Al Kα Radiation)

Chemical form	Na_{1s} E_B	$KL_{23}L_{23}$ E_K(Auger)	α	ΔE_B(PE)	ΔE(Auger)	$-\Delta\alpha$
Na(S)	1071.7	994.2	579.3			
NaI	1071.4	991.4	576.2	−0.3	2.8	3.1
NaBr	1071.5	990.8	575.7	−0.2	3.4	3.6
NaCl	1071.4	990.5	575.3	−0.3	3.7	4.0
NaSCN	1071.1	990.7	575.2	−0.6	3.5	4.1
Na_2SO_3	1071.1	990.6	575.1	−0.6	3.6	4.2
$NaNO_2$	1071.4	990.0	574.8	−0.3	4.2	4.5
Na_2SO_4	1071.0	990.0	574.4	−0.7	4.2	4.9
$NaNO_3$	1071.2	989.8	574.4	−0.5	4.4	4.9
NaF	1071.0	988.8	573.2	−0.7	5.4	6.1
Na_2SiF_6	1071.5	987.9	572.8	−0.2	6.3	6.5

Kr, Pb, Sr, Y, Zr, Nb, Mo (LMM), and all heavy metals (MNN).

5. Final State Sources of Multi-line Structure/ Shake-up

Core electron chemical shifts from an element in two or more oxidation states are not the only possible sources of multi-line structure in an ESCA spectrum. Substituting Equation 9 into Equation 1 and solving for kinetic energy gives:

$$E_K = h\nu - (E_I - E_F) \quad (12)$$

From this equation it becomes obvious that even when all atoms of a particular element in a sample have the same oxidation states and initial state energies, if more than one discrete final state is possible, more than one photoelectron kinetic energy will be possible, and more than one peak will be observed in the spectrum. Electron shake-up transitions and exchange splitting due to unpaired electrons are the two main phenomena in photoionization responsible for multiple final states. Peaks due to shake-up or exchange splitting are usually referred to as "intrinsic" peaks because they arise from the photoionization process itself. [This is opposed to "extrinsic" energy loss peaks (see Section I.B.) which arise from discrete, inelastic electron scattering processes occurring after photoionization has taken place and the electron is moving through the solid.] The physical bases of shake-up and exchange splitting and their analytical usefulness for oxidation state measurements in solids are discussed below.

During the photoionization process, the electrons in an atom experience a sudden change in potential which, in some cases, can excite a second electronic transition involving one of the outer or valence electrons and some bound, normally unfilled orbital. This electron shake-up transition results in a satellite in the spectrum occurring at lower kinetic energy (higher E_B) than the main photoelectron peak. The area of this satellite relative to the area of the main peak is a measure of the shake-up probability of occurrence, and the energy difference between the satellite and main peak is the energy of the shake-up transition. Shake-up satellites are most common in core level spectra of first row transition elements,[46] but have also been observed in a few heavy elements (eg., La, U)[47] and a few organic systems.[48]

In systems where this occurs, shake-up satellites often provide useful chemical information. For example, Tolman et al.[49] and Matienzo et al.[50] have shown that the $2p_{1/2\text{-}3/2}$ spectra of high spin Ni^{II} (d^8) compounds always exhibit strong shake-up satellite structure, while low spin Ni^{II} and Ni^0 compounds do not. A dramatic illustration of this effect can be seen in the $Ni_{2p_{3/2}}$ spectra of $[(C_6H_5)_2(C_2H_5)P]_2NiBr_2$ shown in Figure 13. The stable isomer of this compound at room temperature exhibits tetrahedral coordination geometry and is high spin. The spectra exhibit the satellite structure characteristic of the high spin state. The square planar isomer can be prepared by precipitation from solution at −78°C. Conversion to this isomer causes the satellite structure to disappear consistent with its low spin nature.

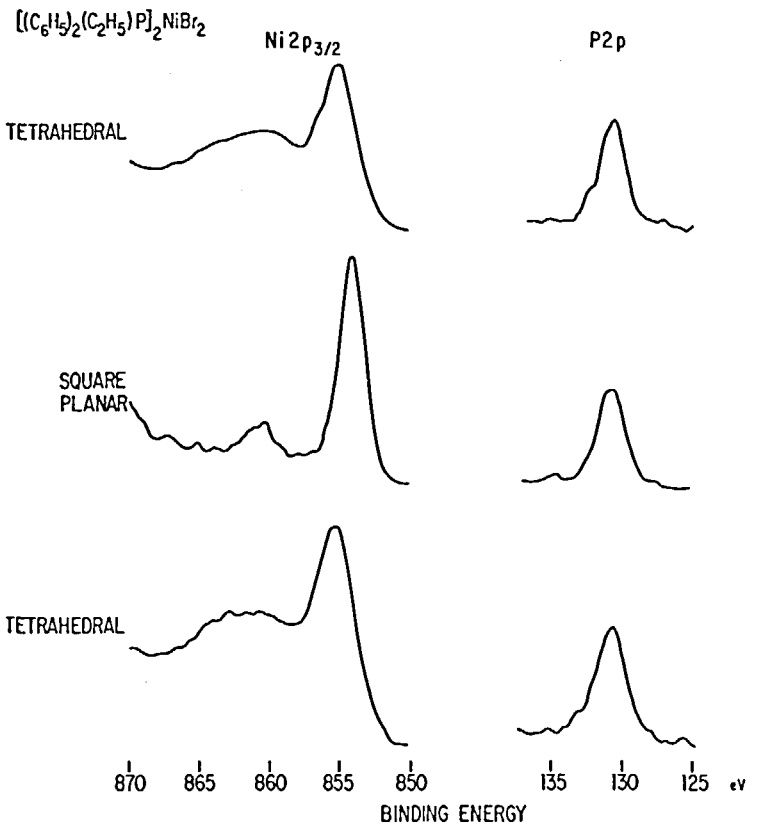

FIGURE 13. $Ni_{2p3/2} - P_{2p}$ spectra for $[(C_6H_5)_2(C_2H_5)P]_2NiBr_2$ in square planar (low spin) and tetrahedral (high spin) configurations.

Warming causes a solid state isomerization to the tetrahedral form and the reappearance of the shake-up satellite structure. Similar studies on a large number of copper compounds have shown that shake-up satellites occur in the $2p_{1/2-3/2}$ spectra of all Cu^{II} species, but are absent in the spectra of Cu^{I} and Cu^{0} compounds.[51] In addition, for both nickel and copper, the shape of the satellite structure differs somewhat among different compounds and appears to be characteristic of the ligand or anion bound to the metal. (This fact has been used as evidence that at least a portion of the shake-up satellite structure is due to a ligand to metal charge transfer excitation.[52]) Figure 14 compares the $Ni_{2p_{1/2-3/2}}$ spectra from $NiCl_2$ and NiO. Both compounds are high spin Ni^{II} and exhibit shake-up satellites in their spectra. The satellite structure is sufficiently different in the two spectra, however, that it can easily be used to distinguish one compound from the other.

6. Final State Sources of Multi-line Structure/ Exchange Splitting

When unpaired electrons are localized on an atom being studied by ESCA, each core level spectrum from that atom can exhibit multiple peaks due to exchange coupling of the unpaired electrons with the photohole.[53] Consider the Mn_{3s} spectrum from MnF_2 shown in Figure 15 as an example.[54] The Mn^{II} ion has 5 unpaired d electrons, and the final state for 3s photoemission ($3s^1 3p^6 3d^5$) can be either a ^7S or ^5S state, depending upon whether the 3s electron remaining after photoionization has its spin parallel to (^7S) or antiparallel to (^5S) the d electrons. The ^7S state is slightly lower in energy than the ^5S state because exchange interaction between electrons with parallel spins reduces the electron-electron coulomb repulsion. The two large peaks observed in the Mn_{3s} spectrum of MnF_2 correspond to the two final states, with the higher intensity ^7S peak found at lower binding energy, as expected. (The two small peaks are due to ^5S states with other electron configurations.) The separation between the ^7S and ^5S peaks is equal to the energy difference between the 2 final states and is proportional to the quantity (2S + 1), where S is the total spin on the metal atom in the final state.

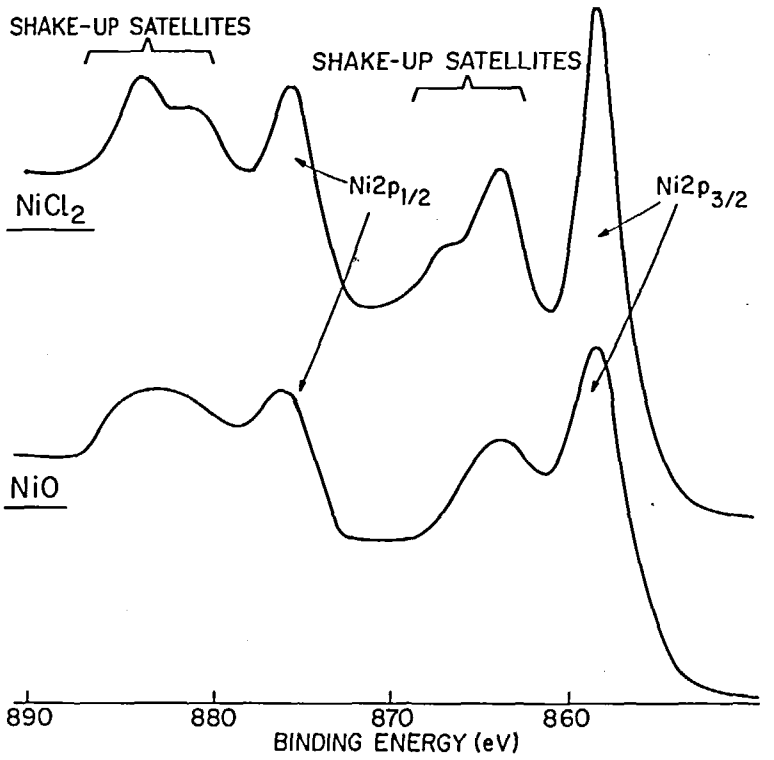

FIGURE 14. $Ni_{2}P_{1/2-3/2}$ spectra for $NiCl_2$ and NiO.

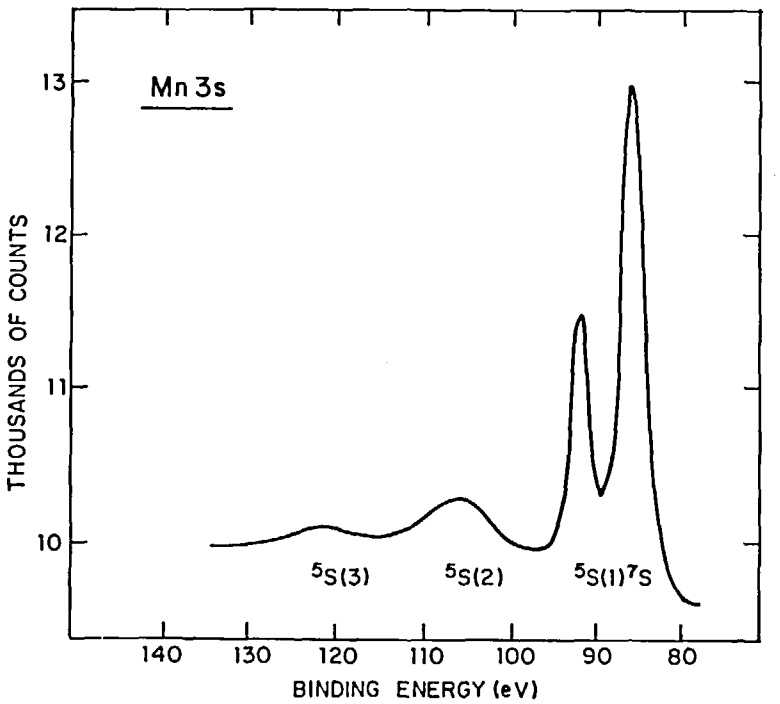

FIGURE 15. Mn_{3S} spectrum from MnF_2. [From Kowalczyk, S. P., Ley, L., Pollak, R. A., McFeely, F. R., and Shirley, D. A., *Phys. Rev. B:*, 7, 4009 (1973). With permission.]

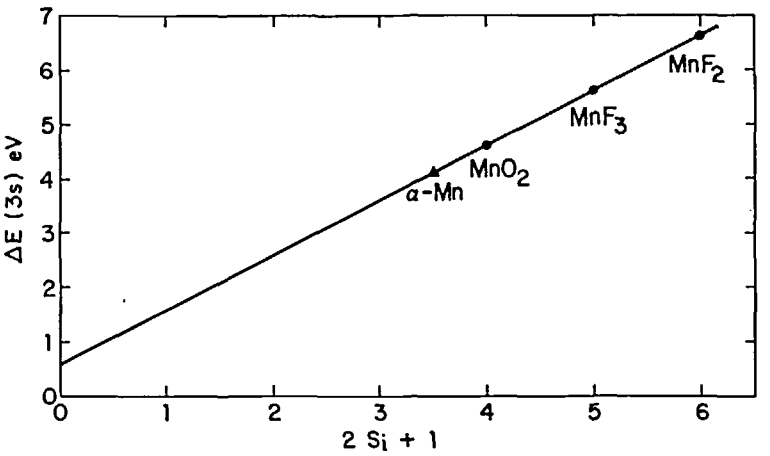

FIGURE 16. Mn_{3S} ^5S and ^7S separation, $\Delta E_B'$ vs. 2Si + 1 for MnF_2, MnF_3, MnO_2, and α-Mn. [From McFeely, F. R., Kowalczyk, S. P., Ley, L., and Shirley, D. A., *Solid State Commun.*, 15, 1051 (1974). With permission.]

If it can be assumed that the spin density on the atom is the same in the initial and final states, then for a series of compounds of a particular paramagnetic metal, the splitting of the peaks in the ESCA spectrum should be related to the total spin on the metal or to the covalent character of the metal-ligand bond.

Qualitative trends of the magnitude of the 3s splitting with total spin and metal-ligand covalent character have been reported in the literature for Cr, Fe, and Mn.[55] Kowalcyzk et al.[56] have used the Mn_{3S} splitting found for α-Mn metal, compared with those found for MnF_2 (Mn^{II},d^5), MnF_3 (Mn^{III},d^4), and MnO_2 (Mn^{IV},d^3), as evidence of a localized magnetic moment in α-Mn metal (see Figure 16). The reader is cautioned, however, that the relationship of total spin with core level splitting may not be characteristic of all paramagnetic metals. For example, no correlation of Cu_{3S} splitting with the covalent character of Cu^{II}-ligand bonds has yet been found.[51] Additional research on standard compounds is needed in this area.

B. Quantitative Analysis

In order to solve many problems related to surface chemistry, it is necessary to determine only qualitatively the major elements present on the surface and, in some cases, the oxidation states of these elements. Other problems require that relative or even absolute atomic concentrations be determined. A number of successful studies have appeared in the literature which use the ESCA technique for quantitative analysis. These studies include measurements of both surface and bulk compositions in such diverse areas as chemically treated polymer surfaces,[57] fluorochemicals sorbed on polymer fibers and films,[58] aluminum oxide films on aluminum foil,[59] electrodeposited metals,[60] metals chelated to fiberglass surfaces,[61] structural groupings in nitroso rubbers,[62] molybdenum oxidation states,[63] and gold-silver alloys.[64] These examples, as well as applications in our own laboratories, have shown that ESCA can be used routinely as a semiquantitative (< ±50% relative error) tool when relative atomic concentrations are compared among samples. Quantitative (< ±10% relative error) comparisons are also possible within a series of closely related samples.

This section of the paper discusses extrinsic and intrinsic energy loss processes[65] and demonstrates how differences in these processes from sample to sample can affect the accuracy of quantitative analysis. A simple model which can be used to obtain relative atomic concentrations at a sample surface is presented. The assumptions inherent in this model are critically examined, and some general guides for the analyst are suggested to aid in the quantitative interpretationof ESCA spectra.

1. Extrinsic Energy Loss Processes

In order to discuss quantitative surface analysis, it is necessary to have an understanding of the inelastic electron scattering processes which determine the effective sampling depth of the ESCA technique in solid samples. These inelastic electron scattering events are commonly referred to as

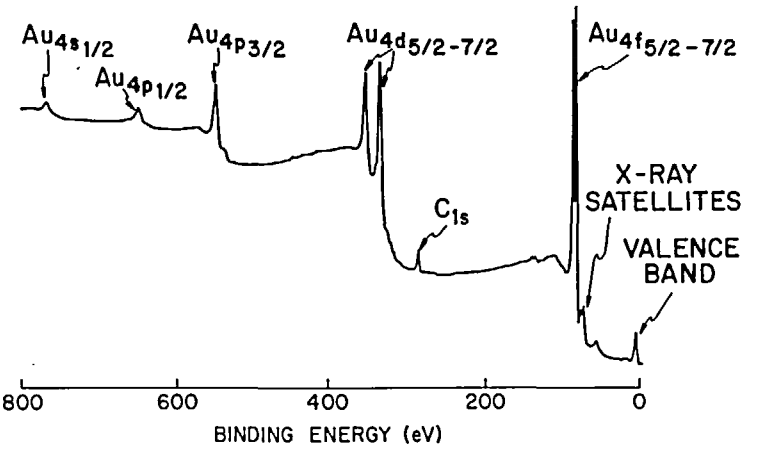

FIGURE 17. Partial survey scan from gold foil.

extrinsic events, as they occur after photoionization has taken place and the photoelectron is moving through the solid. Consider the broad "survey scan" of gold foil shown in Figure 17. Discrete photoelectron peaks are found in the spectrum for the valence band at near zero binding energy and, progressing toward higher binding energy, for each successive electronic level in the gold atom. A small amount of carbon contaminant is also present at the gold surface. Note, however, that these discrete peaks actually account for less than ~1% of the total number of electrons detected. There is a large increase in background to the left (lower kinetic energy) of each peak that is due to photoelectrons which, before escaping from the sample surface, have lost a portion of their kinetic energy by undergoing one or more inelastic scattering processes. This high probability for inelastic electron scattering is the property of electrons in solids that makes ESCA a surface-sensitive technique. Only those photoelectrons generated within the top few atomic layers of the sample have a significant probability of escaping the sample without losing a portion of their kinetic energy. Qualitatively, one can think of a number of inelastic events which can take place as a photoelectron (or any free electron) moves through a solid.[66] For example, the electron may scatter inelastically from a bound electron in the matrix by exciting it to some bound but normally unfilled state in the conduction band (e.g., interband transition) or to an unbound state (ionization). The free electron can also inelastically scatter from collective modes of electron (plasmon) or lattice (phonon) oscillations. Finally, inelastic interaction with other quantized particles (excitons, etc.) in solids may also be possible, but little is known about these interactions at present. It is important to note that each solid matrix will have a different ability to inelastically scatter electrons, depending upon the number and energies of the available transitions in that matrix. Thus, the inelastic mean free paths of photoelectrons in solids and, consequently, the sampling depth of the ESCA technique will vary from sample to sample.

Experimentally, it can be shown that the relative importance of different inelastic scattering mechanisms can change with different matrices. Figure 18 shows two 200-eV scans of aluminum encompassing both the Al_{2s} and Al_{2p} photoelectron lines. The lower spectrum is labeled "oxidized" and was taken using a sample of aluminum foil that had been exposed to the atmosphere. Both aluminum core levels are doublets with, in each case, the higher binding energy peak being due to the aluminum oxide layer on the surface of the foil, and the lower binding energy peak being due to the metal substrate. The upper spectrum is labeled "clean" and was taken on the same piece of aluminum foil after mechanically abrading the foil surface under a flowing stream of dry nitrogen. Although the oxide/metal doublets are still evident in the "clean" spectrum, substantially less oxide is present on this abraded surface when compared to the "oxidized" surface. Note the differences in the general shapes of the background for the two samples. First, the background in the "oxidized" sample is still rising at 250-eV binding energy, while it is falling in the "clean" sample. Even more striking, however, is the discrete structure evident in the "clean" foil spec-

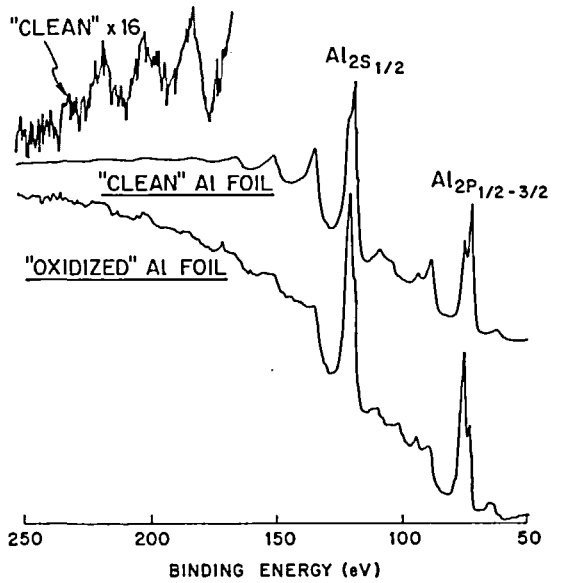

FIGURE 18. Al_{2S}–Al_{2p} and energy loss spectra for "clean" and "oxidized" aluminum foil.

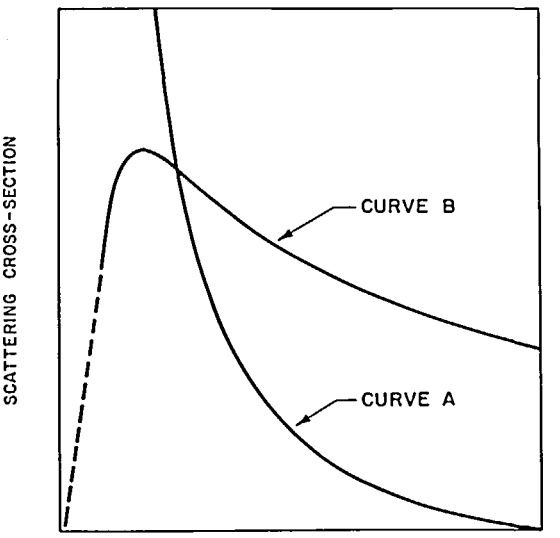

FIGURE 19. Dependence of inelastic electron scattering cross-section on (a) transition energy at constant electron kinetic energy, and (b) electron kinetic energy at constant transition energy.

trum. At least six discrete peaks at kinetic energies lower than the Al_{2S} line can be identified. Going towards lower kinetic energies, these peaks have successively lower intensities and are separated from one another by ~17.5 eV, the energy of the bulk plasma oscillation in aluminum. These peaks arise from Al_{2S} photoelectrons which, on escaping from the sample, have lost a discrete amount of energy (from 1 to 6 times ~17.5 eV) in scattering from the bulk plasmon in aluminum. The remaining structure in the "clean" spectrum can be assigned either to X-ray satellites or to surface or bulk plasmon loss structure associated with the Al_{2p} photoelectrons. Some of this plasmon structure can also be seen in a careful inspection of the "oxidized" spectrum, but it is clear from the general lack of discrete structure that a different inelastic electron scattering mechanism, probably electron-electron scattering, is important in the oxide layer. Different inelastic scattering processes will usually involve different excitation energies and a different number of total possible excitations. As will be shown below, the energy and number of possible excitations in a solid matrix determine the total probability for inelastic electron scattering in that matrix, and thus it is likely that the inelastic mean free paths of the Al_{2p} and Al_{2S} electrons are different in aluminum metal than in aluminum oxide.

For an electron moving in a solid, we can define a total inelastic scattering coefficient, S_j, which is related to the probability of that electron undergoing an inelastic event. S_j is usually given in units of $(\text{length})^{-1}$ and by definition is equal to $1/\lambda$. where λ is the inelastic mean free path of the electron in the solid. Wendt,[67] Wheeler,[68] and Powell[69] have separately derived equations relating the inelastic electron scattering coefficient to the kinetic energy of the photoelectron, E_K, and the electronic transition energy, E_{Tr}. These equations are generally similar in form and can be expressed by:

$$S_j = \frac{C}{E_K} \sum_{Tr} \frac{Z_{Tr}}{E_{Tr}} \left(\ln \frac{4E_K}{E_{Tr}} \right) \qquad (13)$$

where C is a normalization constant, Z_{Tr} is the number of electrons in the matrix which are available for some excitation of energy E_{Tr}, and the summation is carried out over all possible electronic excitations (where E_{Tr} is less than E_K) in the solid. Unfortunately, unless the complete filled and unfilled density of electronic states is known for a given sample, allowed values of E_{Tr} (and Z_{Tr}) will not be known, and Equation 13 cannot be solved exactly. Calculations using various approximations for Z_{Tr} and E_{Tr} have been attempted,[71] but none of these calculations can be applied presently to analytical samples. Even so, an inspection of Equation 13 gives us some qualitative information of value. Curve A of Figure 19 shows, from Equation 13, the general form of

the inelastic electron scattering coefficient versus the transition energy involved in a single inelastic event for a photoelectron with some known kinetic energy. It can be seen that the probability for inelastic electron scattering increases dramatically as the energy of the excitation gets smaller. Consequently, the number and energy of the unfilled states closest to the filled states, and the valence rather than the core electrons, will be important in determining the inelastic mean free path of a photoelectron in a solid. Curve B in Figure 19 plots the general form of the inelastic electron scattering coefficient versus the photoelectron kinetic energy for some known excitation in the matrix by the photoelectron. This curve rises from zero at some threshold corresponding to the excitation energy to a maximum at about three times the threshold energy, and then decreases with electron kinetic energy. (A dotted line is shown for the beginning of the curve as this portion is derived from experiment and is not well-described by Equation 13. According to Powell,[69] structure may be observed in this region.) Recalling from Equation 13 that the total inelastic scattering coefficient is composed of a sum of the individual coefficients for each possible inelastic event, the total inelastic electron scattering coefficient for a particular solid matrix will not be a smoothly varying function of the photoelectron kinetic energy. As the kinetic energy of the photoelectron increases, additional thresholds will be crossed, and the total probability for inelastic scattering will be increased by the addition of the new possible excitations. From Curve A, however, the probability of these additional excitations occurring, relative to the low energy transitions, becomes small very quickly as the threshold energy increases. This is the "saving grace" for quantitative surface analysis by ESCA. In the kinetic energy region of interest (~200 to 1500 eV), the additional excitations which become possible with higher and higher E_K result in very small perturbations to the total S_j vs. E_K curve, and in this kinetic energy region of the curve, S_j can be approximated by a smoothly varying function of $1/E_K$. Although the absolute magnitude of S_j can change dramatically from sample to sample, the E_K dependence remains approximately the same and, as pointed out below, relative photoelectron intensities can be compared from sample to sample.

2. Intrinsic Processes

Thus far, we have only considered extrinsic energy loss processes or those which occur after photoionization has taken place and the photoelectron is moving through the solid matrix. Intrinsic processes can also affect the number of photoelectrons from a core level detected at a particular kinetic energy. Intrinsic processes are those which occur during the ionization process, such as shake-up and multiplet structure due to unpaired electrons (discussed in Section II.A). These processes can partition the photoelectrons from a given core level into two or more kinetic energies. The intensity (and position) of a shake-up satellite relative to the main line can be very sensitive to local electronic effects and may change from sample to sample.[50] Thus, for quantitative analysis, it is necessary to sum the areas of all the peaks resulting from a single core level. In some cases, the distribution of final states is large enough that the resulting multipeak structure is broad and ill-defined, and measurements of the total area of the multipeak structure become difficult or impossible. Thus, core levels which are known from the literature to exhibit shake-up satellites (e.g., 2p levels in some first row transition metals) or multiplet effects with large energy separation (e.g., 2p and 3s levels in some first-row transition metals) should not generally be used for quantitative analysis even though they may be the most sensitive core levels for the atoms of interest. Less sensitive lines (e.g., 3p in some first row transition metals) which do not exhibit these effects are a better choice even though more time may be necessary to acquire a spectrum of good quality. If one is forced to use a core level that does exhibit intrinsic structure, summing the areas of all peaks appears to be the only present solution for quantitative analysis since the theory of shake-up and multiplet splitting cannot be applied routinely to most samples of analytical interest.

The effect of intrinsic processes on relative intensity ratios can be significant even when large intrinsic satellites are not immediately apparent in the spectrum. Table 3 lists the Na_{1s}/F_{1s} intensity ratios, corrected for stoichiometry, for seven different sodium and fluorine containing compounds. The ratios were determined both by Wagner[70] and by Swingle.[71] Swingle's ratios are somewhat higher than those measured by Wagner, possibly because of surface contamination effects. However, the same order of intensities is observed from compound to compound, and the amount of variance in the ratios is very large (~100%). The energy loss regions for the Na_{1s}, F_{1s}, and Na_{2s} levels were examined by Swingle to determine if

TABLE 3

Na_{1s}/F_{1s} Intensity Ratios from Varian-IEE

Compound	Wagner[+]	Swingle[++]
NaF	2.00	2.24
$NaBF_4$	2.59	3.43
Na_3FeF_6	1.48	1.86
Na_2SiF_6	2.14	2.26
Na_2GeF_6	2.33	2.70

[+]Data from Reference 70.
[++]Data from Reference 71.

differences in the discrete energy loss structure associated with the photoelectrons of each compound could account for these intensity ratio variations. Figure 20 shows the energy loss spectra for these electrons in NaF normalized for kinetic energy. The sodium 2s peak is included for energy reference purposes. A striking similarity in the loss regions of all 3 electrons is noted, with the first major energy loss occurring at approximately -11.0 eV. A comparison between these data and the 50-keV electron transmission experiments on NaF by Creuzberg[72] indicates that this is a plasmon loss. At 22.0 eV, sufficient structure for the harmonic process is also present for all 3 photoelectrons, but the remaining structure of each loss region is not solely accounted for by extrinsic energy loss processes. While there is qualitative agreement between the shapes of the sodium 1s and sodium 2s spectra, the fluorine 1s spectrum shows significantly more structure, including a large peak at 27.0 eV which is not visible in either sodium spectrum. Consequently, this peak must be due to one or more intrinsic processes, possibly shake-up, which are characteristic of the fluoride ion in NaF.

Figure 21 compares the F_{1s} energy loss spectra from $NaBF_4$ with NaF. The portion of the loss region exhibiting identifiable structure in $NaBF_4$ has been shaded to emphasize its approximate area relative to the area of the main photoelectron peak. It is apparent that any change in the intensity of the discrete energy loss structure from compound to compound can have considerable effect on the area of the photoelectron peak. For example, in Figure 21, note the large loss at 32.5 eV in the $NaBF_4$ spectrum which does not occur in NaF. This peak is likely due to some intrinsic process as it is not present with the same

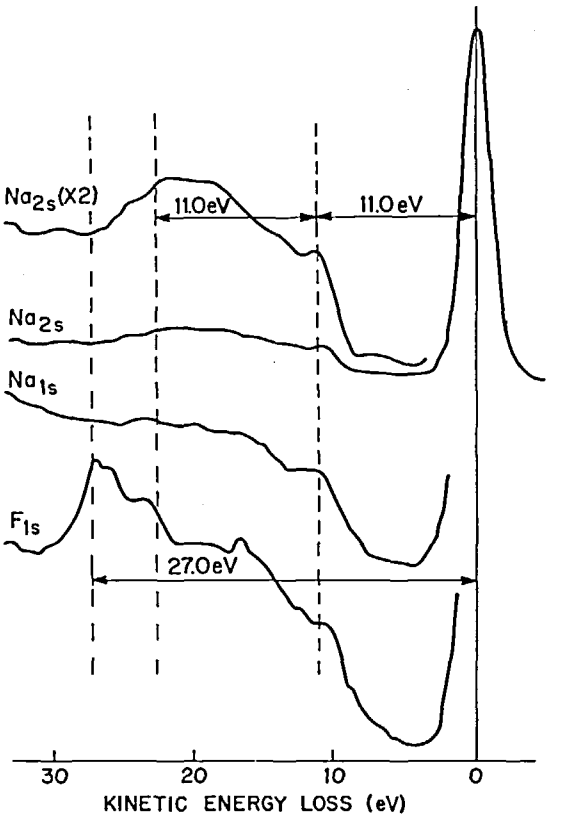

FIGURE 20. Energy loss spectral regions for Na_{2s}, Na_{1s}, and F_{1s} photoelectrons from NaF. [From Swingle, R. S., II, *Anal. Chem.*, 47(1), 21, (1975). With permission.]

relative intensity in the Na_{1s} spectrum of $NaBF_4$. The area of this satellite is ~25% of the area of the F_{1s} line, and its presence could account for the high Na_{1s}/F_{1s} ratio noted in Table 3 for $NaBF_4$.

Generally, in solids, the energy loss structure is not well-defined, and it is not realistic to try to include selected areas of the loss structure in a measurement of the photoelectron peak intensity. Each photoelectron can have a different total probability for extrinsic plus intrinsic energy loss, and this fact will be reflected in an increase or decrease of the photoelectron peak area. Any model for quantitative surface analysis using ESCA must take this fact into account and attempt to minimize its effect on quantitative accuracy.

3. Quantitative Theory

In the previous sections, we have discussed extrinsic and intrinsic energy loss processes for

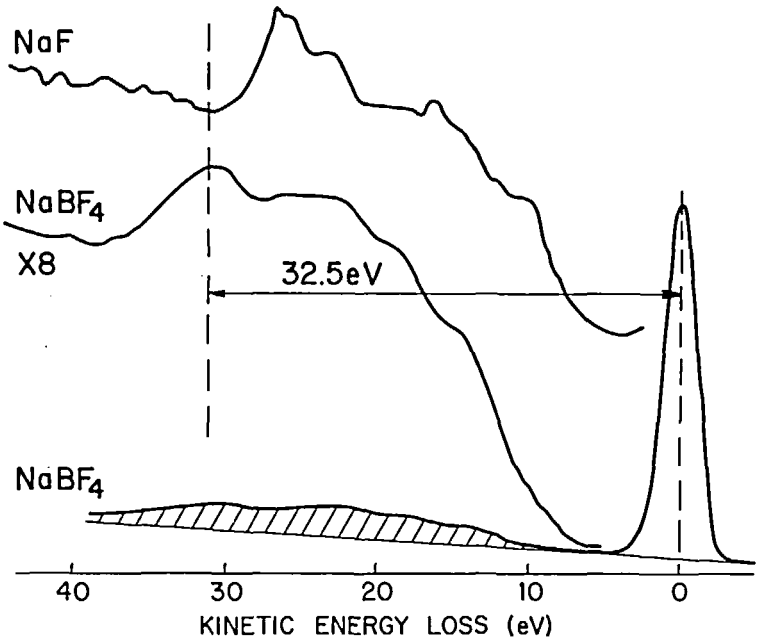

FIGURE 21. F_{1s} energy loss spectral regions for $NaBF_4$ and NaF. [From Swingle, R. S., II, *Anal. Chem.*, 47(1), 21 (1975). With permission.]

photoelectrons in solids and have demonstrated in a qualitative fashion how differences in these processes from sample to sample affect the accuracy of quantitative analysis. In this section, a method is presented which can be used to determine semiquantitative relative atomic concentrations at a sample surface. Because photoelectron intensities depend upon the inelastic mean free path of the photoelectron as well as the atomic concentration, it is convenient for purposes of discussion to divide solid samples into categories dependent upon the homogeneity of the sample in the surface (XY) plane and depth (Z) directions. Application of the quantitative theory to each class of compounds can then be discussed separately. The reader is cautioned to use the material presented in this subsection as a guide, only. Other, more detailed, quantitative models are possible,[73,74] and not all the conclusions presented here are universally accepted.

a. Class I Samples

Samples falling in this class are homogeneous in the XY plane as well as in the Z direction over a range greater than three to five times the inelastic mean free path of the highest kinetic energy photoelectron of interest. Consequently, the sample is fully homogeneous throughout an infinitely thick layer as far as the ESCA technique is concerned.

Several expressions have been developed which relate the photoelectron intensity from an infinitely thick sample to fundamental parameters. These expressions are more or less complex depending upon which variables (sample density, photon flux, source-sample-analyzer angular geometry, surface "shading" effects, instrument kinetic energy response function, etc.) are taken into account. For this discussion, the simplified expression first proposed by Wendt and Riggs[49,67] will be used.

For an infinitely thick sample, the intensity for photoelectron j, $I_j(\infty)$, can be written as:

$$I_j(\infty) = K_j \alpha_j N_j / S_j \qquad (14)$$

where α_j is the emissivity of the core shell of interest in atom j, N_j is the number of such atoms per cubic centimeter, K_j is the instrument response function dependent upon the kinetic energy of the photoelectron, and S_j is the total inelastic electron scattering coefficient in cm^{-1} for photoelectron j in the sample of interest. For many spectrometers, accurate instrument response functions are not known at present, and Equation 14 cannot be used in an absolute sense to relate photoelectron

intensities to N_j. However, in spectrometers which use a retarding field to sweep the ESCA spectrum, it has been shown empirically that, to a large extent, the kinetic energy dependences of the K_j and S_j terms in Equation 14 cancel one another, and that Equation 14 can be approximated by:

$$I_j(\infty) = A\alpha_j N_j \tag{15}$$

where A is constant for a given sample. (The magnitude of A will change from sample to sample since, as noted previously, the magnitude of S_j varies with the sample. However, the kinetic energy dependence of S_j can be approximated by a smoothly varying function of $1/E_K$ in the 200- to 1500-eV range.) Relative atomic concentrations for elements on the same surface can then be calculated from:

$$N_j/N_i = \frac{[I_j(\infty)]\,(\alpha_i)}{[I_i(\infty)]\,(\alpha_j)} \tag{16}$$

Note that if the kinetic energies of the i and j photoelectrons are nearly the same, it is not necessary to assume that the kinetic energy dependences of the K_j and S_j terms in Equation 14 cancel one another. In this case, Equation 16 follows directly from Equation 14 since $S_i = S_j$ and $K_i = K_j$. Consequently, if possible, it is generally advisable to use photoelectrons of about the same kinetic energies for the best quantitative results.

Atomic emissivities, α_j, which correlate directly with relative elemental sensitivities in the Varian IEE-15 spectrometer have been calculated by Wendt from known values of X-ray mass absorption coefficients. α_j can also be estimated from the more recent mass absorption coefficients tabulated by Heinke and Ebisu or from calculated photoelectric cross-sections. Table 4 lists Swingle's compilation[75] of the Mg k_α (1254-eV) photoelectric cross-sections *relative* to the C_{1s} level for each element in the periodic table. Values in this table were taken from J. H. Scofield's absolute cross-sections calculated using Hartree-Slater orbitals.[76,77] Al k_α (1487-eV) photoelectric cross-sections have also been calculated by Scofield and, relative to the C_{1s} level, the most sensitive level for each element agrees within ~10% with those values shown in Table 4 for Mg k_α radiation. The 1487-eV photoelectric cross-sections for different atomic levels within the same atom, however, can be substantially (>20%) larger for those orbitals with lower angular momenta compared to the values calculated for 1254-eV radiation. This effect has been confirmed experimentally by Wagner,[78] and Table 5 lists some measured relative intensities for different levels in the same atoms taken using both Mg k_α and Al k_α radiation.

The relative photoelectric cross-sections shown in Table 4 compare favorably with the experimentally determined atomic sensitivities published by Wagner for the Varian IEE-15 spectrometer.[70] Figure 22 plots atomic number versus Wagner's relative sensitivities using the 1s, $2p_{3/2}$, $3d_{5/2}$, and $4f_{7/2}$ levels where appropriate. (Note that Wagner's sensitivities are referenced to the F_{1s} level vs. the C_{1s} reference level in Table 4.) Because of the energy-loss problems discussed in the previous two subsections, it is difficult to accurately determine relative atomic sensitivities using solid standards. Until comprehensive measurements of photoelectric cross-sections have been made on gas phase systems, the calculated cross-sections are probably more accurate than relative sensitivities based on experimental measurement of photoelectron intensities from solids.

In summary, the simple treatment outlined above says that for spectrometers using a retarding field to sweep the kinetic energy spectrum, the area of a photoelectron line divided by its respective sensitivity factor (photoelectric cross-section) gives a "corrected intensity" which is related to the number of atoms of that element on the sample surface. Ratios of these corrected intensities for different elements detected on the same sample surface give a good estimate of the *relative atomic concentrations* at that surface, particularly if the photoelectron kinetic energies are similar. It is not possible at present to calculate absolute atomic concentrations (e.g., atoms/cm^2) at a surface from these corrected intensities unless critical assumptions are made concerning surface morphology, atomic density, and the magnitude of S_j in the solid of interest, or unless carefully selected standards with known surface compositions are available.

The experimentalist must exercise caution when using a material of known bulk stoichiometry as a "standard" for ESCA. One must know whether the surface of the standard is truly representative of the bulk stoichiometry, and this may not be easy to determine. Nearly all materials

TABLE 4

Photoelectric Cross Sections Relative to Cls Level for Mg Kα (1254eV) Radiation

		1s$_{1/2}$	2s$_{1/2}$	2p$_{1/2}$	2p$_{3/2}$	3s$_{1/2}$	3p$_{1/2}$	3p$_{3/2}$	3d$_{3/2}$	3d$_{5/2}$	4s$_{1/2}$	4p$_{1/2}$	4p$_{3/2}$	4d$_{3/2}$	4d$_{5/2}$	4f$_{5/2}$	4f$_{7/2}$	5s$_{1/2}$	5p$_{1/2}$	5p$_{3/2}$	5d$_{3/2}$	5d$_{5/2}$	5f$_{5/2}$	5f$_{7/2}$	6s$_{1/2}$	6p$_{1/2}$	6p$_{3/2}$
1	H	0.0002																									
2	He	0.0089																									
3	Li	0.059	0.0008																								
4	Be	0.200	0.007																								
5	B	0.492	0.022																								
6	C	1.00	0.047	0.0006	0.0012																						
7	N	1.78	0.084	0.0025	0.0049																						
8	O	2.85	0.134	0.0073	0.0145																						
9	F	4.26	0.199	0.0178	0.0352																						
10	Ne	5.95	0.277	0.0381	0.0751																						
11	Na	7.99	0.390	0.0714	0.141	0.0059																					
12	Mg		0.525	0.121	0.239	0.0261																					
13	Al		0.681	0.193	0.380	0.0485	0.0012	0.0023																			
14	Si		0.855	0.292	0.573	0.0726	0.0050	0.0097																			
15	P		1.05	0.422	0.828	0.0998	0.0129	0.0253																			
16	S		1.25	0.590	1.155	0.130	0.0269	0.0527																			
17	Cl		1.48	0.810	1.564	0.163	0.0493	0.0963																			
18	Ar		1.71	1.06	2.07	0.199	0.0503	0.161																			
19	K		1.96	1.37	2.67	0.249	0.122	0.238			0.006																
20	Ca		2.21	1.74	3.39	0.305	0.169	0.330			0.023																
21	Sc		2.46	2.18	4.24	0.356	0.216	0.420	0.002	0.003	0.027																
22	Ti		2.72	2.68	5.22	0.408	0.268	0.521	0.006	0.009	0.031																
23	V		2.98	3.26	6.33	0.462	0.326	0.633	0.014	0.021	0.034																
24	Cr		3.23	3.92	7.60	0.511	0.382	0.740	0.030	0.044	0.014																
25	Mn		3.48	4.63	8.99	0.575	0.460	0.892	0.048	0.071	0.040																
26	Fe		3.70	5.43	10.5	0.634	0.535	1.04	0.079	0.116	0.043																
27	Co		3.92	6.28	12.2	0.693	0.616	1.19	0.122	0.179	0.045																
28	Ni		4.16	7.18	13.9	0.753	0.701	1.36	0.181	0.265	0.048																
29	Cu		4.38	8.18	15.9	0.805	0.779	1.50	0.268	0.390	0.019																
30	Zn		4.55	9.29	18.0	0.873	0.882	1.70	0.365	0.532	0.052																
31	Ga			10.6	20.5	0.945	0.993	1.92	0.485	0.708	0.074	0.006	0.011														
32	Ge				21.2	1.02	1.11	2.15	0.631	0.920	0.094	0.018	0.034														
33	As					1.10	1.24	2.40	0.802	1.17	0.114	0.037	0.071														
34	Se					1.18	1.37	2.65	1.00	1.46	0.134	0.064	0.123														
35	Br					1.26	1.50	2.92	1.24	1.80	0.156	0.100	0.191														
36	Kr					1.35	1.64	3.20	1.50	2.19	0.178	0.144	0.276														
37	Rb					1.43	1.79	3.48	1.81	2.63	0.209	0.187	0.361					0.006									
38	Sr					1.52	1.93	3.78	2.15	3.14	0.242	0.230	0.445					0.021									
39	Y					1.61	2.08	4.09	2.54	3.70	0.273	0.268	0.521	0.013	0.019			0.025									
40	Zr					1.70	2.24	4.40	2.97	4.33	0.305	0.307	0.596	0.035	0.051			0.029									
41	Nb					1.79	2.39	4.71	3.45	5.01	0.333	0.340	0.661	0.082	0.118			0.013									
42	Mo					1.89	2.54	5.03	3.97	5.77	0.364	0.379	0.739	0.130	0.187			0.014									
43	Tc					1.98	2.69	5.36	4.54	6.60	0.397	0.419	0.818	0.192	0.276			0.015									
44	Ru					2.07	2.84	5.68	5.17	7.51	0.429	0.460	0.899	0.269	0.387			0.016									
45	Rh					2.15	2.98	6.00	5.84	8.48	0.463	0.501	0.981	0.365	0.524			0.016									
46	Pd					2.24	3.12	6.33	6.58	9.54	0.494	0.538	1.06	0.495	0.707												
47	Ag					2.33	3.25	6.64	7.36	10.7	0.531	0.586	1.15	0.616	0.884			0.018									
48	Cd					2.40	3.39	6.96	8.22	11.9	0.571	0.636	1.26	0.747	1.07			0.046									
49	In					2.48	3.51	7.27	9.13	13.2	0.611	0.689	1.37	0.893	1.29			0.063	0.006	0.011							
50	Sn					2.54	3.62	7.58	10.1	14.6	0.653	0.743	1.48	1.05	1.51			0.076	0.017	0.031							
51	Sb					2.60	3.71	7.86	11.1	16.1	0.696	0.799	1.60	1.22	1.76			0.090	0.033	0.063							
52	Te					2.67	3.79	8.14	12.2	17.7	0.741	0.856	1.73	1.40	2.01			0.104	0.054	0.104							
53	I					2.75	3.87	8.37	13.3	19.3	0.785	0.913	1.86	1.58	2.29			0.117	0.080	0.156							
54	Xe					2.83	3.95	8.64	14.5	21.1	0.831	0.971	1.99	1.78	2.57			0.132	0.112	0.218							
55	Cs					2.84	4.04	8.94	15.8	22.9	0.877	1.03	2.12	1.99	2.88			0.152	0.140	0.278					0.005		
56	Ba						4.10	9.26	17.0	24.8	0.924	1.09	2.26	2.21	3.20			0.174	0.166	0.334					0.017		
57	La						4.06	9.52	18.2	26.5	0.971	1.15	2.40	2.44	3.53			0.193	0.189	0.382	0.019	0.027			0.021		
58	Ce							9.67	19.7	28.6	1.00	1.18	2.49	2.58	3.74	0.069	0.088	0.189	0.180	0.365					0.018		
59	Pr							9.75	21.1	30.7	1.04	1.22	2.59	2.76	4.00	0.126	0.161	0.196	0.186	0.378					0.018		
60	Nd								22.6	32.9	1.07	1.26	2.70	2.95	4.28	0.200	0.257	0.202	0.191	0.390					0.018		
61	Pm								24.3	35.3	1.10	1.30	2.81	3.14	4.55	0.296	0.378	0.208	0.196	0.400					0.018		
62	Sm								26.1	37.9	1.14	1.34	2.91	3.33	4.82	0.416	0.531	0.213	0.201	0.412					0.019		
63	Eu								28.2	40.9	1.17	1.37	3.01	3.51	5.09	0.562	0.718	0.219	0.205	0.422					0.019		

TABLE 4 (continued)

Photoelectric Cross Sections Relative to Cls Level for Mg Kα (1254eV) Radiation

		$1s_{1/2}$	$2s_{1/2}$	$2p_{1/2}$	$2p_{3/2}$	$3s_{1/2}$	$3p_{1/2}$	$3p_{3/2}$	$3d_{3/2}$	$3d_{5/2}$	$4s_{1/2}$	$4p_{1/2}$	$4p_{3/2}$	$4d_{3/2}$	$4d_{5/2}$	$4f_{5/2}$	$4f_{7/2}$	$5s_{1/2}$	$5p_{1/2}$	$5p_{3/2}$	$5d_{3/2}$	$5d_{5/2}$	$5f_{5/2}$	$5f_{7/2}$	$6s_{1/2}$	$6p_{1/2}$	$6p_{3/2}$
64	Gd								24.3	43.4	1.20	1.41	3.13	3.73	5.41	0.693	0.887	0.235	0.223	0.465	0.022	0.031			0.022		
65	Tb									20.8	1.22	1.43	3.21	3.88	5.61	0.949	1.21	0.228	0.211	0.440					0.019		
66	Dy										1.25	1.45	3.30	4.05	5.87	1.20	1.52	0.232	0.214	0.449					0.019		
67	Ho										1.27	1.47	3.39	4.22	6.13	1.49	1.89	0.237	0.216	0.457					0.019		
68	Er										1.29	1.49	3.48	4.39	6.37	1.82	2.31	0.240	0.219	0.464					0.019		
69	Tm										1.31	1.50	3.56	4.56	6.62	2.20	2.78	0.244	0.220	0.471					0.019		
70	Yb										1.32	1.51	3.64	4.72	6.85	2.63	3.33	0.247	0.222	0.478					0.019		
71	Lu										1.34	1.52	3.73	4.91	7.13	3.05	3.87	0.261	0.237	0.519	0.021	0.029			0.023		
72	Hf										1.36	1.53	3.83	5.10	7.42	3.50	4.45	0.271	0.252	0.562	0.054	0.074			0.026		
73	Ta										1.38	1.54	3.93	5.29	7.15	3.99	5.08	0.290	0.268	0.606	0.098	0.136			0.029		
74	W										1.39	1.55	4.03	5.48	8.01	4.92	5.75	0.306	0.283	0.651	0.152	0.212			0.031		
75	Re										1.41	1.55	4.13	5.67	8.30	5.08	6.46	0.321	0.299	0.697	0.217	0.303			0.033		
76	Os										1.42	1.55	4.24	5.86	8.60	5.67	7.22	0.337	0.314	0.745	0.293	0.410			0.035		
77	Ir										1.43	1.55	4.34	6.05	8.90	6.30	8.03	0.350	0.324	0.774	0.431	0.593					
78	Pt										1.44	1.54	4.45	6.24	9.20	6.97	8.87	0.366	0.340	0.825	0.508	0.709			0.017		
79	Au										1.45	1.53	4.55	6.42	9.50	7.68	9.79	0.380	0.353	0.877	0.619	0.865			0.017		
80	Hg										1.45	1.52	4.65	6.60	9.79	8.43	10.8	0.397	0.368	0.935	0.707	0.997			0.040		
81	Tl										1.46	1.50	4.75	6.78	10.1	9.22	11.8	0.413	0.383	0.996	0.804	1.14			0.051	0.004	0.008
82	Pb										1.46	1.47	4.86	6.94	10.4	10.0	12.8	0.430	0.398	1.06	0.900	1.29			0.059	0.011	0.023
83	Bi										1.44	1.45	4.96	7.11	10.6	10.9	14.0	0.446	0.412	1.12	0.997	1.44			0.068	0.021	0.046

TABLE 5

Effect of Photon Energy on Measured Relative Intensities

Sample	Element	Orbitals	Intensity Ratios: Mg Kα (1254 eV)	Intensity Ratios: Al Kα (1487 eV)
MgF_2	Mg	2?/2s	0.83	0.70
4A Sieve	Al	2p/2s	1.04	0.82
	Si	2p/2s	1.59	1.23
GeO_2	Ge	$3d/3p_{3/2}$	1.29	1.08
$NaAsO_2$	As	$3d/3p_{3/2}$	1.19	1.15
Na_2SeO_3	Se	$3d/3p_{3/2}$	1.36	0.92
NaBr	Br	$3d/3p_{3/2}$	1.45	1.15

are subject to some degree to surface contamination by H_2O, CO, CO_2, or hydrocarbon. Most metal alloys exhibit preferential surface segregation of one element relative to another, and oxygen enrichment or deficiency at many metal oxide surfaces appears to be the rule rather than the exception.

Grazing angle ESCA.[79,80] described in Section IV, may be useful in determining whether the surface of a "standard" is representative of bulk stoichiometry. Ion sputtering can also be useful in generating surfaces of known stoichiometry, but this technique must be used with great care since preferential sputtering of one element relative to another is a well-documented phenomenon[81,82] and can lead to a surface which does not consist of the "standard" stoichiometry. For problems in which they are applicable, organic homopolymers are good standards because they are not generally subject to surface oxidation, adsorption, or segregation problems. For other problems, the only general guide is to use a standard as nearly like the sample of interest as possible. When possible, it is best to compare relative atomic concentrations among samples. If absolute concentrations are necessary, the pitfalls mentioned above must be considered.

Note that the quantitative model presented here does not deal with the effects of intrinsic processes on photoelectron peak intensities. As discussed previously, it is not possible to do this for most analytical samples, and peaks exhibiting obvious intrinsic satellites should not be used for quantitative analysis if alternative peaks are available. When comparing intensity ratios from a closely related series of samples, intrinsic processes will not usually present a problem but, to be sure, the corrected intensities of more than one photoelectron peak from each of the elements of interest can be measured and compared.

b. Class 2 Samples

Samples falling in this class are layered samples that are homogeneous in the XY plane but not homogeneous over the sampling depth of the ESCA technique. If the element of interest is in the top layer and the layer has a thickness X, then the intensity of photoelectron j from that element is given by:

$$I_j(X) = I_j(\infty)\,[1 - e^{-S_j X}] \qquad (17)$$

where $I_j(\infty)$ is the intensity that would be observed if the layer were infinitely thick. For two photoelectrons arising from elements in the top layer, the relative concentrations are given from Equations 14 and 17 as:

$$N_j/N_i = \left(\frac{I_j(X)}{I_i(X)}\right)\left(\frac{\alpha_i}{\alpha_j}\right)\left(\frac{1 - e^{-XS_i}}{1 - e^{-XS_j}}\right) \qquad (18)$$

Note that this expression has a ratio of exponential terms involving both the layer thickness and the inelastic scattering coefficients of the two photoelectrons. The relative atomic concentrations cannot be calculated directly from Equation 18 unless the kinetic energies of the two photoelectrons are nearly the same (in which case it can be assumed that $S_i = S_j$ and Equation 18 reduces to

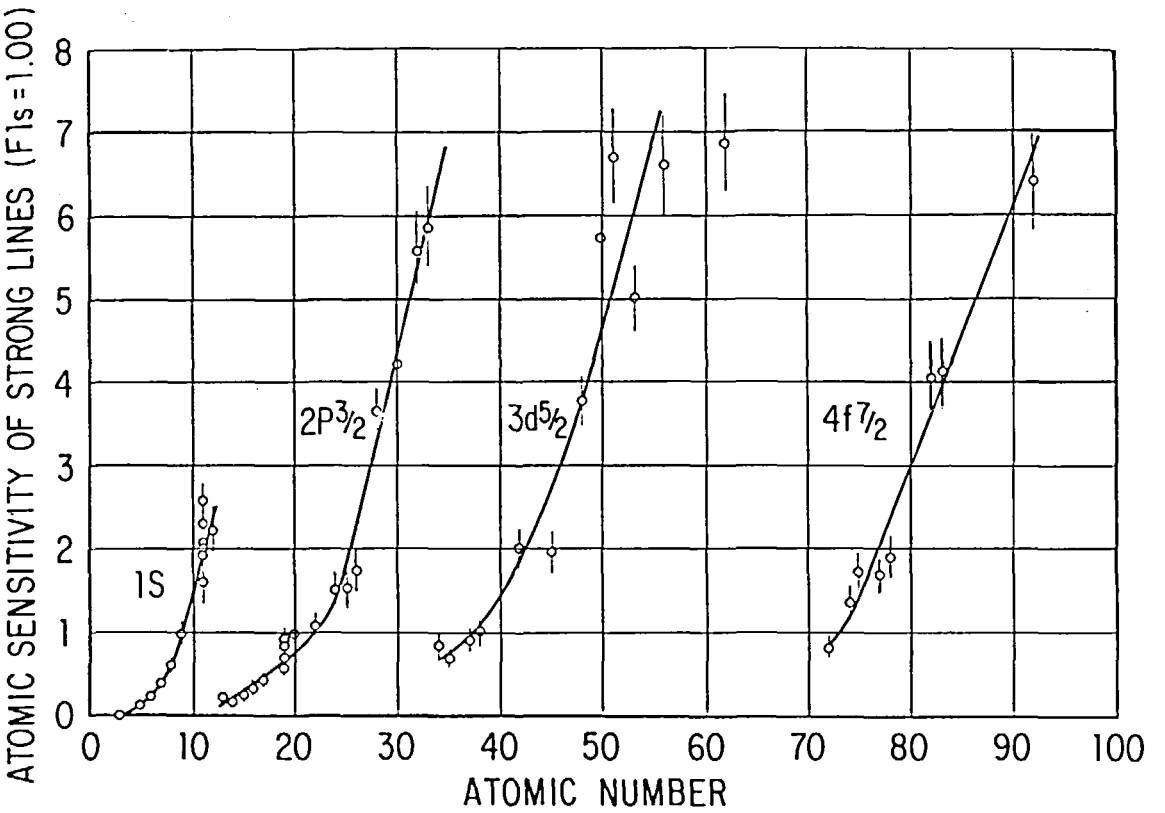

FIGURE 22. Experimental atomic sensitivities relative to F_{1s} level determined on Varian IEE-15 spectrometer. [From Wagner, C. D., *Anal. Chem.*, 44(6), 1050 (1972). With permission.]

Equation 16) or unless the layer thickness is known and absolute values of S_i and S_j in the layer are known or can be estimated (Equation 18 cannot be solved knowing only the relative magnitudes of S_j and S_i). If neither of these conditions can be met, then intensity ratios can be used among similar samples with the same layer thicknesses as a measure of relative concentrations in the surface layers of the samples. However, each corrected intensity ratio will not represent the relative atomic concentration of the two elements at that surface. If the layer thickness cannot be assumed constant from sample to sample, then corrected intensity ratios are not even useful for relative comparison among samples. In these cases, it may be helpful to use grazing angle ESCA in order to reduce the sampling depth of the technique to less than the layer thickness. This effectively changes a Class 2 into a Class 1 sample.

The photoelectron intensity from an element in a substrate layer covered by a layer of thickness Y is given by:

$$I_j(Y) = I_j(0)\,[e^{-S_j^* Y}] \qquad (19)$$

where I_j (0) is the intensity that would be observed if the covering layer were of zero thickness, and S_j^* is the inelastic scattering coefficient of the photoelectron in the covering layer matrix. The same considerations are important in determining relative atomic concentrations for elements in the substrate layer that are mentioned above for the top layer and, consequently, this case will not be treated further. It should be mentioned that, subject to the limitations discussed earlier, ion sputtering may be useful in this case to remove the covering layer, thus changing the substrate into a Class 1 sample.

Comparing photoelectron intensities from elements localized in different layers becomes an

even more complex problem. The special case of an ultrathin surface layer (less than one monolayer) on an infinitely thick substrate is of interest, however, since many samples of practical interest can be treated using this model. Supported metal catalysts with single metal atoms or small metal atom clusters on a substrate and partly exchanged ion exchange resins are two examples of this type of sample. If the substrate is only slightly covered by the surface atoms (1 to 5% coverage), it can be assumed that the intensity of the photoelectrons from atoms in the surface layer is not attenuated at all by inelastic scattering and that the intensity of the photoelectrons from the substrate is not attenuated by the surface layer. Thus, the substrate intenstiy can be used as an internal standard, and the intensity ratio of the surface atom peak divided by the substrate peak will be directly related to the number of surface atoms on a given sample. Although these intensity ratios are not easily converted to either absolute or relative atomic concentrations at the surface of a single sample, they are useful in direct comparison with intensity ratios from other similar samples as a measure of the relative amounts of the surface-localized element.

C. Class 3 Samples

Samples in this class are not homogeneous in either the XY plane or the Z direction. While the sampling depth depends on the inelastic mean free path of the photoelectron in the solid, there is no X-Y resolution in the ESCA technique, and the spectrum consists of an integral signal from all irradiated portions of the sample surface. In general, only qualitative analysis is possible with Class 3 samples. In certain situations, special sample preparation techniques such as masking portions of the sample surface can be useful. Otherwise, surface analysis techniques with better XY resolution should be used for quantiative analysis.

III. CURRENT ESCA INSTRUMENTATION

Although commercial ESCA instrumentation has only been available for a relatively short time (since about 1970), at least eight different commercial instruments have been available during that period, and they have been characterized by great diversity of design. As with any complex instrumentation, the design of a commercial electron spectrometer involves a number of trade-offs. We will discuss the important considerations in making these trade-offs in ESCA instrumentation. For convenience, this discussion will be organized by instrument component and function, including discussions of vacuum system design, X-ray source design, analyzer design, detectors, modes of scanning, sample considerations, and various means of data output.

A. Vacuum System

1. Required Vacuum Level

There are two basic requirements imposed upon the design of vacuum systems for ESCA measurements. The first is that the analyzer vacuum be sufficient for the mean free path of an electron in the vacuum environment to be long compared to the distance it must travel between sample and detector. This requires vacuum levels on the order of 10^{-6} torr. Most commercial instruments also operate the X-ray source directly in the analyzer vacuum. The vacuum level required for X-ray source operation is similar to that dictated by electron mean free path considerations. The second and more rigorous vacuum requirement is that the vacuum level be sufficient that the sample surface is not altered significantly by the vacuum atmosphere during the measurement. One can show by simple calculation that at a vacuum level of 1×10^{-6} torr, approximately 1 monolayer of molecules per second will accumulate on a surface if the sticking coefficient of the gas molecules is unity on that surface. If sticking coefficients near unity were common, this would mean that vacuum in the 10^{-10}-torr range would be required to maintain a surface in clean condition for a measurement requiring on the order of 1 hr. However, as Tracy[83] has recently pointed out, it is rare for the sticking coefficient of gases on surfaces to be near unity. In fact, for most gases on most materials, the sticking coefficient is less than 10^{-3}, which means that a 10^{-7}-torr vacuum is adequate for most ESCA measurements. Furthermore, the sticking coefficient usually drops drastically after one monolayer of material is adsorbed on the surface; the sticking coefficient of a gaseous molecule on a layer of similar molecules is normally far smaller than the sticking coefficient of the molecule on the bare surface of a material such as a metal. Since the vast majority of samples which one wishes to examine for analytical pur-

poses have been handled in a laboratory atmosphere, their surfaces are already saturated with adsorbed gas when one introduces them into the spectrometer. The likelihood of further gas adsorption as a result of vacuum atmosphere is small. Vacuum requirements are more rigorous for Auger measurements due to phenomena such as electron beam induced adsorption. This has occasionally led, through inappropriate analogy, to the erroneous conclusion that vacuum requirements for ESCA are more stringent than they actually are.

For operation at the relatively moderate vacuum levels that are adequate for ESCA, on the order of 10^{-6} to 10^{-9} torr, the absolute vacuum level is less important than the composition of the vacuum atmosphere. Materials with generally high sticking coefficients or those which, if adsorbed on a sample would interfere with data interpretation (such as hydrocarbons and water) are to be avoided if possible; on the other hand, relatively inert gases such as argon, neon, and nitrogen can be tolerated at relatively high levels during ESCA measurement.

2. Design

The details of the design of the vacuum system for ESCA hardware will depend upon considerations of cost, utility, and intended application of the equipment. The major areas of consideration are discussed below.

Some instruments have sample introduction chambers, and others do not. There are two major advantages to using a vacuum interlock sample introduction system. The first is that the analyzer high vacuum can be maintained at all times and need not be broken for sample interchange. It is possible in some instruments of this design to change samples in as little as 2 to 3 min without significant degradation of the analyzer vacuum. This capability is particularly advantageous in an analytical or other laboratory where sample throughput is an important consideration. Instruments with sample introduction chambers tend to have significantly higher throughput than those which do not, even if only one sample is introduced at a time. A second advantage of the introduction chamber is that with proper design, it can also be used as a reaction or sample preparation chamber. In this chamber, one can conduct experiments such as ion etching the sample, vacuum evaporating metals onto the sample either for calibration purposes or for study of the metals themselves, and conducting gas-solid reactions which may be of interest in corrosion and heterogeneous catalysis.

The major disadvantage of the sample introduction chamber is that it typically necessitates the use of some sort of sliding vacuum seal. It is relatively difficult to maintain true ultrahigh vacuum conditions when a sliding seal is used to introduce samples, although commercial instruments are available with introduction chambers and sliding seals which operate routinely in the 10^{-9}-torr range. The sample is also exposed to contamination as it slides through the seal chambers during sample introduction. Since the sliding action wipes the probe, this can become a dirty area. Further, traces of water will be carried into the analyzer vacuum probe rod unless a dry box is used around the introduction chamber area.

When rigorous ultrahigh vacuum conditions are desired, sample introduction chambers are normally not used. In these cases, the sample chamber is designed so that a number of samples can be introduced at once, since the pump-down times may be on the order of 12 hr or more, and multiple samples are therefore a requirement in order that sample throughput not suffer to an intolerable extent.

The choice of vacuum pumps for an ESCA vacuum system is one which has been made in a number of different ways by commercial manufacturers. A popular combination of "dry" pumps is a molecular sieve sorption pump for rough pumping in combination with a differential ion pump for producing high vacuum. Advantages of this system include the total absence of pumping fluids, which avoids the possibility of contamination of the sample or vacuum system by these fluids. The pumps are reliable and based on well-known technology. A characteristic of ion pumps is that not all gases are pumped with equal speed. Fortunately, however, the gases which are not pumped well by ion pumps, such as argon, are almost totally innocuous in the ESCA experiment. Therefore, ion pumps are generally a good choice. A second combination which is of value is the use of a cryosorption pump for rough pumping, with both ion pumping and sublimation pumping in the high vacuum section. An ion pump and sublimation pump in close proximity to one another produce synergistic pumping effects since the ion pump pumps material which the sorption pump or sublimation pump does not pump well, and vice

versa. Again, this is a totally dry pumping system capable of producing ultrahigh vacuum. A further advantage of systems utilizing ion pumps is that power failures or pump shutdowns rarely damage ion pumps and the ion current readout serves as a pressure gauge. A third possibility is that of a turbomolecular pump backed by a large mechanical pump. Advantages of this kind of pump are that all gases are pumped with essentially equal efficiency and high gas loads can be tolerated. If the turbomolecular pump is sufficiently large in size, it can also produce ultrahigh vacuum conditions. Disadvantages of this kind of pumping system are that fluid is present in the mechanical pump and lubricating fluids are necessary for the bearings of the pump turbine. In the event of a vacuum accident, the vacuum system can become contaminated with organic fluids from these sources. A further disadvantage is that turbomolecular pumps are relatively expensive. A fourth possibility is the combination of a diffusion pump backed by a mechanical roughing pump. The advantages of this kind of system are that it is based on familiar and thoroughly developed technology and is relatively inexpensive and rugged. The disadvantages, however, lie in the presence of organic pumping fluids in both the diffusion pump and the mechanical pump, necessitating the use of very efficient cryogenic trapping to prevent oil vapors from entering the analyzer and contaminating the sample. In the event of a vacuum accident, the analyzer and sample areas can quite easily become contaminated with organic pumping fluids.

The incorporation of bakeout facilities and the ultimate temperature of bakeout available are other variables in vacuum system design for ESCA. If ultrahigh vacuum is desired, bakeout capability to a temperature of 250°C is typically required. In a system of this kind, bakeout heaters will typically be permanently installed, and flanges and all other materials of construction will be designed to easily withstand the rigors of 250°C at ultrahigh vacuum. A more moderate bakeout in the temperature range of 125 to 150°C is also useful for producing favorable vacuum conditions, especially for reducing the background of water desorbing from the vacuum system walls.

Metal flanges using copper gaskets as sealing materials are normally used in UHV systems. The advantage of this kind of flange design is that it can be baked to 250°C or more without degrading its performance as a vacuum seal. The disadvantages are that it is relatively expensive and that it is more difficult to work with than alternatives. The major alternative in use in ESCA vacuum flange design is the use of flanges incorporating Viton® fluoroelastomer seals. These seals can readily withstand moderate bakeout conditions and are relatively inexpensive to fabricate and easy to assemble free of leaks. The possibility that the elastomer material will desorb undesirable hydrocarbon material in the vacuum system, however, frequently discourages the use of this type of seal in ultrahigh vacuum systems. With appropriate flange design, however, Viton® can be used effectively in UHV systems. Other gasket materials which are sometimes used include tin and gold. The advantage of these soft metals is that gaskets can be formed to provide bakeable seals on flanges of relatively inexpensive design.

B. X-ray Source Design

1. Generation of X-rays

Generation of X-rays for an ESCA experiment is accomplished by imposing a potential of 10 to 12 kV between a hot filament emitting electrons and the X-ray anode. Electrons are accelerated to the anode material, and the ensuing collisions create inner level vacancies in the atoms of the target material. Subsequent relaxation then produces the characteristic X-rays of the anode material which are used in the ESCA experiment. Bremstrahlung,[84] a background of continuous radiation extending to the maximum energy of the excited electrons, is also generated as the high energy electrons decelerate rapidly in the target material. This is illustrated in Figure 23 for both aluminum and magnesium anodes.

2. Target Materials

For purposes of ESCA measurements, aluminum and magnesium are the most useful target materials. Aluminum Kα radiation has an energy of 1486.6 eV and an energy distribution (full width at half maximum of the overlapped $K\alpha_{1,2}$ doublet) of approximately 0.9 eV. The magnesium Kα line has an energy of 1253.6 eV and an energy width of approximately 0.7 eV. Thus, a somewhat narrower electron kinetic energy distribution and a correspondingly higher ESCA resolution are obtained with a magnesium anode. The slightly lower magnesium X-ray photon energy means that certain otherwise useful ESCA lines, especially

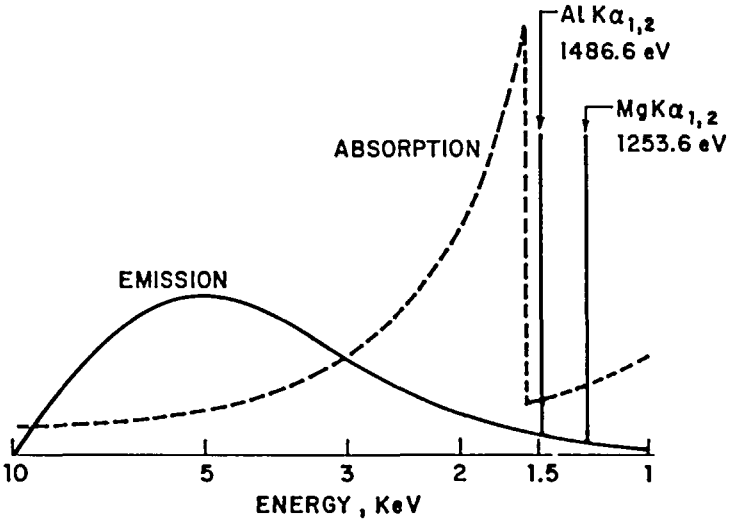

FIGURE 23. Mass absorption coefficient of aluminum as a function of energy (- - -), and intensity distribution of magnesium or aluminum anode X-ray tubes operated at 10kV (——).

magnesium 1s, are not accessible with this anode, and anode cooling is somewhat more critical. Nevertheless, magnesium is normally the anode of choice for ESCA experiments because of the higher resolution available. Aluminum is used occasionally when it is necessary to observe the magnesium 1s line or to avoid interferences from X-ray generated Auger electrons.

3. X-ray Window/Filter

A thin window is normally interposed between the X-ray source and the sample in an ESCA experiment, primarily to prevent electrons from the X-ray source from entering the kinetic energy analyzer and contributing to the spectral background. For this purpose, thin metal foils, normally aluminum or beryllium, are used. If aluminum is used as the X-ray window, it serves the secondary function of a wavelength filter to improve the signal-to-background ratio observed in the spectra, since the aluminum X-ray absorption spectrum exhibits a K adsorption edge at an energy just above that of the aluminum K emission line. Figure 23 illustrates this effect with the aluminum absorption spectrum in the 1 to 10 KV energy range shown superimposed upon the emission spectrum. Inspection of this figure shows that X-rays of energy significantly higher than the Kα emission are very strongly absorbed, whereas the Kα emission line itself is only weakly adsorbed. Even though the effect is not quite so dramatic, the same filtering of magnesium radiation by the aluminum window material occurs.

4. Line Width Considerations

Minimizing the width of the exciting X-ray line is desirable since the width of this line appears directly in the width of the observed photoelectron peak; the wider the X-ray line, the more resolution suffers. As previously stated, narrow lines are normally obtained through the selection of magnesium as the source of X-rays for ESCA. However, there is commercial instrumentation available wherein crystal dispersion techniques are used to disperse and partially monochromatize the X-rays which fall on the sample. The best known of these schemes[85] utilizes a technique known as dispersion compensation wherein the X-ray line is dispersed across the sample as a function of energy and the photoemitted electrons are spatially correlated with the point from which they originate on the sample. This dispersion compensation scheme allows the observation of electrons of a range of energy focused as if they were all of the same energy. The advantage of this approach over direct monochromatization using narrow slits is the conservation of the small amount of X-ray energy which is available, producing higher signal strengths than would otherwise be achieved. The use of X-ray source monochromatization allows the observation of ESCA lines approximately 0.4 eV (20 to 40%) narrower than those achievable on

instruments not utilizing X-ray monochromatization. Another important feature of monochromatized systems is the very low background achieved due to elimination of the bremstrahlung portion of the X-ray spectrum. This is especially significant in the valence band region.

C. Analyzer Design

Numerous schemes have been utilized for measurement of electron kinetic energy distributions. Included here will be only those designs which are presently being utilized in commercial instrumentation or which are significant for historical reasons. More thorough and detailed reviews are available in the literature.[86]

1. Magnetic Deflection

The earliest electron spectrometers for ESCA utilized a magnetic field to sort electrons from one another on the basis of kinetic energy.[1] The magnetic field was scanned by varying the current to coils which produced the field. This type of spectrometer never achieved commercial use, primarily because of its extreme sensitivity to ambient magnetic fields and the need for cancellation of these fields at the spectrometer through the use of surrounding Helmholtz coils. They were also very insensitive and difficult to operate. In spite of their disadvantages, much pioneering ESCA research was carried out with magnetic instruments, and several are still in operation.

2. Spherical Capacitor

The spherical capacitor analyzer[86] consists of sections of two concentric spheres of different radii. This type of analyzer functions in a manner analogous to a prism and lens system. Electrons having different energies are separated from one another as they traverse the electric field established between the two spherical sectors. Electrons having the same energy and diverging from each other as they enter the analyzer will be brought to a focus at the exit slit. Because of this characteristic, the spherical sector is space focusing: that is, a point source is imaged as a point. Because this analyzer has a well-defined focal plane, it can be utilized with multi-element detectors, which are discussed later.

3. Cylindrical Mirror

The cylindrical mirror or cylindrical capacitor analyzer is another type currently in use in commercial instrumentation.[87] This analyzer consists of two coaxial cylinders, with the outer cylinder at a potential which is negative relative to the inner cylinder. The sample and detector are located at opposite ends of the cylinders along the common axis. An optical baffle is located inside the inner cylinder to prevent electrons from moving in a straight line from the sample to the detector. The potential difference between the inner and outer cylinders creates a cylindrical electrostatic field. Entrance and exit slots are cut around the circumference of the inner cylinder, with the planes of these slots parallel to each other and normal to the coaxis of the cylinders. The axial symmetry of this analyzer produces space focusing. In contrast to the spherical capacitor analyzer, no focal plane exists with this device. The intrinsic resolution capability of this type of analyzer is apparently not especially high. The commercial adaptation of the analyzer utilizes tandem cylindrical capacitors to improve resolution by causing electrons to traverse two analyzing fields before being detected.

4. Nondispersive Electrostatic Filter

The third type of analyzer currently available commercially utilizes two spherically symmetric retarding fields.[88] A simplified diagram of this analyzer is shown in Figure 24. The first retarding field encountered by the photoelectrons is used in the reflection mode and functions as a low energy pass filter. The second field is used in the transmission mode as a high pass filter. The first filter rejects high energy electrons by scattering from the solid plate which is the second field defining element of this filter; the second filter rejects low energy electrons by simple reflection. There is a small energy overlap between these two filters which yields a narrow transmission function as illustrated. The resolution of this analyzer is dependent only upon the energy overlap of the two filters and the sharpness of their cutoff characteristics and not on acceptance angle or aperture size. Thus, it has the advantage of simultaneous achievement of high resolution and high sensitivity. This analyzer is not space focusing, nor does it have a focal plane.

D. Detectors

1. Single Element Detectors

Most electron spectrometers which are currently available commercially utilize single element

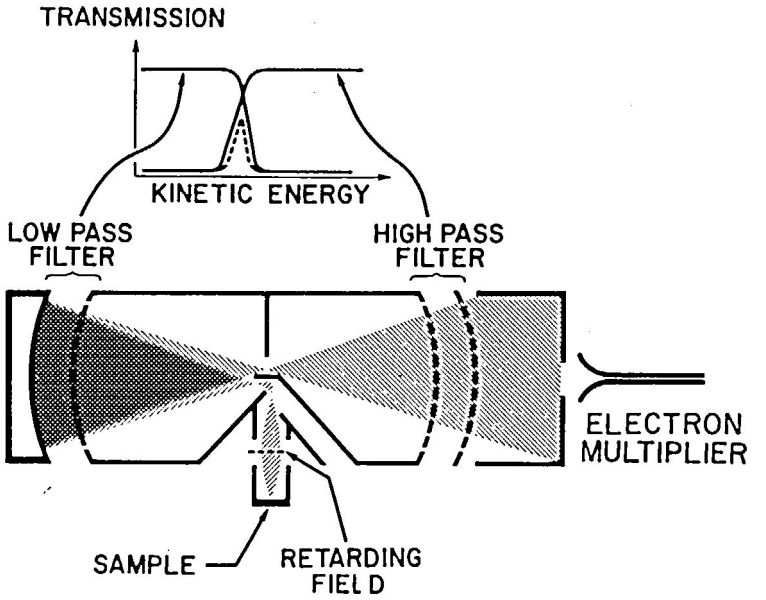

FIGURE 24. Simplified schematic diagram of a nondispersive electron kinetic energy analyzer. (Courtesy of Du Pont Instrument Products Division.)

detectors positioned at the exit aperture. By far the more common type of detector in use is the continuous dynode type. Their advantages are relatively high gain, the ability to operate in either a pulse counting or a current mode, and the ability to withstand repeated exposure to air when the instrument is vented without degrading performance. The more conventional multiple stage copper/beryllium type electron multiplier is also usable in ESCA applications, but is much less common.

2. Multi-element Detectors

Electron spectrometers utilizing analyzers which have a focal plane can, in principle, make use of multi-element detectors. These detectors consist of an array of linear multiplier surfaces arranged side-by-side. This array can be placed on the focal plane of the spectrometer, and electrons of a range of energies may be collected across it. By simultaneously examining a large number of resolution elements, multi-element detectors currently in use can produce in excess of 100 X improvement in signal-to-noise ratio per unit data acquisition time.[89] In the most widely used configuration, a phosphor screen is placed directly behind the array. When an electron strikes a particular element of the array, it creates an electron pulse at the phosphor screen, in turn generating a pulse of light. A vidicon camera scans the phosphor screen and detects and transmits the light pulses to the pulse counting equipment of the spectrometer.[85] Since currently it is not technologically feasible to fabricate multi-element detectors such that the gain and noise of all elements is identical, an incident electron will produce a different light pulse intensity on different detector elements, thus distorting the spectral information. In order to circumvent this problem, the spectrum is normally scanned back and forth across the detector array so that each spectral element will be detected for an equal period of time by each detector element, thus averaging out differences in gain and noise from element to element in the detector. The result is true Poisoin statistics, which give an improvement in signal-to-noise ratio proportional to the square root of the number of scans. The advantage of these detectors is the dramatic improvement in the amount of time required to take data. An additional potentially useful characteristic of this arrangement is that some spatial resolution (ca 1 mm^2) can be obtained by means of electronic slits. The disadvantages include the requirement for a focal plane spectrometer, the cost, and the relatively complicated ancillary equipment such as the phosphor screen, the vidicon camera, and data handling equipment. At the present time, multi-

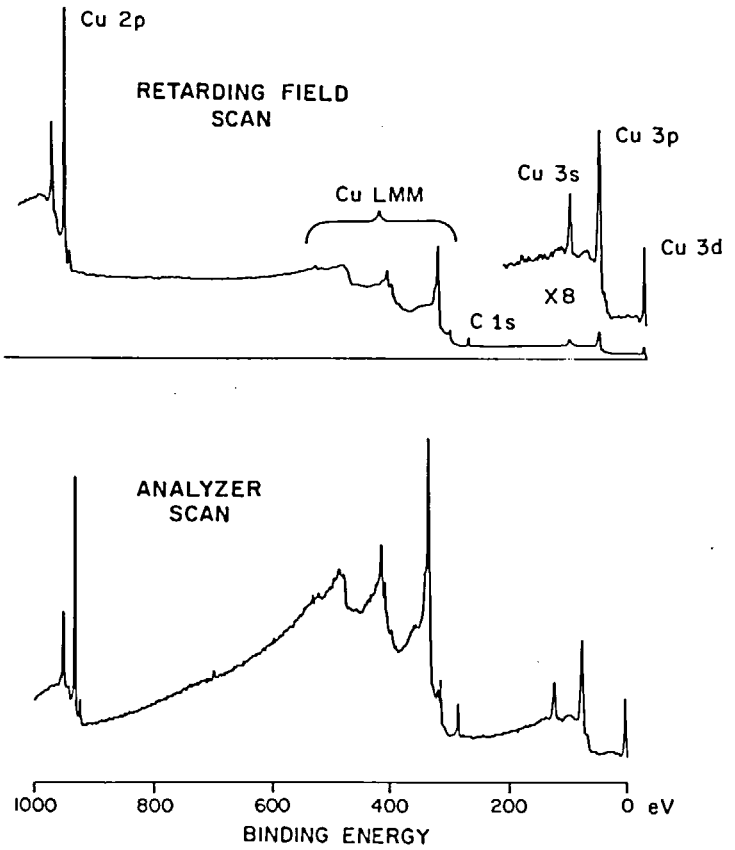

FIGURE 25. Survey spectra of copper metal comparing spectral background and peak intensity ratios from retarding field scanning (top) and an analyzer scaning modes (bottom).

element detectors are used only in instruments utilizing X-ray monochrometers because of the low signals achieved from such instruments and the corresponding need to enhance them by every means available.

E. Scanning Mode

There are two fundamental ways in which an ESCA spectrum may be scanned. The first is to scan the electron kinetic energy analyzer so that the electron energy which will pass through it to the detector is continuously varied. In the case of the spherical capacitor or the cylindrical mirror analyzer, this is done by varying the electrostatic field between the spherical or cylindrical electrostatic elements of the analyzer. In the case of the nondispersive analyzer, the energy of the filter functions would be continuously varied. There is one commercial spectrometer currently available which scans exclusively in this mode, and another is available which can scan in either mode. The second approach to scanning the spectrometer is to establish a retarding field between the sample and the analyzer and to scan this field while maintaining the acceptance energy of the analyzer at a fixed value. Thus, the spectrum is effectively scanned past the energy window established by the analyzer. Most commercial electron spectrometers utilize this scanning mode, primarily because retardation generally produces better spectral intensity.[90] Figure 25 shows 2 spectra obtained from copper metal, one on a Du Pont 650 Electron Spectrometer scanned in the retarding field mode, and the second on a McPherson electron spectrometer which utilizes the analyzer scanning technique. Visual comparison of these spectra reveals two primary differences. First, the background tends to drop at high binding energy when utilizing the analyzer scanning mode and to stay constant or increase with the retarding field mode. The second difference is in the relative peak intensities. Note that the major copper Auger line

appears to be more intense in the analyzer scanning mode than does the copper $2p_{3/2}$ photoelectron line. This is anomalous, for the number of emitted LMM Auger electrons cannot exceed the number of emitted Cu 2p electrons since the Auger transition begins with a 2p vacancy. In the retarding field scan mode, the Cu $2p_{3/2}$ line is approximately 3 times as intense as the Auger line, which is qualitatively in agreement with expectation. This reflects the basic difference between the two scanning modes; the analyzer scanning mode tends to distort the spectrum in favor of electrons at high kinetic energy, whereas the retarding field mode does not. This is due to the fact that with retardation, the spectrometer sensitivity variation with kinetic energy tends to cancel the effect of changing electron escape depth with kinetic energy. The discussion in Section II.C clarifies this further. From an analytical point of view, it appears on empirical grounds that the retarding field mode is more convenient because of the agreement of peak intensity ratios observed between spectra obtained in this mode and the relative sensitivities derived from the calculated photoelectric cross-sections (Table 4). Semiquantitative estimation of sample composition is therefore more straightforward using spectrometers scanned by retardation.

F. Sample Considerations

Some of the most important instrumental design considerations are centered on the size, shape, and other characteristics of the sample, as well as the facilities for preparing, manipulating, and pretreating the sample. Some of these are discussed briefly below.

The sample phase is obviously a primary consideration. Spectrometers are available which can accept both solid and gas phase samples. To date, gas phase X-ray photoelectron spectroscopy research has revealed little direct analytical application. Therefore, at the present time, the ability to handle solid samples is the only important consideration for spectrometers intended for analytical measurements.

Spectrometers vary in their ability to accept samples of different sizes and shapes since this is a design compromise involving other factors. With any present available sample configuration, one must occasionally use his ingenuity to get his sample into the instrument. In most spectrometers, a sample with a rough surface will give a lower signal intensity than a sample of the same composition with a smooth surface. In spectrometers using X-ray monochromators and dispersion compensation, resolution also degrades with sample roughness. In these instruments, the depth of field of the entrance lens is very small and the sample must be positioned within a few thousandths of an inch to optimize resolution and sensitivity.

Some spectrometers maintain the sample in a horizontal configuration at all times, while others either do not mount the sample horizontally or require that it be rotated through a nonhorizontal configuration for insertion into the spectrometer. Obviously, if a horizontal configuration is maintained throughout, this is an advantage for operating with powdered samples which then need not be held in place with an adhesive or other special arrangement.

If liquids or other volatile materials are to be examined, the ability to lower the sample temperature in order to reduce the vapor pressure sufficiently so that it may be examined in the vacuum environment may be required. Conversely, the ability to increase sample temperature above ambient can be important if phase transitions are to be studied or gas-solid reactions at the sample surface are to be conducted.

The availability of a sample reaction chamber is an important instrumental consideration. Conducting gas-solid reactions is best done in a special chamber in order to avoid exposure of the spectrometer to corrosive or otherwise damaging environments. Other kinds of sample pretreatment such as ion etching, scraping, vapor deposition of metals, and fracturing to expose fresh surface are also best done in a chamber connected to, but isolated from, the analyzer chamber.

The ability to ion etch samples is a further useful capability. Ideally, the angle between the sample and the ion beam will be between 25 and 40° in order to maximize the etching rate.[91,92] The ion beam energy should be relatively low – normally below about 2000 eV in order to minimize the amount of damage done to the surface by the ion beam.

The ability to do angular dependence measurements in the spectrometer can be important both for quantitative work (see Section II.C) and in order to obtain in-depth information nondestructively (Section IV.C).

It is sometimes important to be able to transfer samples into the spectrometer while maintaining

them under an inert atmosphere. Although no commercial spectrometers have attachments available for this procedure, some are more easily adaptable to transfer of samples under inert atmosphere than are others.

G. Data Acquisition and Processing

In current ESCA instrumentation, the data obtained are inherently digital, with electron counting being the normal detection mode. Thus, digital data accumulation systems, such as multichannel analyzers and computers operating in multichannel data acquisition modes, are common. At least two commercially available ESCA instruments also have analog data collection modes. When the signal is sufficiently strong, it is convenient to convert the digital signal to analog with an appropriate ratemeter. The ratemeter output is then used to drive an XY recorder, thereby allowing the data to be plotted in real time. When applicable, analog data acquisition is more convenient and often faster than corresponding digital data acquisition and is a useful option to have available. By appropriate choice of scanning speeds and ratemeter time constant, the signal/noise ratios which are achievable with analog scanning are equivalent to those obtainable with equal data acquisition time in a digital scanning mode.

Digital data acquisition and the corresponding ability to signal average repetitive scans over a spectral region are an important capability in ESCA because of the widespread occurrence of relatively weak signals. These signals may be enhanced by long-term signal averaging in order to extract weak signals from background noise. Multichannel analyzers, commercially available from several manufacturers, are the simplest and least expensive means of obtaining this capability. Most multichannel analyzers which are currently available are sufficiently flexible for data acquisition over narrow spectral regions for obtaining high resolution data as well as for obtaining survey scan data over wide spectral regions. Furthermore, these instruments usually have useful data manipulating capabilities. For example, digital smoothing of data, background slope correction, and subtraction of background, as well as differentiation and integration of data, are all possible with most commercial multichannel analyzers. Figure 26 shows the application of the multichannel analyzer capability to background correction of the steeply sloped background from a copper spectrum.

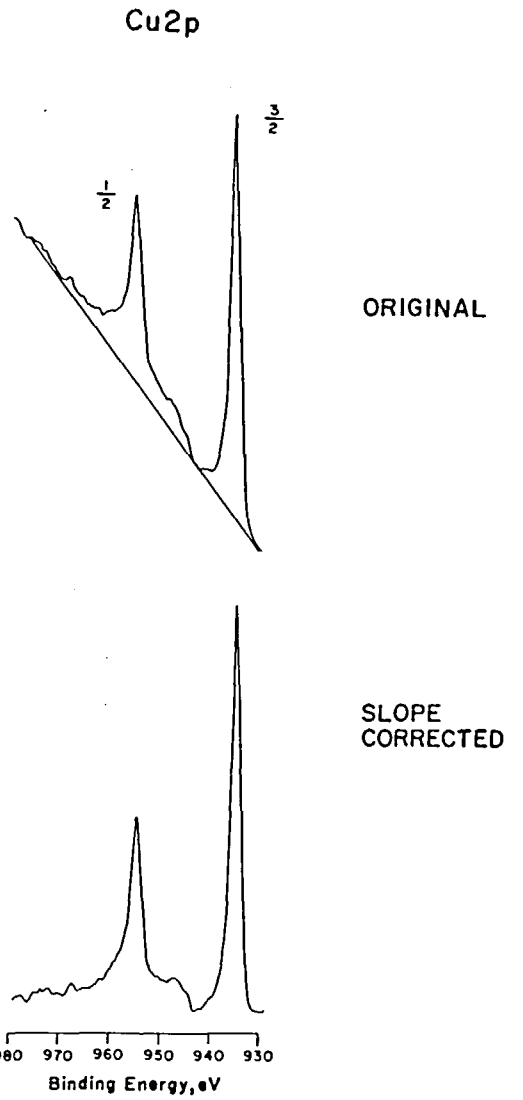

FIGURE 26. Correction of steeply sloping background.

A form of resolution enhancement is also possible with the use of multichannel analyzers, as illustrated by the spectra in Figure 27. The resolution enhanced spectrum shown in Figure 27 is obtained by a simple manipulation of data in the commercial multichannel analyzer available with an electron spectrometer.[93]

The use of a computer for digital data acquisition allows signal averaging of weak signals with a greater degree of flexibility than does the hard-wired multichannel analyzer since the number of data points obtainable in a given spectral region is typically variable over a wider range than that

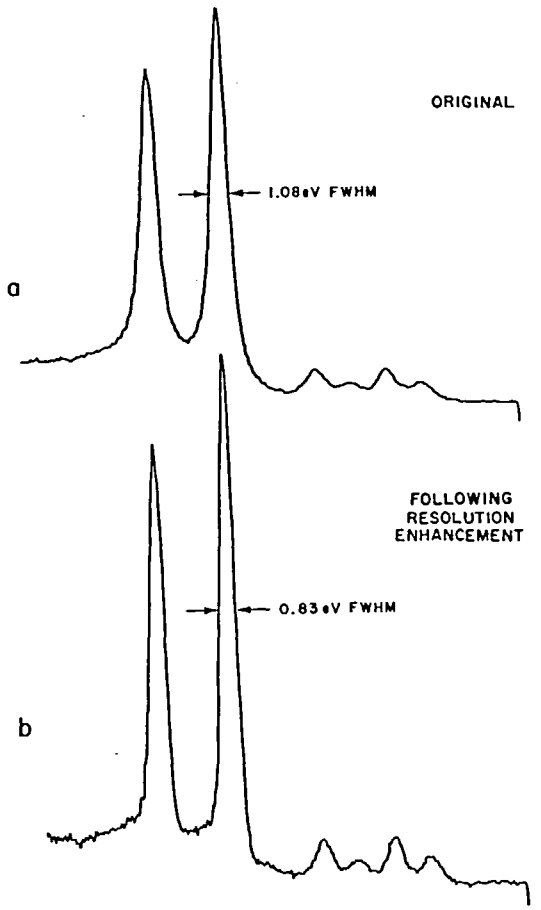

FIGURE 27. Resolution enhancement using multichannel analyzer. (From Du Pont Instruments Tech. Product Bull. #650–1010, June, 1975.)

available with a multichannel analyzer. Strictly for data acquisition, however, the signal averaging capability of a computer is roughly equivalent to that of a multichannel analyzer. The real advantage of a computer is that it can also be utilized to control the spectrometer. Data acquisition can be programmed in a number of spectral regions, and control can be transferred to the computer for unattended operation. The importance of this capability is inversely proportional to the intrinsic speed and sensitivity of the spectrometer. Highly sensitive spectrometers obtain data quickly enough that this ability becomes relatively unimportant. Conversely, a spectrometer with inherently slow data acquisition capabilities can make better use of computer control capability to conserve operator time.

Once data have been obtained in digital form, whether in a multichannel analyzer or in a computer, further data processing can produce important and useful results. If the data are obtained in a multichannel analyzer, means must be available to transfer them to an appropriate computer by punched paper tape, magnetic tape, or a direct MCA/computer interface. If the spectrometer is equipped with a sufficiently powerful computer, data processing can be accomplished directly with the dedicated computer. With many instruments, however, this prevents simultaneous operation of the spectrometer.

ESCA data lend themselves to data processing techniques for several reasons. Spectrometer functions are often known or can be determined or approximated. The inherent resolution of the technique is not great; therefore, the need exists for mathematical methods for deconvoluting closely overlapped spectra. Finally, peak shapes and widths are often known or constant.

The literature contains procedures for correction of background and curve fitting[94] as well as sophisticated techniques for data smoothing and deconvolution of the spectrometer function and Fourier-type resolution enhancement.[95,96] An example of the results which are obtainable using a variation of Van Cittert's method[97] due to Jansson and co-workers[98,99] is shown in Figure 28. In this case, polynomial filtering and physical constraints such as the prohibition of negative solutions are applied. When properly used, techniques of this sort have yielded results which are in satisfying agreement with theory. In general, the use of computer data manipulation techniques should grow in importance in ESCA in the future.

IV. APPLICATIONS OF ESCA TO SURFACE ANALYSIS

In this section of the paper, applications of ESCA to surface related problems are presented. This section is not intended to be a comprehensive review of the published applications. Rather, some selected studies are presented in order to demonstrate the broad utility of the ESCA technique to problems in both organic and inorganic surface chemistry. In the last part of this section, some principles and examples of in-depth analysis by ESCA using grazing angle and ion sputtering techniques are presented.

A. Organic Surface Analysis

One of the first applications of ESCA to surface analysis of organic materials was published by

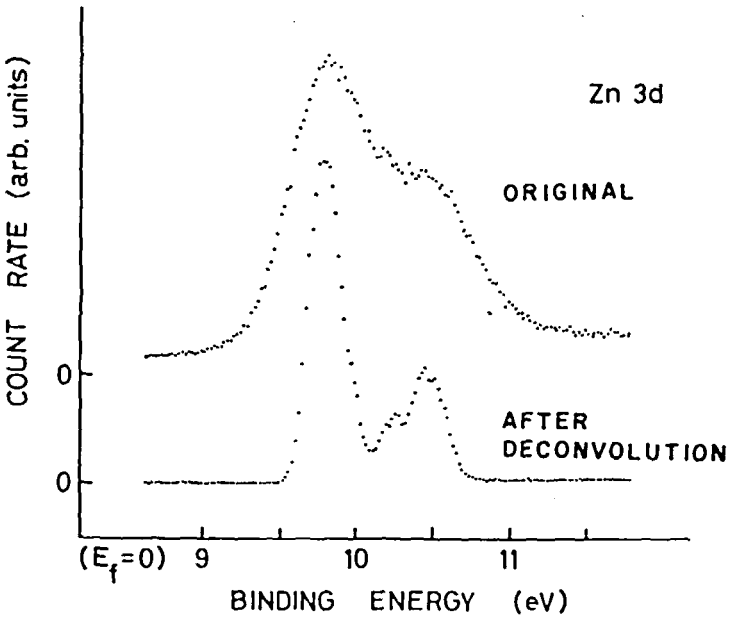

FIGURE 28. Resolution enhancement using a computer technique. [From McLachlan, A. D., Jenkin, J. G., Liesegang, J., and Leckey, R. C. G., *J. Electron Spectrosc. Relat. Phenom.*, 3, 207 (1974). With permission.]

Millard[100] and concerned the effects of corona discharge and low temperature discharge treatments on the surface chemistry of wool fibers. Millard studied the sulfur, nitrogen, carbon, and oxygen spectra of the wool fibers before and after the discharge treatments. The most significant changes were noted in the S_{2p} spectra, which are shown in Figure 29. The top spectrum was taken from untreated wool, while the middle and bottom spectra were taken from wool fibers which had been exposed, respectively, to a corona discharge and to a low temperature plasma in air. The top spectrum exhibits a large peak at ~163.5 eV due to the ~3.7% sulfur present in the wool as part of the amino acid cystine. A smaller peak at higher binding energy is also evident in this spectrum. The intensity of the small peak relative to that of the cystine sulfur peak increases substantially after exposure to both the corona discharge and the low temperature plasma. Its binding energy is characteristic of sulfur in the +6 oxidation state, and apparently the cystine sulfur is oxidized by the treatments to a sulfate ion or to some organic compound containing S^{+6}. The sulfur in the wool appears to be much more susceptible to oxidation than is nitrogen under the treatment conditions studied since no oxidized forms of nitrogen were detected in the N_{1s} spectra taken after the surface treatments.

Several problems in fluoropolymer surface chemistry have been studied by Dwight and Riggs[57] using ESCA combined with three other techniques – soft X-ray spectroscopy, contact angle hysteresis, and electron microscopy. One of these problems involved determining the etching mechanism of sodium in liquid ammonia (Na/NH_3) solutions on fluoropolymer films. Fluoropolymer films have several end uses which require bonding of the films to a substrate, but untreated fluoropolymers form joints of negligible strength with ordinary adhesives and require some type of pretreatment to increase their bondability. Treatment with Na/NH_3 is known to promote bondability. Line 1 of Figure 30 shows the C_{1s}, O_{1s}, F_{1s}, and Br_{3d} photoelectron spectra for poly-(tetrafluoroethylene/hexafluoropropylene) [Teflon® FEP] after etching with an Na/NH_3 solution. Lines 2 and 3 show the same spectra for an FEP control and for an Na/NH_3 etched film, respectively, after submerging in bromine-in-carbon tetrachloride solutions. The spectra in line 2 are essentially identical to those from an untreated FEP surface. A single high binding energy carbon peak at ~293 eV due to the fluorocarbon is seen along with a strong fluorine peak. No oxygen is detected on the untreated (or the Br_2/CCl_4 treated) surface. The ESCA spectra from the Na/NH_3 etched FEP film bear no

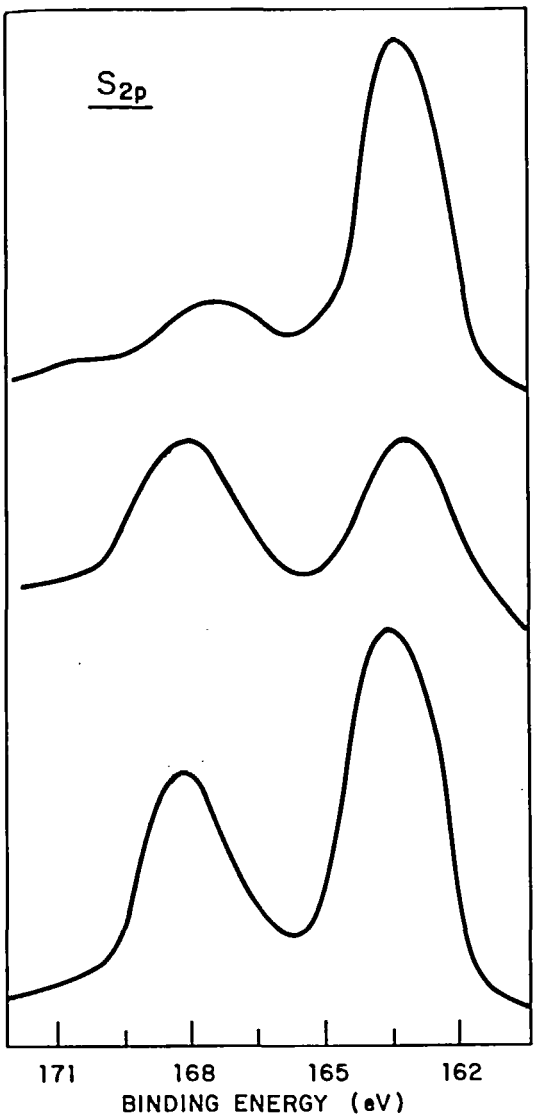

FIGURE 29. S_{2p} spectra from untreated wool fibers (top), corona discharge treated wool fibers (middle), and low temperature plasma discharge treated wool fibers (bottom). [From Millard, M. M., *Anal. Chem.*, 44(4), 828 (1972). With permission.]

resemblance to those from the control. The carbon peak is now centered at a lower binding energy of ~285 eV and exhibits a high binding energy tail extending to ~289 eV. Using an analog curve resolver, this carbon peak was fitted to three overlapping Gaussian curves, with the results shown in Figure 31. The binding energies of the three peaks are typical of hydrocarbon- (saturated or unsaturated), carbonyl-, and carboxyl-type carbon atoms. A large oxygen peak is also evident on the etched surface, and the fluorine intensity has been reduced compared to the control by more than an order of magnitude. To determine if the large hydrocarbon peak was due to saturated or unsaturated hydrocarbon, the etched film was subsequently submerged in bromine-in-carbon tetrachloride solution, the classical test for unsaturation. The spectra in lines 2 and 3 of Figure 30 indicate that no bromine was detected on an FEP control subjected to the same treatment, but that bromine was detected on the etched surface. In addition, compared to line 1, the central component of the C_{1s} spectrum in line 3 has increased in intensity relative to the hydrocarbon peak. Brominated carbon atoms are expected to exhibit a higher binding energy than hydrocarbon, and the central component of this group of peaks is probably a sum of the intensities from brominated and carbonyl carbon. Since the oxygen spectrum is essentially unchanged, the difference between the carbon spectra in lines 1 and 3 must be due to the introduction of bromine-carbon bonding, and at least some unsaturation is present on the surface of the etched film. By comparing these ESCA results with electron micrographs, the authors conclude that the solvated electrons in the Na/NH_3 etching solutions combine with and remove fluorine from the polymer surface. A condensed, highly reactive, sponge-like carbon network remains which reacts with the etching solvent and with atmospheric oxygen and moisture when it is removed from the solution. The result is a rough, porous hydrocarbon surface layer containing unsaturated and carbonyl and carboxyl groups.

B. Inorganic Surface Analysis

Hercules et al.[61] have devised a method for trace analysis of metals which utilizes the surface sensitivity of the ESCA technique. By flowing a solution containing the metal of interest through a glass fiber disk that had been silylized with dithiocarbamate functional groups, the authors were able to concentrate trace quantities of the metal on the surface of the glass disk by ion exchange. Figure 32 shows a spectrum from 1 of these glass fiber disks after flowing through a 100-ml solution containing 20 ppm of lead. The large peak at ~152 eV is due to silicon in the glass substrate, while the other 2 peaks at ~143 and 148 eV are due to lead $4f_{5/2}$ and $4f_{7/2}$ core levels from the lead concentrated on the glass surface. Using this method, the authors reported detection levels of ~10 ppb for Pb, Ca, Tl, and Hg, and they

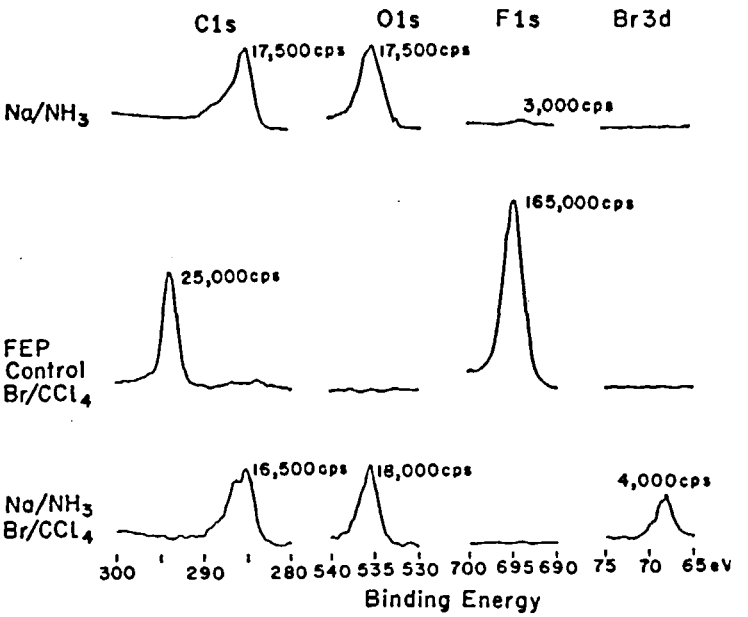

FIGURE 30. C_{1s}, O_{1s}, F_{1s}, and Br_{3d} spectra from Na/NH_3 etched FEP film (top), FEP control film (middle), and etched film (bottom) after immersion in bromine-in-carbon tetrachloride solutions. [From Dwight, D. W., and Riggs, W. M., *J. Colloid Interface Sci.*, 47(3), 650 (1974). With permission.]

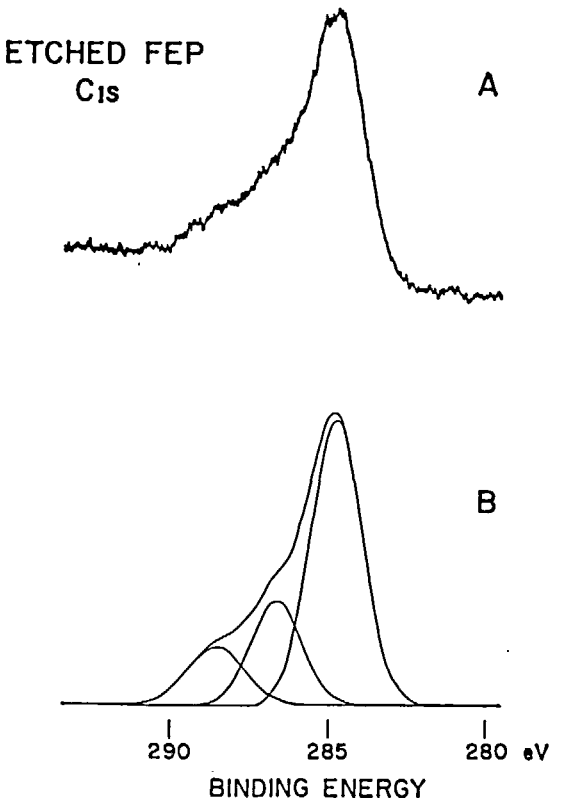

FIGURE 31. (a) Experimental and (b) Deconvoluted C_{1s} spectrum from Na/NH_3 etched FEP film. [From Dwight, D. W. and Riggs, W. M., *J. Colloid Interface Sci.*, 47(3), 650 (1974). With permission.]

estimate that under certain conditions, this could be extended to the parts per trillion range for the heavy metals.

Swingle, Ginnard, and Madden[101] have studied electroless nickel-boron coatings with ESCA in order to correlate the physical properties of the Ni-B system with changes in surface chemistry as the coating is heated in vacuum and heated in air. Such heat treated Ni-B coatings are very hard and are more wear resistant than tool steels, hard chromium, and a variety of other metallic coatings. In addition, the coatings are electrically conducting, resistant to air oxidation, and readily braised and soldered. ESCA spectra were taken after each of a series of sequential heat treatments. Only a portion of the data presented by the authors will be discussed here. Figures 33 and 34 compare the B_{1s}/S_{2p} and $Ni_{2p_{3/2}}$ spectra, respectively, from the coating as plated, after heating at 200°C for 90 min in vacuum, and after heating at 400°C for 90 min in vacuum. At least 3 distinct boron peaks at approximately 192, 188, and 182 eV are evident in Figure 33. Comparing the binding energies of these peaks with those of selected standards indicates that the high E_B peak at 192 eV is due to an oxide or mixed oxide of boron. The peak at 188.0 to 188.5 eV could be due to a number of boron containing species,

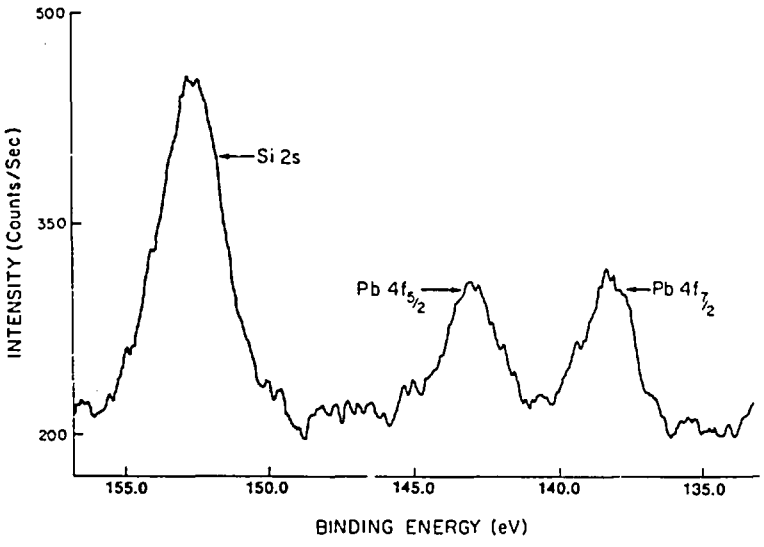

FIGURE 32. Si_{2s}–$Pb_{4f_{5/2}-7/2}$ spectrum from glass fiber disk after flowing 100 ml solution of 20 ppm lead through the disk. [From Carlson, S. A. and Hercules, D. M., *Anal. Chem.*, 45(11), 1794 (1973). With permission.]

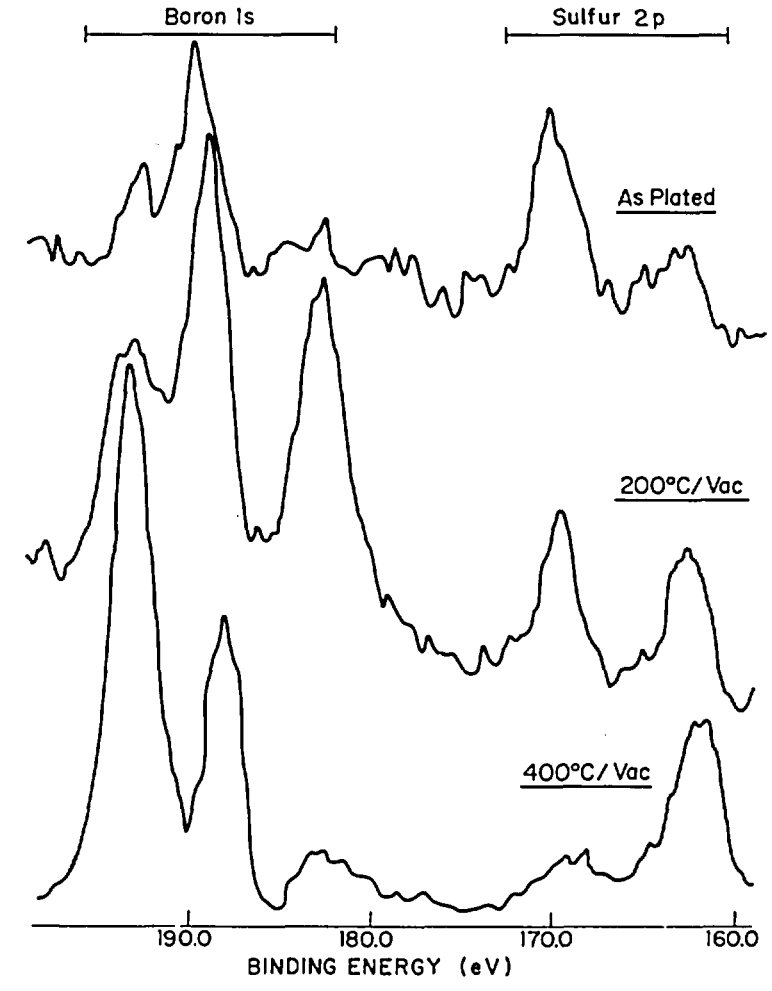

FIGURE 33. B_{1s}–S_{2p} spectra from Ni-B electroless plate as plated (top) after heating at 200°C in vacuum for 90 min (middle), and after heating 400°C in vacuum for 90 min. (From Swingle, R. S., II, Ginnard, C. R., and Madden, G. I., ESCA Studies of Nickel-Boron Electroless Coatings, presented at the Pittsburgh Conference on Analytical Chemistry, Cleveland, March, 1975.)

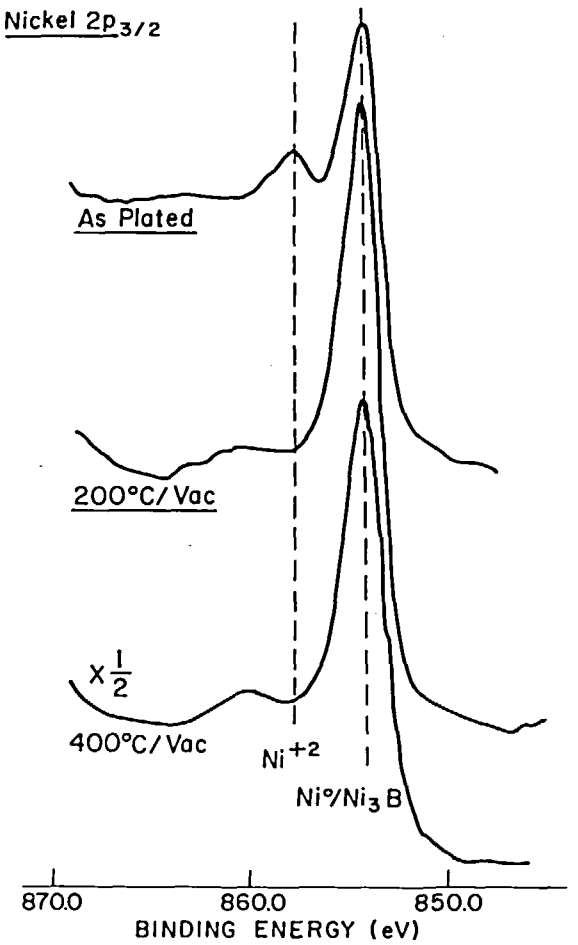

FIGURE 34. $Ni_{2p_{3/2}}$ spectra from Ni–B electroless plate as plated (top), after heating at 200°C in vacuum for 90 min (middle), and after heating 400°C in vacuum for 90 min. (From Swingle, R. S., II, Ginnard, C. R., and Madden, G. I., ESCA Studies of Nickel-Boron Electroless Coatings, presented at the Pittsburgh Conference on Analytical Chemistry, Cleveland, March, 1975.)

including the intermetallic Ni_3B phase believed to be present in the coating.[102] Note that both the 192- and 188-eV peaks show small changes in peak width and relative binding energies from treatment to treatment, indicating that more than 1 distinct species contributes to each of the peaks. The third peak at 182 eV presents a problem in interpretation since, to the authors' knowledge, no B_{1s} binding energies this low have been reported in the literature. At present, the authors feel that this species is due to boron, or possibly borohydride, which is randomly distributed in the Ni-B solid solution, and that extra-atomic relaxation accounts for the very low binding energy. Two sulfur peaks are also shown in Figure 33. The high E_B peak at 169.3 eV is characteristic of sulfate and arises from the Tl_2SO_4 stabilizer present in the coating bath. The second peak at 162.5 eV is characteristic of a sulfide and suggests that some sulfate is reduced to sulfide in the coating bath and codeposited with the other elements during the plating process. It is apparent that heating the coating in vacuum significantly alters its surface composition. The total amount of boron at the surface increases, and the two lower E_B boron species are partly oxidized. This oxidation is somewhat surprising in the 10^{-5}-torr vacuum of the reaction chamber and is in sharp contrast to the reduction evident in the nickel and sulfur spectra. Note that the sulfate/sulfide ratio decreases from 2.5 in the "as plated" condition to 0.25 after heating at 400°C in vacuum. In addition, Figure 34 shows that the small amount of Ni^{+2} on the surface of the "as plated" coating is completely removed after the first heat treatment. Even at 400°C, where oxidation is more likely, there is no formation of Ni^{+2}. Figures 35 and 36 compare the B_{1s}/S_{2p} and $Ni_{2p_{3/2}}$ spectra, respectively, after subsequently heating the Ni-B coating in air at 200°C for 90 min and at 400°C for 30 min. As expected, the surface composition of the coating changes drastically under these treatment conditions. Boron is further oxidized, with only a single boron oxide peak at 192.7 eV in evidence after heating at 400°C. The sulfide is reoxidized to sulfate, and the $Ni_{2p_{3/2}}$ spectrum, taken after heating at 400°C in air, shows both the chemical shift and the shake-up satellite structure characteristic of the high spin +2 oxidation state. Note that even after heating in air at 400°C, a peak due to Ni^0/Ni_3B is still evident. In order to observe this peak with the ESCA technique, the oxide layer formed above the Ni^0/Ni_3B cannot have a thickness greater than 2 to 3 times the mean escape depth, λ, of the nickel $Ni_{2p_{3/2}}$ electron. Thus if λ is of the order of 15 to 20 Å, this layer is likely to have a thickness $\lesssim$60 Å. This is somewhat surprising considering the harsh conditions of these sequential treatments. (The $Ni_{2p_{3/2}}$ ESCA spectrum of Ni foil, for example, shows no peak due to Ni^0 after being heated in air at 400°C.) It is apparent that the oxide layer on Ni-B effectively "passivates" the coating and presents a very strong barrier to further oxidation. It is not possible to deduce the exact composition of this protective layer from the ESCA data alone;

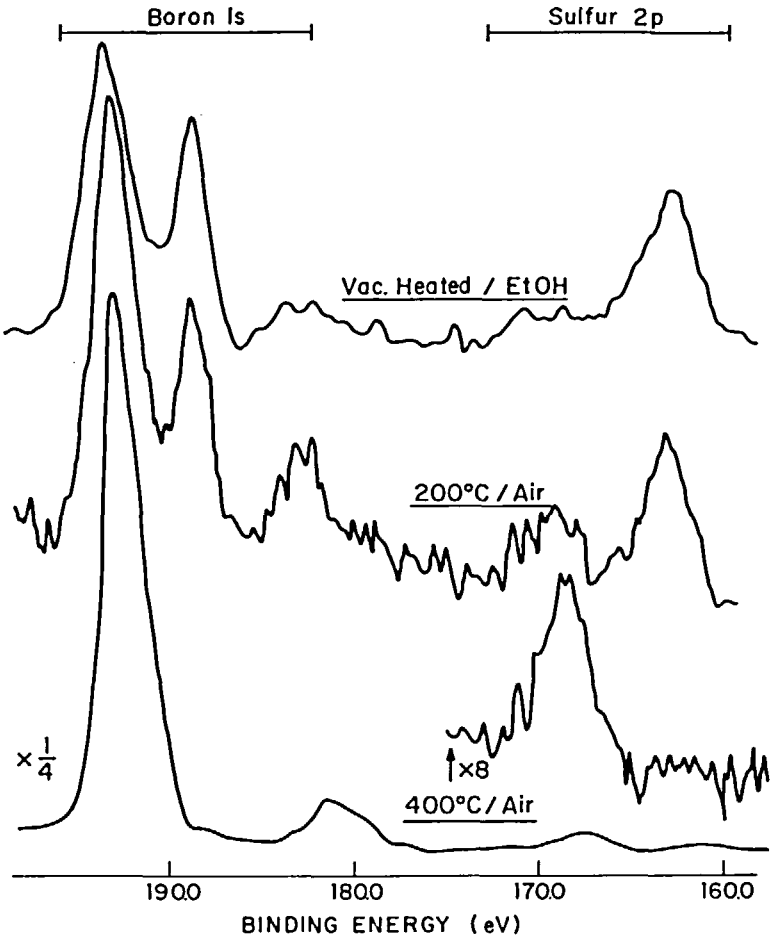

FIGURE 35. B_{1s}–S_{2p} spectra from Ni–B electroless plate after vacuum/heat treatments (top), after heating at 200°C in air for 90 min (middle), and after heating at 400°C in air for 30 min. (From Swingle, R. S., II, Ginnard, C. R., and Madden, G. I., ESCA Studies of Nickel-Boron Electroless Coatings, presented at the Pittsburgh Conference on Analytical Chemistry, Cleveland, March, 1975.)

however, several important conclusions concerning its nature are evident. First, the $Ni_{2p_{3/2}}$ binding energy of the Ni^{+2} species is consistently 0.5 to 0.9 eV higher than that for simple NiO, suggesting that nickel oxidation products other than NiO must be present. Second, large amounts of other elements present in the coating bath, including carbon and thallium, are detected in the coating and must be codeposited with the nickel and boron in the coating process. (The authors show Tl_{4f} spectra which indicate substantial Tl enhancement of the surface after heating at 400°C in air.) Last, in contrast to nickel, all the boron detected after heating at 400°C in air has been oxidized. Because λB_{1s} is greater than λNi_{2p}, this result suggests that the oxide layer is not homogeneous with depth and that boron is preferentially oxidized toward the bottom of the coating. This conclusion is in agreement with the preferential boron oxidation noted in the vacuum heat treatments and probably accounts for the oxidation resistance of the Ni-B coating.

Heterogeneous catalysis is another field where the characterization of solid surfaces is of great importance. Applications of ESCA in this area have been recently reviewed by Riggs and Parker[103] and by Brinen[104] and, except for the brief example below, will not be discussed in detail. Figure 37 shows the X-ray photoelectron spectra taken from a charcoal supported palladium catalyst used in the reduction of a nitrogen containing organic compound.[105] The purpose of

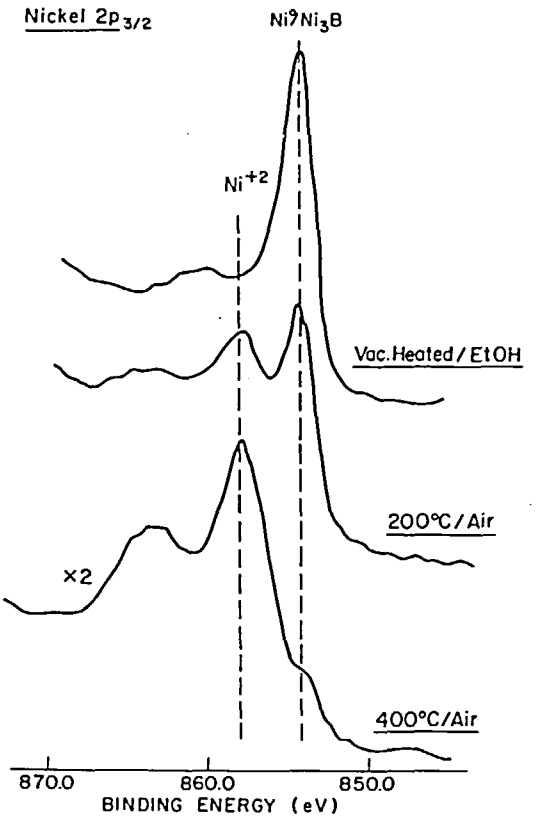

FIGURE 36. $Ni_{2p_{3/2}}$ spectra from Ni–B electroless plate after vacuum/heat treatments (top), after heating at 200°C in air for 90 min (middle), and after heating at 400°C in air for 30 min. (From Swingle, R. S., II, Ginnard, C. R., and Madden, G. I., ESCA Studies of Nickel-Boron Electroless Coatings, presented at the Pittsburgh Conference on Analytical Chemistry, Cleveland, March, 1975.)

the study was to determine the cause of catalyst deactivation. Poisoning of the catalyst surface by either sulfide or chloride compounds was suspected as the cause of the deactivation since X-ray fluorescence indicated no difference in the total palladium content between active and inactive catalyst samples. The ESCA spectra, however, show that both sulfur and chlorine are absent on the spent catalysts and that, compared to the active catalyst, a large amount of nitrogen is present. In addition, the inactive catalyst exhibits a much lower palladium intensity, indicating that some nitrogen-containing by-product of the reaction is coating the surface of the catalyst and blocking the active palladium sites. This hypothesis is supported by the large increase in palladium intensity and reduction in nitrogen intensity (Figure 38) found after ion sputtering the spent catalyst.

C. In-depth Analysis

In solving many chemical problems, it is useful to determine atomic composition and oxidation state information as a function of depth into the sample. Using ESCA, this "depth profiling" can be accomplished with either grazing angle[79,80] or ion sputtering[91] techniques. Some principles, relative advantages, and examples of each technique are presented below.

Figure 39 illustrates the general principle of grazing angle ESCA for a specular surface. The effective sampling depth of the ESCA technique is related to $\lambda \sin \theta$, where λ is the inelastic mean free path of the photoelectron in a solid (see Section II.C), and θ is the take-off angle of the photoelectron with respect to the plane of the sample surface. In the grazing angle experiment, spectra are taken as a function of θ, and at θ = 15°, for example, the sampling depth is about ¼ (sin 15° ≅ 0.25) of that for θ = 90°. Grazing angle has two important advantages compared to ion sputtering. First, it is nondestructive in nature and permits oxidation states to be measured as a function of depth. (The latter may not be possible with ion sputtering due to the preferential sputtering effects mentioned below.) Second, for most spectrometers, grazing angle is inexpensive to implement since only the geometry of the sample-to-analyzer entrance need be altered. Expensive accessories are not generally required. The most important disadvantage of grazing angle compared to ion sputtering is that samples can only be profiled over a depth equal to two or three times λ. For most samples, λ lies in the range of 10 to 30 Å, and ion sputtering is necessary for profiles beyond 50 to 100 Å in depth.

The usefulness of grazing angle for enhancing the surface sensitivity of ESCA has been illustrated by M. W. Duch[106] using a model system consisting of an absorbed monolayer of perfluorodecanoic acid on glass. Figure 40 shows the C_{1s} spectra from this system taken at θ = 90° and θ = 15°. At θ = 90°, a large C_{1s} peak is seen at 285.0 eV due to the hydrocarbon contaminant. The higher binding energy structure at 290 to 300 eV is difficult to interpret due to the overlap of the chemically shifted C_{1s} peaks from the fluorocarbon and carboxyl carbon atoms with the $K_{2p½-3/2}$ doublet from potassium in the glass substrate. At θ = 15°, the $K_{2p½-3/2}$ peaks are almost completely removed from the spectrum, and 3 peaks are seen at ~289, 292, and 294 eV due to the $-CO_2-$, $-CF_2-$, and CF_3- groups,

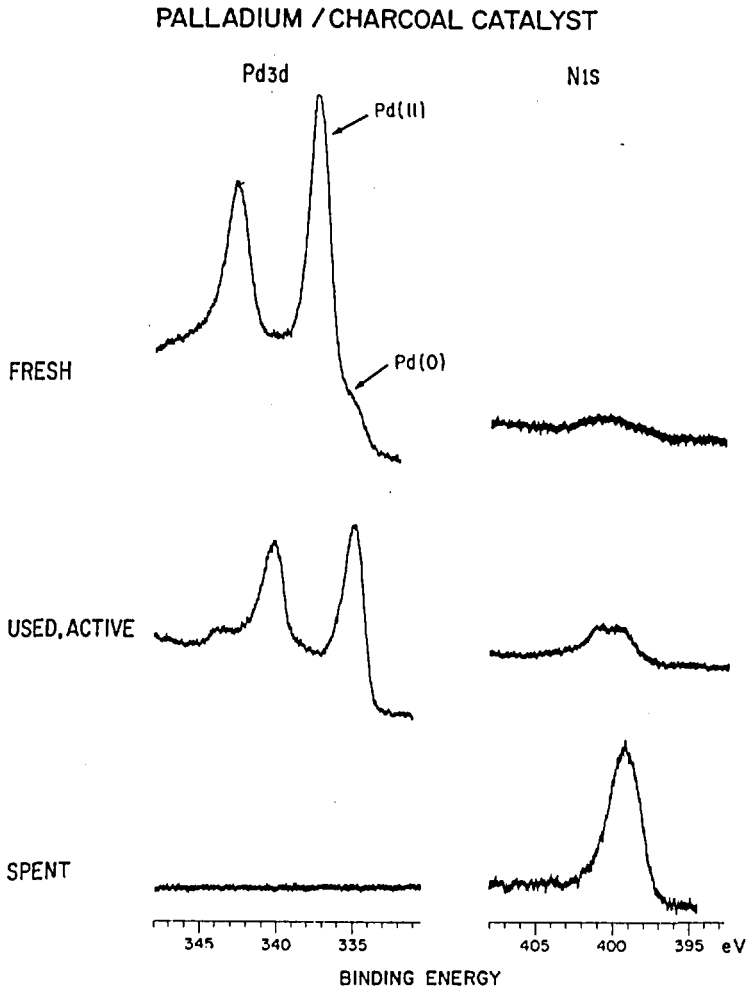

FIGURE 37. $Pd_{3\,d_{3/2\text{-}5/2}}$ and N_{1S} spectra from fresh (top), used but active (middle), and used but inactive (bottom) charcoal supported palladium catalyst. (From Ginnard, C. R., Du Pont Applications Data, Bull. ES–0007, February, 1974.)

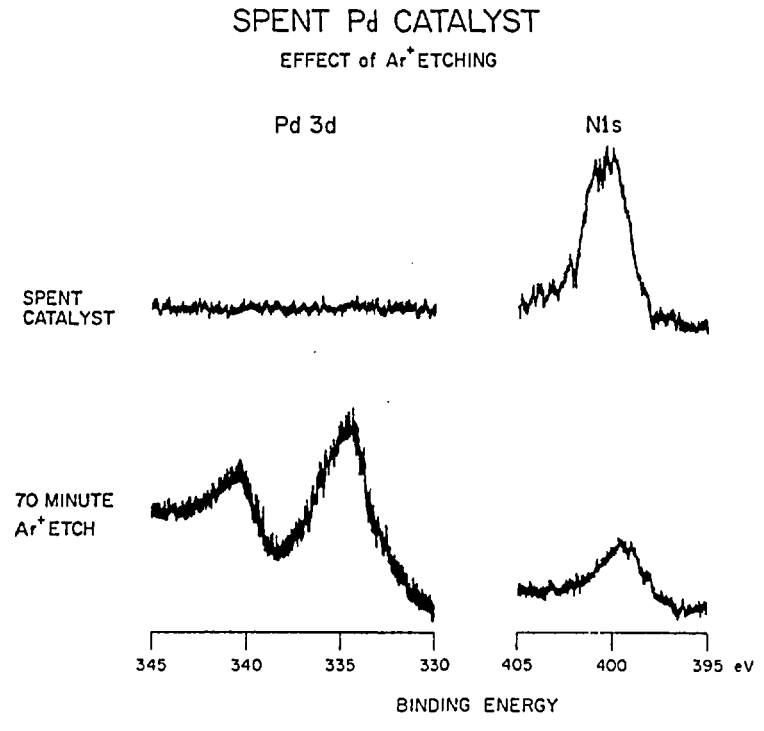

FIGURE 38. $Pd_{3\,d_{3/2\text{-}5/2}}$ and N_{1S} spectra from spent charcoal supported palladium catalyst before (top) and after (bottom) ion sputtering. (From Ginnard, C. R., Du Pont Applications Data, Bull. ES–0007, February, 1974.)

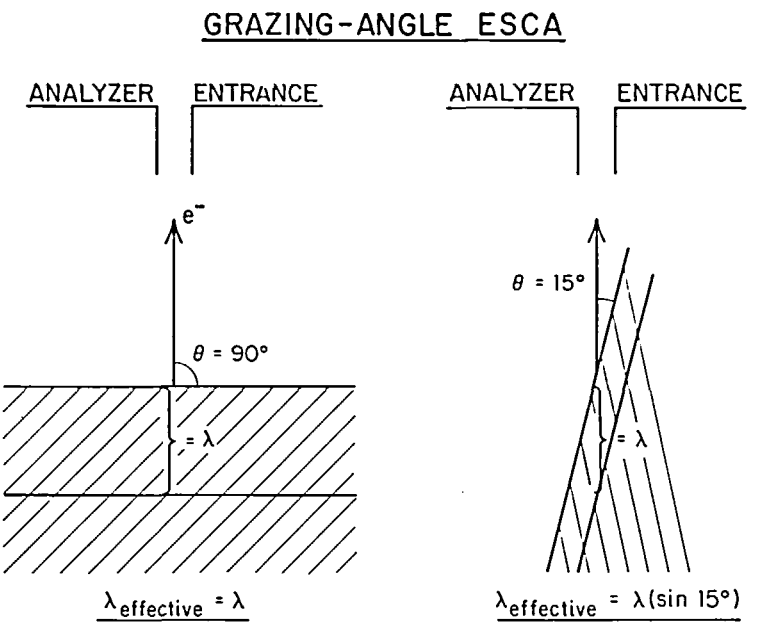

FIGURE 39. Principles of grazing-angle ESCA for specular surfaces.

respectively, in the adsorbed molecule. Note the increased intensity of the CF_3- peak relative to that of the -CO_2- peak, even though the same number of CF_3- and -CO_2- carbon atoms are present in the adsorbed molecule. This is probably due to the orientation of the adsorbed perfluorodecanoic acid molecules, with the polar -CO_2- group localized primarily at the glass-adsorbate interface and the -CF_2- group localized primarily at the adsorbate-vacuum interface.

Grazing angle ESCA has been used by Swingle, Groff, and Monroe[107] to study the surface of single crystals of the organic charge-transfer complex, tetrathiafulvalene-tetracyanaquinodimethane (TTF-TCNQ). The complex is of interest because of its one-dimensional metallic character and reported superconductivity fluctuations at 60K.[108,109] Unusual structure in both the N_{1s} and the S_{2p} spectra of this complex had been reported,[110,111] and the study was undertaken to determine if this multipeak structure resulted from shake-up or from chemical shift due to different amounts of electron transfer at the surface of the crystals compared to the bulk. Figure 41 compares typical background corrected N_{1s} spectra from TTF-TCNQ taken at $\theta = 90°$ and $\theta = 15°$. The $\theta = 90°$ spectrum exhibits the multipeak structure characteristic of TTF-TCNQ, while the $\theta = 15°$ spectrum is dominated by a single peak at 399.0 eV. Similar changes with θ are evident in the S_{2p} spectra from TTF-TCNQ, and it is apparent that at the *ab* crystal surface of the complex, there is a thin layer of TTF-TCNQ (from one to five molecules thick) that is distinguishable from the bulk. By comparing the absolute N_{1s} and S_{2p} binding energies from TTF-TCNQ with those from selected standards, the authors conclude that this surface layer exhibits little or no electron transfer compared to 0.8 ± 0.2 electron transfer in the bulk.

In the ion sputtering method of depth profiling, X-ray photoelectron spectra are taken before and after bombarding the sample with a beam of energetic (usually ~500 to 2000 eV) ions. The sputtering action of the ion beam slowly etches away the sample surface with time,[91] exposing the underlying atomic layers. It is not yet clear if ion sputtering can be generally applied to depth profiling of organic materials. However, the technique has been applied to all types of inorganic materials and, for example, has been used by Coad and Cunningham[112] to study the composition of oxide films on chrome steels. These authors found thin regions that were rich in chromium adjacent to the metal-oxide interface.

When interpreting changes in X-ray photoelectron spectra as a function of sputtering time, care must be taken to insure that these changes result from compositional changes with depth in the sample and not from preferential sputtering.

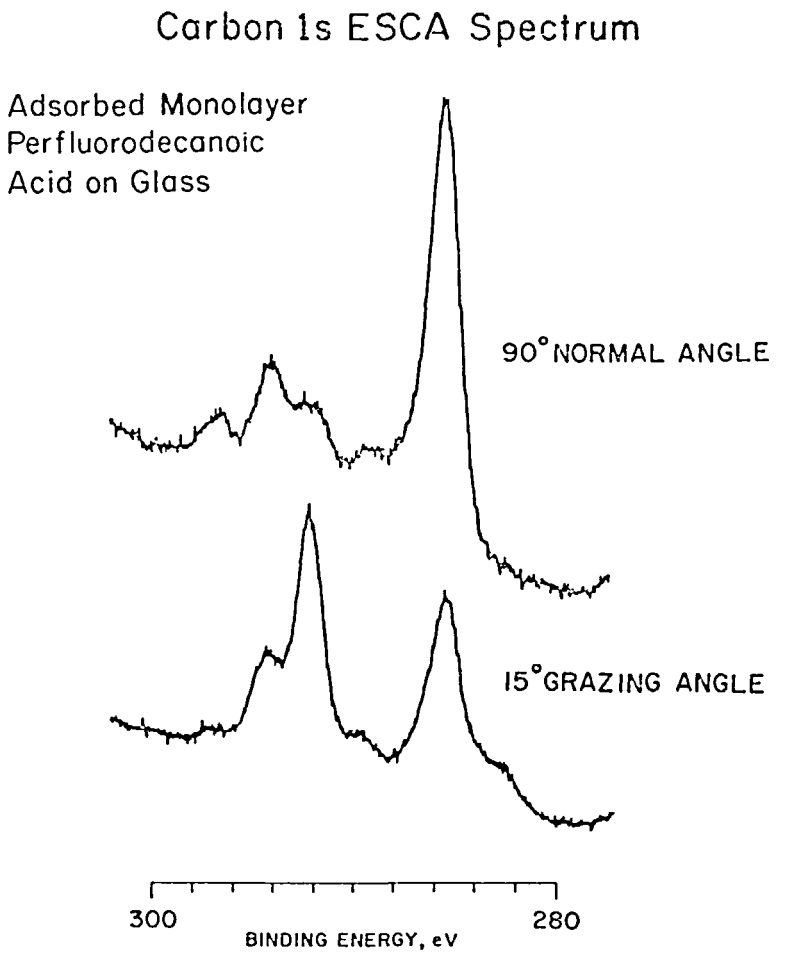

FIGURE 40. $K_{2p_{1/2-3/2}}-C_{1s}$ spectra at $\theta = 90°$ (top) and $\theta = 15°$ (bottom) for a monolayer of perfluorodecanoic acid adsorbed on glass. (From Duch, M. W., personal communication, 1975.)

For example, it is now known that many metal oxides are reduced to the corresponding metal or to lower oxides by Ar^+ sputtering because oxygen, with its high sputtering yield and high volatility, is more likely to escape the sample than is the metal. This fact has even been used by Yin, Ghose, and Adler[81] to generate FeO from Fe_2O_3 *in situ* and to study changes in iron core electron binding energies with iron oxidation states. Kim et al.[82] have studied 26 metal oxides with ESCA before and after ion sputtering, and they found a direct correlation between the free energy of formation of the metal oxide and the tendency of the oxide to be reduced by an Ar^+ ion beam.

V. COMPARISON WITH OTHER SURFACE ANALYSIS TECHNIQUES

In this section, ESCA is briefly compared with three other modern, high vacuum, spectroscopic techniques for solid surface analysis. These techniques are Auger Electron Spectroscopy (AES),[93] Ion Scattering Spectroscopy (ISS),[113] and Secondary Ion Mass Spectrometry (SIMS).[114] Many other techniques for surface analysis have been discussed in the literature, but they will not be mentioned here because they (1) are concerned with the physical rather than the chemical nature of surface (e.g., Scanning Electron Microscopy), (2) are only applicable to well-defined surfaces under ultrahigh vacuum (e.g., Low Energy Electron Diffraction and UV Photoelectron Spectrometry), (3) probe too deeply into a sample (e.g., Attenuated Total Reflectance Infrared and Soft X-ray Fluorescence), or (4) have not yet been developed to a point where they can be routinely applied to analytical samples (e.g., Ion Neutralization Spectrometry and Inelastic Electron Back-

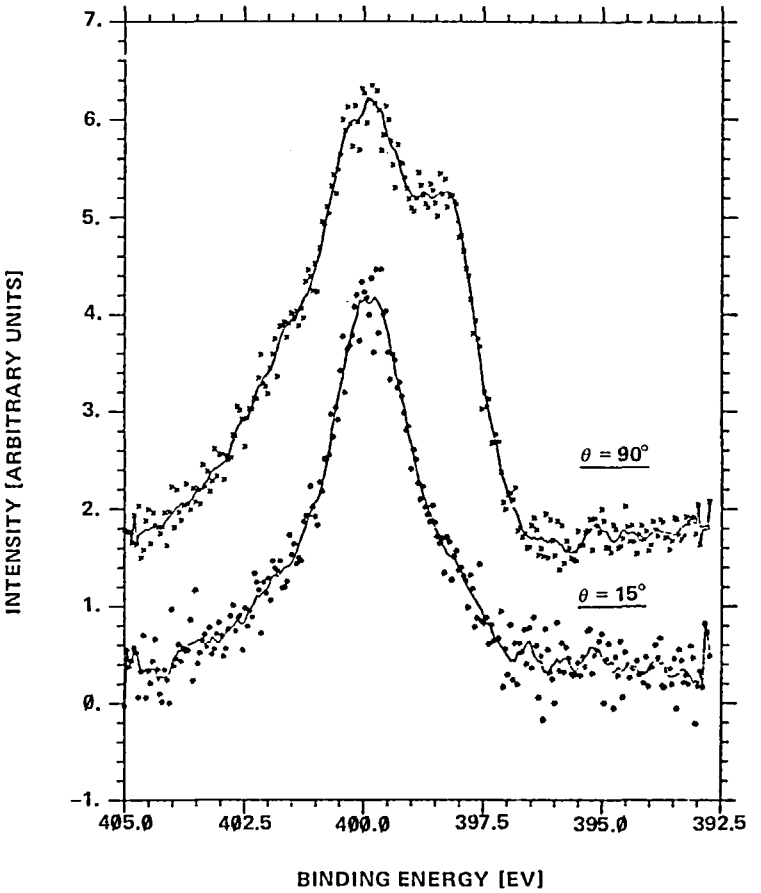

FIGURE 41. Background corrected N_{1s} spectra from single crystals of TTF-TCNQ taken at $\theta = 90°$ (top) and $\theta = 15°$ (bottom). [From Swingle, R. S., II, Groff, R. P, and Monroe, B. M., *Phys. Rev. Lett.*, 35(7), 452 (1975). With permission.]

scattering Spectrometry). ESCA, AES, ISS, and SIMS are all commercially available and well established in the literature. A brief description of the basic principles of each of these techniques is given separately below. This is followed by some general remarks concerning the relative strengths and weaknesses of the techniques.

A. ESCA

In the ESCA experiment, a solid surface is exposed to X-rays of energy $h\nu$, and the kinetic energy distribution of the ejected photoelectrons is measured. The resulting spectrum is usually plotted as intensity versus E_B, the electron binding energy, where E_B is given approximately by:

$$E_B = h\nu - E_K \quad (20)$$

Each core level of every atom in the periodic table has a characteristic range of binding energies. The exact binding energy of a photoelectron line can often be used as a measure of element oxidation state.

B. AES

Auger electrons result from relaxation of a core level (level 1) ionized atom. In the first step of this relaxation process, an electron from a level of higher energy (level 2) falls into the level 1 vacancy. The difference in energy between the two levels ($E_{B_1} - E_{B_2}$) is then emitted either as an X-ray photon, which is the basis of X-ray fluorescence, or as an Auger electron from level 3, leaving a doubly ionized atom. The Auger electrons have kinetic energies characteristic of the atom and given approximately by:

$$E_K \cong E_{B_1} - E_{B_2} - E_{B_3} \quad (21)$$

Unlike the ESCA technique, the Auger electron kinetic energy is independent of the energy used for primary ionization. In the commercial spectrometers, the initial ionization of the atoms in the sample is accomplished with an electron beam. The Auger spectrum is usually plotted as the first derivative of the intensity with respect to kinetic energy, dN/dE_k, versus kinetic energy in order to eliminate the high background in the spectrum from the large number of backscattered primary electrons.

C. ISS

In this technique, a solid surface is bombarded with a collimated beam of monoenergetic noble gas ions, usually $^4He^+$, $^3He^+$, $^{20}Ne^+$, or $^{40}Ar^+$. A small fraction of these ions will undergo binary, elastic collisions with atoms in the first monolayer of the sample and will be reflected from the surface. For a 90° scattering angle, classical collision theory shows that the mass, M_1, of the reflecting atom at the sample surface can be calculated from:

$$E_1/E_0 = \frac{M_1 - M_0}{M_1 + M_0} \tag{22}$$

where E_0 and M_0 are the energy and mass of the incident ion, respectively, and E_1 is the energy of the reflected ion. In the commercial spectrometer, the ions scattered at 90° are energy analyzed, and a spectrum of intensity versus E_1/E_0 is produced.

D. SIMS

In this method, a solid surface is bombarded with an ion beam, and the secondary or sputtered ions ejected from the surface by the action of the beam are mass analyzed with a mass spectrometer. Conventional mass spectra are produced and, with the appropriate electronics, both positive and negative ion SIMS are possible.

E. Summary Comparison

Table 6 compares these four techniques in nine important categories. Depth resolution is about the same in ESCA and AES since the sampling depths of both techniques are governed by the inelastic mean free paths, λ, of the electrons in solids. Experimentally, λ has been shown to vary from 5 to ~100 Å depending upon the matrix and the exact kinetic energy of the electron being considered. Most λ values fall in a range of 10 to 30 Å, however, and for specular surfaces, the effective sampling depth can be reduced to 1 to 2 atomic layers using grazing angle techniques. The sampling depth in the ion techniques (ISS and SIMS) depends upon the sputtering rate of the sample relative to the scan time necessary to collect a spectrum. The sputtering rate, in turn, depends upon the mass of the incident ions and the current density of the incident ion beam. When a beam current of 1 μa is defocused over 1 cm^2 of the sample surface, the beam current density of 1 $\mu a/cm^2$ will result in a SIMS depth resolution of ~1 to 5 atomic layers depending upon the matrix, the scan time, and whether or not cratering or edge effects are important. If the same 1 μa ion beam is then focused to a spot ~30 μm in diameter, the beam current density is increased by greater than 4 orders of magnitude to ~50 mA/cm^2. The sputtering rate is increased and the depth resolution is decreased proportionately (for constant scan time). Rastering the ion beam across the sample surface can improve the depth resolution significantly and is an important feature for secondary ion mass spectrometers which employ large current densities. The sampling depth for ISS is a single monolayer. Incident ions that penetrate past the first monolayer have a high probability of being neutralized by the matrix, and neutrals are not detected by the ion scattering spectrometer even if they are elastically reflected at a 90° scattering angle.

The ESCA technique has no spatial resolution, and the signal is an integral of photoelectrons from all irradiated portions of the sample. A sample can be as small as ~1 mm^2. The electron beam diameter in commercial AES instruments may be as small ~5 to 10μm, and spectrometers with imaging capability are commercially available. The ion beam diameter in the commercial ISS instrument ranges from several millimeters to ~250 μm in diameter, and at present, the technique has little or no spatial resolution compared to some commercial AES instruments.

The range of costs for present commercial spectrometers is given in column 3 of Table 6. The exact price depends greatly upon the data acquisition system and the number of accessories purchased with each basic spectrometer. For a simple SIMS attachment to an existing vacuum system, an ion gun and mass spectrometer can be purchased for approximately $25,000. A complex ESCA system can cost over $200,000, while ion

TABLE 6

Modern Vacuum Techniques for Surface Analysis

	Depth resolution	Spatial resolution	Cost ($)	Qualitative analysis	Quantitative analysis	Chemical information	Surface damage	Monolayer sensitivity
ESCA	10–30 Å	None	60–200K	Good	Good	Yes	1	10^{-1} to 10^{-3}
AES	10–30 Å	As small as 5–10 μm	60–150K	Good	Fair	Limited at present	2	10^{-2} to 10^{-3}
ISS	1 monolayer	None to ~250 μm depending upon beam diameter	45–75K	Fair	Fair	Not generally available	3	10^{-1} to 10^{-2}
SIMS	1 monolayer	None to 1–2 μm depending upon beam diameter	25K without vacuum system	Good	Poor	Very limited	3	Extremely variable

microprobes with imaging capabilities can exceed $300,000.

The ability of the techniques to qualitatively analyze a surface is shown in column 4. Both ESCA and AES easily detect all elements in the periodic table, with the notable exception of hydrogen. Some overlapping of peaks is found in ESCA and AES spectra, but this is generally not a problem for qualitative analysis because most elements exhibit more than one peak. ESCA and AES do not distinguish between different isotopes of the same element. ISS is rated fair in this category because of its poor sensitivity for elements with atomic numbers below oxygen and the poor mass resolution of the technique at high mass. The latter problem is partly overcome by using noble gases of high mass (e.g., $^{40}Ar^{+}$) as the probe, but then elements with masses less than the probe mass are not detected. ISS can resolve some isotopes, notably ^{16}O and ^{18}O. All modern mass spectrometers have sufficiently high resolution to resolve nominal masses to ~500 and, consequently, SIMS resolves all isotopes in the periodic table. Overlap between ions of the same mass is often a problem since both monatomic and polyatomic clusters are sputtered as ions from solid surfaces. Relative natural abundances of different isotopes and higher mass resolution can aid in qualitative peak identification. SIMS has a unique and important advantage over all three of the other techniques in that it can detect hydrogen.

Column 5 rates the techniques in their abilities to perform quantitative analysis. Quantitative surface analysis by ESCA has been treated extensively in Section II.B and will not be discussed here. AES has the same general problems with sampling depth variability found in ESCA. In addition, the interaction probability of the ionizing electrons with bound electrons is not as well characterized as X-ray interaction and, because the spectrum is usually displayed at a first derivative, only peak heights can be used for quantitation. Different line widths are not taken into account. In ISS, quantitative accuracy depends upon an elastic scattering cross-section which can be calculated and upon a neutralization probability which, for some elements, is matrix dependent. More work on quantitative analysis by ISS needs to be done, but it presently appears that by using suitable standards, quantitative results are possible which are comparable to the precision and accuracy attainable with ESCA and AES. Quantitative analysis with SIMS is not possible using noble gas ion beams. In these cases, secondary ion emission coefficients vary by approximately seven orders of magnitude across the periodic table, and, for a single element, are extremely matrix dependent. Work using O_2^{+} ion beams has had some success in quantitative analysis.[116]

Column 6 compares the techniques with regard to their ability to extract chemical information other than composition. Chemical shift, Auger

parameters, shake-up satellites, and multiplet effects can all be used to obtain oxidation state or electronic environment information from ESCA. This potential is also present in AES, but generally has not been explored. AES spectra interpretation is more complex in this regard, and most commercial instruments with single-pass cylindrical mirror analyzers (CMA) do not have sufficient resolution to detect small chemical shifts in Auger lines. ISS has not been used to extract chemical information, but recent work indicates this may be possible in the future for a limited number of cases.[117] In general, for the ion techniques, chemical information below the first atomic layer is lost due to preferential sputtering. SIMS gives very limited chemical information. Interpretation of cracking patterns and cluster ions arising from the sputtering of solid surfaces has not yet advanced to the state-of-the-art found for ions produced in the gas phase.

Column 7 lists the relative order of surface damage produced by the four techniques. ESCA is the only one which readily lends itself to the analysis of organic materials. The electron beam excitation used in AES severely damages (or even destroys) organic materials. ISS and SIMS, because they are ion techniques, are not "nondestructive" in nature. In these cases, the surface is slowly removed by sputtering during the measurement.

Column 8 lists the approximate sensitivities in monolayers for ESCA, AES, and ISS. These numbers are variable depending upon the element under consideration and the surface morphology of the sample. Sensitivity for the SIMS technique is extremely variable, as pointed out in the discussion on quantitative analysis.

It should be clear from this discussion that each of the techniques has its strengths and weaknesses. No single technique is a panacea for all surface analysis problems, and the one most applicable to a particular laboratory will depend upon the type of problems encountered in that laboratory. In many cases, a combination of two or more of these techniques may be more useful than one alone.

REFERENCES

1. Siegbahn, K., Nordling, C., Fahlman, A., Nordberg, R., Hamrin, K., Hedman, J., Johansson, G., Bergmark, T., Karlsson, S., Lindgreen, I., and Lindberg, B., *ESCA-Atomic, Molecular and Solid State Structure Studied by Means of Electron Spectroscopy,* Almqvist and Wiksell, Uppsala, Sweden, 1967.
2. Siegbahn, K., Nordling, C., Johansson, G., Hedman, J., Heden, P. F., Hamrin, K., Gelius, U., Bergmark, T., Werme, L. O., Manne, R., and Baer, Y., *ESCA Applied to Free Molecules,* American Elsevier, New York, 1969.
3. Betteridge, D. and Williams, M. A., *Anal. Chem.,* 46(5), 125R (1974).
4. Hercules, D. M. and Carver, J. C., *Anal. Chem.,* 46(5), 133R (1974).
5. Hamnett, A. and Orchard, A. F., *Electron. Struct. Magn. Inorg. Compd.,* 1, 1 (1972).
6. Evans, S. and Orchard, A. F., *Electron. Struct. Magn. Inorg. Compd.,* 2, 1 (1973).
7. Hamnett, A. and Orchard, A. F., *Electron. Struct. Magn. Inorg. Compd.,* 3, 218 (1974).
8. Baker, A. D., Brundle, C. R., and Thompson, M., *Chem. Soc. Rev.,* 1(3), 355 (1972).
9. Swartz, W. E., Jr., *Anal. Chem.,* 45(9), 788A (1973).
10. Brundle, C. R., *Surf. Defect Prop. Solids,* 1, 171, 1972.
11. Gelius, U., *Phys. Scr.,* 9(3), 133 (1974).
12. Shirley, D. A., *Adv. Chem. Phys.,* 23, 85 (1973).
13. Dekeyser, W., Fiermans, L., Vanderkelen G., and Vennik, J., Eds., *Electron Emission Spectroscopy,* D. Reidel Publishing, Boston 1973.
14. Shirley, D. A., Ed., *Electron Spectroscopy,* American Elsevier, New York, 1972.
15. Baker, A. D. and Betteridge, D., *Photoelectron Spectroscopy – Chemical and Analytical Aspects,* Pergamon Press, New York, 1972.
16. Sevier, K. A., *Low Energy Electron Spectrometry,* Interscience, New York, 1972.
17. Citrin, P. H., Shaw, R. W., Jr., Packer A., and Thomas T. D., in *Electron Spectroscopy,* Shirley, D. A., Ed., American Elsevier, New York, 1972, 691–702.
18. Carley, A. F., Joyner, R. W., and Roberts, M. W., *Chem. Phys. Lett.,* 27(4), 580 (1974).
19. Nathan, R. and Hopkins, B. J., *J. Phys. E.,* 7(10), 851 (1974).

20. Ascarelli, P. and Missoni, G., *J. Electron Spectrosc. Relat. Phenom.*, 5, 417 (1974).
21. Citrin, P. H. and Hamann, D. R., *Phys. Rev. B:*, 10(12) 4948 (1974).
22. Waugh, J. L. T., *The Constitution of Inorganic Compounds*, Interscience, New York, 1972, 607.
23. Hollander, J. M. and Shirley, D. A., *Annu. Rev. Nucl. Sci.*, 20, 435 (1970).
24. Johansson, G., Hedman, J., Berndtsson, A., Klasson, M., and Nilsson, R., *J. Electron Spectrosc. Relat. Phenom.*, 2, 295 (1973).
25. Kim, K. S., O'Leary, T. J., and Winograd, N., *Anal. Chem.* 45(13), 2214 (1973).
26. Huchital, D. A. and McKeon, R. T., *Appl. Phys. Lett.*, 20, 158 (1972).
27. Ebel, M. F. and Ebel, H., *J. Electron Spectrosc. Relat. Phenom.*, 3, 169 (1974).
28. Dickinson, T., Povey, A. F., and Sherwood, P. M. A., *J. Electron Spectrosc. Relat. Phenom.*, 2, 441 (1973).
29. Grunthaner, F. J., Ph. D. thesis California Institute of Technology, Pasadena, 1974.
30. Ogilvie, J. L. and Wolberg, A., *Appl. Spectrosc.*, 26(3), 401 (1972).
31. Hnatowich, D. J., Hudis, J., Perlman, M. L., and Ragaini, R. C., *J. Appl. Phys.*, 42(12), 4883 (1971).
32. Dianis, W. P. and Lester, J. E., *Anal. Chem.*, 45(8), 1416 July (1973).
33. Betteridge, D., Carver, J. C., and Hercules, D. M., *J. Electron Spectrosc. Relat. Phenom.*, 2, 327 (1973).
34. Ginnard, C. R. and Riggs, W. M., *Anal. Chem.*, 46(9), 1306 (1974).
35. Ginnard, C. R. and Riggs, W. M., *Anal. Chem.*, 44(7), 1310 (1972).
36. Bagus, P. S., The role of Ab initio molecular orbital calculations in the analysis and interpretations of X-ray photo-electron spectra, in *Proceeding of the International Symposium on X-Ray Spectra and Electronic Structure of Matter*, Faessler, A. and Wiech, G., Eds., Fotodruck Frank OHG, München, 1972, 256.
37. Clark, D. T., Feast, W. J., Kilcast D., and Musgrave, W. K. R., *J. Polym. Sci., Polym. Chem. Ed.*, 11(2), 389 (1973).
38. Koopmans, T. C., *Physica*, 1(2), 104 (1933).
39. Davis, D. W., Banna, M. S., and Shirley, D. A., *J. Chem. Phys.*, 60(1), 237 (1974).
40. *Handbook of Spectroscopy*, Vol. 1, Robinson, J. W., Ed., CRC Press, Cleveland, 1974, 517, 752.
41. Wagner, C. D. and Biloen, P., *Surf. Sci.*, 35, 82 (1973).
42. Wagner, C. D., *Anal. Chem.*, 47(7), 1201 (1975).
43. Kowalczyk, S. P., Ley, L., McFeely, F. R., Pollak, R. A., and Shirley, D. A., *Phys. Rev. B:*, 9(2), 381 (1974).
44. Wagner, C. D., *Anal. Chem.*, 44(6), 967 (1972).
45. Wagner, C. D., Chemical Shifts of Auger Lines, and the Auger Parameter, presented at Discussions of the Faraday Society, Vancouver, Canada, July, 1975.
46. Carlson, T. A., Carver, J. C., and Vernon, G. A., *J. Chem. Phys.*, 62(3), 932 (1975).
47. Wertheim, G. K., Cohen, R. L., Rosencwaig, A., and Guggenheim, H. J., in *Electron Spectroscopy*, Shirley, D. A., Ed., American Elsevier, New York, 1972, 813.
48. Ikemoto, I., Thomas, J. M., and Kuroda, H., *J. Chem. Soc. Faraday Discuss.*, 54, 208 (1972); Ikemoto, I., Thomas, J. M., and Kuroda, H., *Bull. Chem. Soc. Jap.*, 46, 2237 (1973); L. J. Aarons et al., *J. Chem. Soc. Faraday II*, 69(2), 270 (1973).
49. Tolman, C. A., Riggs, W. M., Linn, W. J., King, C. M., and Wendt, R. C., *Inorg. Chem.*, 12(12), 2770 (1973).
50. Matienzo, L. J., Yin, L. I., Grim, S. O., and Swartz, W. E., Jr., *Inorg. Chem.*, 12(12), 2762 (1973).
51. Frost, D. C., Ishitani, A., and McDowell, C. A., *Mol. Phys.*, 24(4), 861, 1972.
52. Kim, K. S., *J. Electron Spectrosc. Relat. Phenom.*, 3, 217 (1974).
53. Fadley, C. S. and Shirley, D. A., *Phys. Rev. A:*, 2(4), 1109 (1970).
54. Kowalczyk, S. P., Ley, L., Pollak, R. A., McFeely, F. R., and Shirley, D. A., *Phys. Rev., B:*, 7, 4009 (1973).
55. Carver, J. C., Schweitzer, G. K., and Carlson, T. A., *J. Chem. Phys.*, 57(2), 973 (1972).
56. McFeely, F. R., Kowalczyk, S. P., Ley, L., and Shirley, D. A., *Solid State Commun.*, 15, 1051 (1974).
57. Dwight, D. W. and Riggs, W. M., *J. Colloid Interface Sci.*, 47(3), 650 (1974).
58. Phillips, R. W., *J. Colloid Interface Sci.*, 47(3), 687 (1974).
59. Clark, D. T. and Tripathi, K. C., *Nat. Phys. Sci.*, 244, 77 (1973).
60. Brinen, J. S. and McClure, J. E., *Anal. Lett.*, 5(10), 737 (1973).
61. Carlson, S. A. and Hercules, D. M., *Anal. Chem.*, 45(11), 1794 (1973).
62. Kilcast, D., Feast, W. J., Musgrave, W. K. R., and Clark, D. T., *J. Polym. Sci.*, A-1, 10, 1637 (1972).
63. Swartz, W. E. Jr. and Hercules, D. M., *Anal. Chem.*, 43(13), 1774 (1971).
64. Larson, P. E., *Anal. Chem.*, 44(9), 1678 (1972).
65. Wertheim, G. K. and Rosencwaig, A., *Phys. Rev. Lett.*, 26(19), 1179 (1971).
66. Pines, D., *Elementary Excitations in Solids*, W. A. Benjamin Publishing, New York, 1963.
67. Wendt, R. C. and Riggs, W. M., Surface Analysis by X-ray Photoelectron Spectroscopy, presented at Eastern Analytical Symposium, New York, Nov. 1971.
68. Wheeler, J. A., personal communication, 1973.
69. Powell, C. J., *Surf. Sci.*, 44(1), 29 (1974).
70. Wagner, C. D., *Anal. Chem.*, 44(6), 1050 (1972).
71. Swingle, R. S., II, *Anal. Chem.*, 47(1), 21 (1975).
72. Creuzburg, M., *Z. Phys.*, 196, 433 (1966).
73. Ebel, H. and Ebel, M. F., *X-Ray Spectrom.*, 2(1), 19 (1973).

74. Carter, W. J., Schweitzer, G. K., and Carlson, T. A., *J. Electron Spectrosc. Relat. Phenom.*, 5, 827 (1974).
75. Du Pont Tech. Product Bull. #650–1007, September, 1974.
76. Scofield, J. H., Tech. Report No. 51326, University of California Radiation Lab., 1973.
77. Scofield, J. H., personal communication, 1973.
78. Wagner, C. D., personal communication, 1975.
79. Fraser, W. A., Florio, J. V., Delgass, W. N., and Robertson, W. D., *Surf. Sci.*, 36, 661 (1973).
80. Fadley, C. S., Baird, R. J., Siekhaus, W., Novakov, T., and Bergstrom, S. A. L., *J. Electron Spectrosc. relat. Phenom.*, 4, 93 (1974).
81. Yin, L. I., Ghose, S., and Adler, I., *Appl. Spectrosc.*, 26(3), 355 (1972).
82. Kim, K. S., Baitinger, W. E., Amy, J. W., and Winograd, N., *J. Electron Spectrosc. Relat. Phenom.*, 5, 351 (1974).
83. Tracy, J. C., in *Electron Emission Spectroscopy*, Dekeyser, W., Fiermans, L., Vanderkelen, G., and Vennik, J., Eds., Reidel Publishing, Boston, 1973, 295-329.
84. Jenkins, R. and de Vries, J. L., *Practical X-Ray Spectrometry*, 2nd ed., Springer-Verlag, New York, 1969.
85. Siegbahn, K., Hammond, D., Fellner-Feldegg, H., and Barnett, E. F., *Science*, 176, 245 (1972).
86. Wannberg, B., Gelius, U., and Siegbahn, K., *J. Phys. E.*, 7(3), 149 (1974).
87. Sar-el, H. Z., *Rev. Sci. Instrum.*, 38(9), 1210 (1967).
88. Lee, J. D., *Rev. Sci. Instrum.*, 44(7), 893 (1973).
89. Gellender, M. E. and Baker, A. D., *J. Electron Spectrosc. Relat. Phenom.*, in press, 1975.
90. Helmer, J. C. and Weichert, N. H., *Appl. Phys. Lett.*, 13(8), 266 (1968).
91. Carter, G. and Colligon, J. S., *Ion Bombardment of Solids*, American Elsevier, New York, 1968.
92. Kaminsky, M., *Atomic and Ionic Impact Phenomena on Metal Surfaces*, Academic Press, New York, 1965.
93. Du Pont Instruments Tech. Product Bull. #650–1010, June, 1975.
94. Fadley, C. S., Ph. D. dissertation, University of California at Berkeley, 1970.
95. Wertheim, G. K., *J. Electron Spectrosc. Relat. Phenom.*, 6, 239 (1975).
96. McLachlan, A. D., Jenkin, J. G., Liesegang, J., and Leckey, R. C. G., *J. Electron Spectrosc. Relat. Phenom.*, 3, 207 (1974).
97. Van Cittert, P. H., *Z. Phys.*, 69(5–6), 298 (1931).
98. Jansson, P. A., Hunt, R. H., and Plyler, E. K., *J. Opt. Soc. Am.*, 58(12), 1665 (1968).
99. Jansson, P. A., Hunt, R. H., and Plyler, E. K., *J. Opt. Soc. Am.*, 60(5), 596 (1970).
100. Millard, M. M., *Anal. Chem.*, 44(4), 828 (1972).
101. Swingle, R. S., II, Ginnard, C. R., and Madden, G. I., ESCA Studies of Nickel-Boron Electroless Coatings, presented at the Pittsburgh Conference on Analytical Chemistry, Cleveland, March, 1975.
102. Portnoi, K. I., Romashov, V. M., Chubarov, V. M., Levinskaya, M. Kh., Salibekov, S. E., *Poroshk. Metall.*, 50(2), 15 (1967).
103. Riggs, W. M. and Parker, J. J., in *Modern Methods of Surface Analysis*, Czanderna, A. W. and Wolsky, S. P., Eds., American Elsevier, New York, 1975.
104. Brinen, J. S., *J. Electron Spectrosc. Relat. Phenom.*, 5, 377 (1974).
105. Ginnard, C. R., Du Pont Applications Data, Bull. ES–0007, February, 1974.
106. Duch, M. W., personal communication, 1975.
107. Swingle, R. S., II, Groff, R. P., and Monroe, B. M., *Phys. Rev. Lett.*, 35(7), 452 (1975).
108. Coleman, L. B., Cohen, M. J., Sandman, D. J., Yamagishi, F. G., Garito, A. F., and Heeger, A. J., *Solid State Commun.*, 12(11), 1125 (1973).
109. Ferraris, J., Cowan, D. O., Walatka, V., Jr., and Perlstein, J. H., *J. Am. Chem. Soc.*, 95, 948 (1973).
110. Ginnard, C. R., Swingle, R. S., II, and Monroe, B. M., *J. Electron Spectrosc. Relat. Phenom.*, 6(1), 77 (1975).
111. Grobman, W. D., Pollak, R. A., Eastman, D. E., Maas, E. T., Jr., and Scott, B. A., *Phys. Rev. Lett.*, 32(10), 534 (1974).
112. Coad, J. P. and Cunningham, J. G., *J. Electron Spectrosc. Relat. Phenom.*, 3, 435 (1974).
113. Brongersma, H. H. and Mul, P. M., *Surf. Sci.*, 35, 393 (1973).
114. Benninghoven, A., *Surf. Sci.*, 35, 427 (1973).
115. Palmberg, P. W., *Anal. Chem.*, 45(6), 549A (1973).
116. Shimizu, R., Ishitani, T., Kondo, T., and Tamura, H., *Anal. Chem.*, 47(7), 1020 (1975).
117. Erickson, R. L. and Smith, D. P., *Phys. Rev. Lett.*, 34(6), 297 (1975).